UNIVERSITY OF OSLO
Institute of Theoretical Astrophysics

Hinode/EIS Spectroscopy and Modeling

Master Thesis

Marte Elisabeth Skogvoll

June 2007

Acknowledgments

First of all I want to thank my supervisor Viggo Hansteen for guiding me through this project. I am very grateful for the endless patience he has had with me and my continual questions. Thanks also to Geir Emblemsvåg for helping me with all my physics and computer problems, and for proof reading my thesis.

I also want to thank Mats Carlsson, Luc Rouppe Van Der Voort and Øystein Langangen for taking me to The Swedish Solar Telescope in May 2006 and letting me be a 'real' astronomer for a while.

Thanks to the people in and around IAESTE, Fysikkforeningen, and Fysisk Fagutvalg for making these five years at Blindern a memorable part of my life. Especially I want to thank Josefine for being my friend and fellow student throughout these years. It would not have been the same without you.

I want to thank Sofie, Glenn, Hanne Sigrun, Thale, Kosovare, Iselin, Stefano, Vegard, Nicolaas, and the rest of the people at Stjernekjelleren for the interesting discussions around the lunch table. Thanks also to The Institute of Theoretical Astrophysics for providing such great facilities, which has contributed to the good professional and social environment in our study hall.

Finally, I want to thank the rest of my friends and my family for caring and for making me think about other things than physics. Especially, I want to thank Ivar for proof reading my thesis and for his indulgence the last couple of months.

Marte Elisabeth Skogvoll
June 2007

Contents

Chapter 1

Introduction

The Sun is our nearest star. By providing heat and light it sustains life on Earth and influences our climate. It is therefore interesting to understand more about its physical processes. In addition, the Sun is important in the study of other stars. The Sun is an average star, and its unique location makes it possible to study in much greater details than the stars further away. Better knowledge of the Sun improves our understanding of other stars and astrophysical objects.

To increase our understanding of the Sun and its processes, further observations are needed. In this matter, the Hinode satellite, which is the subject of the thesis, will make valuable contributions with its studies of the solar atmosphere.

We begin the chapter by describing the structure of the Sun and one of the important problems solar physicists are faced with today. Then we give a short description of the Hinode satellite and its instruments. We end the chapter by describing the aim of the thesis, the methods we are using, and the thesis outline.

1.1 The Sun

1.1.1 Solar Structure

The Sun is commonly divided into two parts; the solar interior and the solar atmosphere. An illustration of the solar structure is given in Figure 1.1. The interior consists of a core which extends some 20 percent of the solar radius, where the hydrogen fusion is taking place. This is the process by which the Sun ultimately generates its energy of 3.9×10^{26} W, and with a radius of 7×10^8 m this is equivalent to a flux of 6.3×10^7 W/m^2 at the solar surface. This energy has to be transported out of the Sun, and throughout most of the interior this is done by radiation. In the upper 20 percent of the Sun's radius the energy is transported by convection. The solar magnetic field,

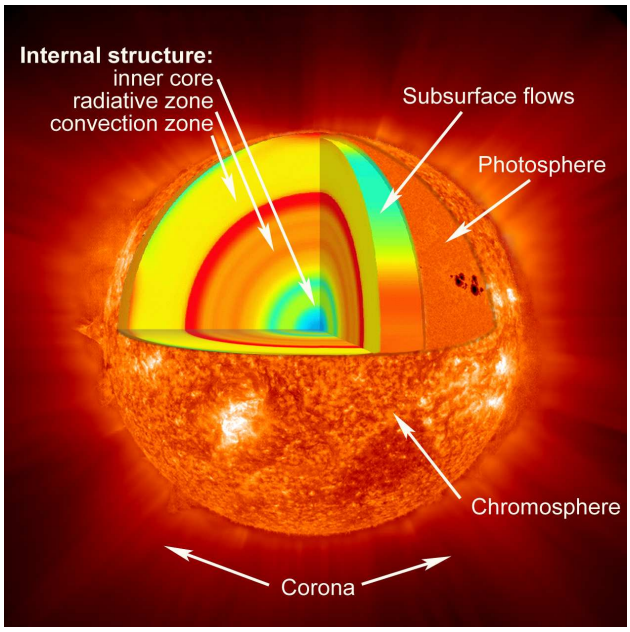

Figure 1.1: Illustration of the solar structure. (NASA)

which is the source of much of the solar atmosphere's activity, is continually generated by the action of convection and by the Sun's differential rotation.

The solar atmosphere is divided into four regions, namely the photosphere, the chromosphere, the transition region, and the corona. The photosphere is the part of the Sun which is seen in visible light. Because of the rapidly changing odds of a photon escaping the Sun through this region, which has a depth of only 500 km, the Sun appears with a clear edge, the solar limb. The temperature in the photosphere is about 6000 K, but decreases with height. The granulation pattern we see in the photosphere is the last remnant of the convection zone which extends to the bottom of the photosphere.

After temperature minimum, some few hundred kilometers above the photosphere, the chromosphere's temperature increases slightly, then remains roughly isothermal for some 2000 km. The density decreases exponentially with a scale height of some 200 km in this area. In the upper parts of the chromosphere the magnetic field changes from being controlled by the denser photospheric gas to controlling the plasma structure.

The outer layer of the solar atmosphere is the corona, which extends out to a distance of several million km. The temperature here is some MK, and with a density of some 10^{-11} kg/m^3 it is only about 10^{-12} as dense as the photosphere. With this density and temperature the corona can only be seen in visible wavelengths when the light from the photosphere has been blocked out by an eclipse or through the use of a coronagraph. Instead it is common

to observe this region of the solar atmosphere in X-ray wavelengths. Here the magnetic field expands in the increasingly tenuous plasma and fills all space around the Sun some few thousand kilometers above the photosphere.

Between the chromosphere and the corona lies the transition region. In this region the temperature rises rapidly, from some 10^4 K to 10^6 K in only a few Mm. The transition region emits most of its radiation in extreme ultraviolet (EUV) spectral emission lines, mainly originating from strongly ionized metals.

The solar wind is an extension of the Sun's atmosphere, with the high speed electrons and ions from the corona escaping into interplanetary space.

1.1.2 The Heating Problem

As described above, the Sun's energy is formed in the core and transported from there and out to the Sun's surface. Therefore one should expect, according to the second law of thermodynamics, that the temperature would decrease with distance from the Sun's center. This is indeed the case for the solar interior to the photosphere. From this point and upwards the opposite is the case, the upper parts of the solar atmosphere have a much greater temperature than the photosphere. This was shown by Edlén (1943) by identifying forbidden lines of highly ionized atoms.

Because the corona is such a tenuous plasma the energy flux needed to heat it up to a few MK is actually quite small, only some 100 W/m^2. This is only 10^{-6} of the radiative energy flux emerging from the Sun, which therefore should be more than enough to heat the corona. The lack of energy emerging from the solar interior is thus not the problem, but rather to find a mechanism that is able to transmit the energy through the photosphere, chromosphere, and transition region, and then to deposit it into the corona. This is commonly called 'the heating problem' and has been one of the major questions for solar physicists the last 60 years.

Throughout the years several theories have been suggested; e.g. Biermann (1946, 1948) and Schwarzschild (1948) suggested that sound waves produced in the solar convection zone heated the chromosphere and corona, while Alfvén (1947) and Osterbrock (1961) suggested that magnetic (MHD) wave modes could carry the energy flux.

The leading idea today is that the energy transfer must be related to the magnetic field, and possibly to the reconnection of magnetic field lines. Photospheric motions concentrate the magnetic field into small elements or patches that are spread over the entire solar surface. In some regions, such as in sun spots or plage regions, the field becomes strong enough to dominate the dynamics of the photosphere. Magnetic field lines are forced towards the inter-granular lanes because of the convection, which randomly shuffling them about, causing stress to build up. As the field lines become too twisted they might snap and rearrange, causing dissipation of magnetic en-

ergy in the corona, and thus heating it (Parker, 1983). This is commonly called nano-flare heating by magnetic reconnection. Observational evidence of this type of event has been found by e.g. Yokoyama et al. (2001). In addition, ab initio simulations by Gudiksen and Nordlund (2005) based on this idea, starting from a prescribed photospheric velocity field and observed photospheric magnetic field, generate coronal structures very similar to those observed. Even so, the answer to the heating problem is still not fully understood, and further observations are needed to better understand the role of the magnetic field in the coronal heating. To determine how the energy is transferred from below the photosphere and up into the outer atmosphere, we need to simultaneously measure the changes in the magnetic field and the emission lines' intensities from the transition region and corona.

1.1.3 Observations of the Solar Atmosphere

Since the recognition of the high temperatures in the upper solar atmosphere there has been a need for better observations of this region. As described above, the transition region and the corona emit most of their radiation in EUV and X-ray wavelengths, respectively. The Earths atmosphere is opaque to these wavelengths, so to be able to observe these regions in the wavelengths they are emitting strongest, the detector must be sent up above our atmosphere.

There have been several successful rocket and satellite experiments so far, e.g. *Orbiting Solar Observatory*, *Skylab*, *Spacelab 2*, and in later times the *Solar and Heliospheric Observatory* (SOHO) and *Transition Region and Coronal Explorer* (TRACE).

1.2 Hinode

The Japanese *Hinode* (Solar-B) (Ichimoto and Solar-B Team, 2005), the successor to YOHKOH (Solar-A) mission, was launched 22 September 2006 21:36 UT. It studies the Sun in visible, EUV, and X-ray wavelengths, in addition to being able to produce vector magnetogram maps. The satellite is moving in a 680 km circular Sun-synchronous orbit over the Earth's day/night terminator, which allows near-continuous observation of the Sun. Each orbit takes 96 minutes, which yields 15 orbits a day. Data is brought down at a number of ground stations, including at the Uchinoura Space Centre in Japan and at KSAT's Svalbard Station. This allows at least 17 daily ground station contacts, and thus an average of 6 Gbytes data telemetry a day. Hinode carries three instruments; a Solar Optical Telescope (SOT), an X-ray Telescope (XRT) and an EUV Imaging Spectrometer (EIS). A short description about each of them are given below.

SOT

SOT (Ichimoto et al., 2004) consists of two major components; namely the Optical Telescope Assembly (OTA) and the Focal Plane Package (FPP). OTA is with its 50 cm, the largest optical solar telescope that has ever been sent out into space. It has a wavelength coverage of 3870–6680 Å (visible light), and will thus observe the photosphere and chromosphere. It has a resolution of 0.25 arc seconds, which means that details down to 175 km can be resolved on the Sun. The light captured by SOT is analyzed in the FPP consisting of three instruments; a Narrowband Filter Imager (NFI), a Broadband Filter Imager (BFI) and a Spectropolarimeter (SP). NFI can compute the four Stokes parameters and Dopplergrams (line-of-sight velocity) of the photosphere and chromosphere. BFI produces high spatial and temporal resolution images and measures horizontal flow and the temperature in the photosphere. With the polarized spectra from SP one can produce photospheric 3D vector magnetograms.

XRT

XRT (Kano et al., 2004) is a high resolution grazing incidence telescope, and its goal is to observe the high temperature plasma of the corona. By producing images with different X-ray filters, XRT can observe in a wider temperature band (1–30 MK) than previous X-ray telescopes. This allows for detections of dissipation of magnetic energy in forms of flares and coronal mass ejections. XRT can either observe the full solar disk or a smaller area with higher resolution. XRT is expected to have an angular resolution of 2 arc seconds, or about 1400 km on the Sun. Built-in visible light optics allow for sub-pixel accuracy image alignment with SOT.

EIS

EIS (Culhane et al., 2007) is an EUV spectrometer which can observe various lines in two wavelength intervals, 170–210 Å and 250–290 Å, covering a wide range of plasma temperatures (0.1–20 MK). With the spectra from EIS it is possible to determine the intensity, the Doppler velocity, the line width, and the temperature and density of the plasma where the line is formed.

Due to the use of multi-layer coated optics and back-illuminated CCDs, EIS has approximately a factor 10 enhancement in effective area compared to CDS (on board SOHO). In addition, the spectral resolution (3 km/s for Doppler velocities) is also improved by an order of magnitude, and the spatial resolution (2 arc seconds) is improved by a factor two or three compared to CDS.

1.2.1 Scientific Aims

The scientific aims of the Hinode mission are focused on three main goals:

- To determine the mechanisms responsible for heating the corona in active regions and the quiet Sun.
- To establish the mechanisms responsible for transient phenomena, such as flares and coronal mass ejections.
- To investigate the processes responsible for energy transfer from the photosphere to the corona.

These goals will be approached by using the combination of the three different instruments on board the satellite. By observing the photosphere and the underlying magnetic field at the same time as the chromosphere and corona, one gets a better possibility of understanding the connection between the different parts of the Sun. In particular, it is interesting to observe the dynamic and thermal response of the corona to the changing magnetic and velocity fields of the photosphere and convection zone, to see if we can get closer to the answer to the heating problem.

1.3 The Thesis

The aim of the thesis is to better understand how we can relate the EIS observations to physical phenomena in the solar atmosphere. Specifically, we want to study how the diagnostic variables react to changes in the morphology in the solar atmosphere. That is, we will study how the line intensity and the Doppler velocity for the spectral lines observable with EIS react to the changes in temperature, density, and velocity. Especially, we want to study the iron lines formed in the corona around 1 MK, and examine what they can tell us about the condition in the upper solar atmosphere.

Since we can not 'check' what is really happening when there is an event on the Sun for then to see how the EIS lines respond to these, we approach this problem by numerical simulations. We make a model of the solar atmosphere, introduce perturbations to this system, and examine how the properties of the gas change according to these events. Then we study how the EIS emission lines change as a result of this perturbation. Thereafter, we discuss which of these changes EIS is actually able to detect, and whether observing with EIS can explain the physical phenomena causing these changes.

EIS is only able to detect the emission line intensity, Doppler velocity, and line width. In addition, one can also compute the temperature and density in the region where the line is formed. These temperature and density diagnostics are only reliable as long as the line is formed in ionization equilibrium. Therefore, we also examine whether any of our spectral lines are driven out of equilibrium during our simulations.

By following this procedure we can come to a better understanding of which phenomena EIS is able to detect, which limitations the data have, and which cautions must be taken when drawing conclusions from the EIS observations to the physical explanations about what is actually happening. Thus we find out how to better use the EIS data.

1.3.1 Methods

To solve this problem we use a combination of the simulation code TTRANZ (Hansteen, 1991) and the IDL package CHIANTI (Landi et al., 2006; Dere et al., 1997). TTRANZ solves the hydrodynamic plasma equations in one dimension along with the rate equations which determine the radiative losses from the transition region and corona. CHIANTI is an atomic database and contains routines for exploitation of this data.

A schematically overview of the work is given by:

1. Identifying the most important EIS spectral emission lines by using the CHIANTI atomic database.

2. Constructing usable TTRANZ atomic data files, using the CHIANTI atomic database, the HAO-DIAPER package (Judge and Meisner, 1994), and the NIST line database (Ralchenko et al., 2005) as references.

3. Constructing a coronal loop model and examining how this reacts to perturbations, such as changes in the heating rate and forced waves on the system.

4. Examining how the chosen EIS spectral lines' intensities and velocities react to the loop changes.

5. Examining whether any of the chosen EIS spectral lines are driven out of ionization equilibrium in the scenarios described above.

1.3.2 Thesis Outline

The remainder of this thesis is divided into five chapters. We start by going through the basic physics behind emission line formation and the hydrodynamic plasma equations in Chapter 2. Further, in Chapter 3 we describe our simulation code, explain the numerical schemes in use, and how input are given to the program. In Chapter 4 we examine the performance of the EIS spectrograph and decide which emission lines in the EIS passband that are usable for our purpose. In this chapter we also design the atomic models needed. In Chapter 5 we run our simulation code with the input found in the previous chapters. We perturb the system by changing the heat input and

forcing waves on the system, and analyze the changes in the loop morphology. Thereafter, we examine the diagnostic variables for the chosen lines to see if they can explain the loop changes. Finally, in Chapter 6 we summarize what we have done and which results we have come to and give suggestions for further work and improvements.

Chapter 2

Basic Line and Plasma Physics

In this chapter we first give an introduction to what an emission line is. Thereafter, we go through the different processes that contribute to the emission line formation and the processes that determine the ionization state of an element. Then we explain how we can compute the emission lines' intensity and Doppler velocity. Finally, we give a short introduction to the hydrodynamic plasma equations, which describe the behavior of the plasma in the solar atmosphere.

2.1 Introduction

The solar atmosphere consists of a warm and low density gas. Below lies the cooler and denser photosphere, which radiates as a black body with its emission peak in the visible wavelength interval. Therefore, the atmosphere is most easily observed in the short wavelength part of the spectrum, where its emission lines out-shine the continuum.

Emission lines are caused by photons emerging from the solar atmosphere when an ion de-excites from an excited upper energy level 'u' to a lower energy level 'l'. The energy taken away by the photon is given by the energy difference of the two levels,

$$\Delta E = E_u - E_l = h\nu \,, \tag{2.1}$$

where h is the Planck constant, ν is the frequency, and E_u and E_l are the energies of the upper and lower levels, respectively.

The gas is considered *optically thin* when all the emitted photons leave the atmosphere without being scattered, and *effectively thin* if all created photons eventually escape after a number of scatterings before being thermalized. The intensity I_ν of an optically thin spectral emission line with frequency ν is related to the number density of ions in the correct upper energy

level (n_u), and the rate at which these de-excite by emitting a photon (A_{ul}).

$$I_\nu = \frac{h\nu}{4\pi} \int_0^s n_u A_{ul}\, \phi_\nu \, ds \,, \tag{2.2}$$

where we have divided by the sphere solid angle unit since the photon can be sent out in any direction, and integrated along the line of sight s. ϕ_ν is the line's emission profile which we will come back to in Section 2.4.1.

To compute the intensity we thus have to find expressions for our two unknowns n_u and A_{ul}. These are both related to the ion's excitation and de-excitation processes which we discuss in Section 2.2.

2.2 Electron Excitation and De-excitation

Electron excitation is the process in which a bound electron transfers from a low lying energy level 'l' (ground or excited) to a higher energy level 'u' by stealing energy from a photon or a free electron. The inverse process is called electron de-excitation, and take place when a bound electron transfers from an excited energy level to a lower lying level (ground or excited) and the extra energy is taken away either by a photon or a free electron.

Bound-bound transitions between two levels can occur in different ways, and we will give a short introduction to each of them:

- radiative excitation and de-excitation (photoabsorption, spontaneous radiative de-excitation, and stimulated emission) (Section 2.2.1)
- collisional excitation and de-excitation (Section 2.2.2)

2.2.1 Radiative Excitation and De-excitation

Absorption is the process in which an ion absorbs a free photon and becomes excited up into a higher energy level. The rate coefficient for this process is denoted B_{lu}. The inverse process, called spontaneous radiative de-excitation, is the process where an excited atom decays into a lower level, and thus emits a photon which carries away the energy difference between the two levels. Its rate coefficient is denoted A_{ul}.

$$X_l + h\nu \Leftrightarrow X_u \,, \tag{2.3}$$

where X_l and X_u denote the lower and upper energy levels, respectively.

The principle of detailed balance states that in thermal equilibrium (TE) the number of transitions due to one process is exactly balanced by its inverse process. To meet this requirement of TE, we need a third process, namely stimulated emission, with rate coefficient B_{ul}. In this process a photon hits an excited atom, which then de-excites and sends out another photon,

$$X_u + h\nu \Rightarrow X_l + h\nu + h\nu \,. \tag{2.4}$$

These three rate coefficients are all called Einstein coefficients, and are related by

$$\frac{B_{ul}}{B_{lu}} = \frac{\omega_l}{\omega_u}\,, \tag{2.5}$$

where ω_u and ω_l are the multiplicities (statistical weights) for the upper and lower levels, respectively, and

$$\frac{A_{ul}}{B_{ul}} = \frac{2h\nu^3}{c^2}\,, \tag{2.6}$$

where c is the speed of light in vacuum. These two relations hold universally since they do not depend on any property of the medium.

The spontaneous de-excitation rate is in the literature often given by the oscillator strength (f_{ul}), which is related to the Einstein A coefficient by (Rutten, R. J., 2003),

$$A_{ul} = 6.671 \times 10^{15} \frac{\omega_l}{\omega_u} \frac{f_{ul}}{\lambda^2}\,, \tag{2.7}$$

with λ in Å.

2.2.2 Collisional Excitation and De-excitation

A free electron that moves close to an ion can transfer some of its energy to one of the bound electrons. The free electron loses the same amount of energy as it takes to excite the bound electron from a lower level 'l' into an upper level 'u'. The transition rate for collisional excitation is denoted C_{lu}. In the inverse process an electron hits an excited atom, the bound electron de-excites to a lower level and the free electron takes away the extra energy. The rate coefficient for this process is denoted C_{ul}. These processes are also called electron impact excitation and electron impact de-excitation.

$$X_l + e \Leftrightarrow X_u + e \tag{2.8}$$

The collisional excitation rate coefficient is related to the collision cross section (σ) of the collision between the ion and electrons of velocity u.

$$C_{lu} = \int_{u_0}^{\infty} \sigma_{lu}(u) f(u) u \, du\,, \tag{2.9}$$

where the threshold energy is given by $\frac{1}{2} m_e u_0^2$ (m_e is the electron mass) and f is the velocity distribution function of the electrons. The collision cross section can be found either by theoretical calculations or in laboratory experiments.

Assuming that the electron distribution function is Maxwellian, we can write the collision rate as a function of the temperature alone (Mason and Fossi, 1994),

$$C_{lu}(T_e) = \frac{C_0}{\omega_l} T_e^{-1/2} e^{-\Delta E / k_B T_e} \Upsilon_{lu}(T_e)\,, \tag{2.10}$$

where ω_l is the multiplicity of the lower level, $C_0 = 8.63 \times 10^{-6}$ is a constant, k_B is the Boltzmann constant, and T_e is the electron temperature. Υ_{lu} is the thermally averaged collision strength, which is a slowly varying function with temperature.

The rate coefficients for the collisional excitation and de-excitation processes are related through the detailed balance principle,

$$\frac{C_{lu}}{C_{ul}} = \frac{\omega_u}{\omega_l} e^{-\Delta E / k_B T_e} \,. \tag{2.11}$$

This relation also holds outside TE, as long as the electron velocity distribution function is Maxwellian.

2.2.3 Coronal Equilibrium

We have now given an overview of the different excitation and de-excitation processes that can occur. We are interested in the region of the solar atmosphere where the extreme ultraviolet (EUV) radiation is emitted. In this region the electron density is low ($n_e < 10^{18}$ m^{-3}) and the temperature is high ($T_e > 10^4$ K). This leads to the so-called *Coronal Equilibrium* (CE) condition, which allows us to do some simplifications.

Excitation – De-excitation Rate Equation

With CE conditions it is usually safe to assume that the population of the upper level mainly is produced by collisional excitation from the ground level, and that the spontaneous radiative decay overwhelms the other depopulation processes. The number of excitations and de-excitations must balance each other, so we get the simple relation

$$n_u A_{ul} = n_l n_e C_{lu} \,. \tag{2.12}$$

This approximation is not correct if there is no allowed transition (according to the electric dipole approximation) down from the excited state 'u'. If this is the case, the spontaneous radiative de-excitation rate is quite small and the collision de-excitation rate becomes comparable to it. This kind of upper level is called a *meta-stable* level, and extra attention must be given to these levels when designing our atomic model.

Assuming Equation 2.12 to be valid, another expression for the unknown parameters in Equation 2.2 ($n_u A_{ul}$) are found. In the previous section we also found an expression for the collision excitation rate (Equation 2.10), so our challenge is now to find the number density of ions in the lower energy level, n_l.

Number Density

Within CE we can assume that the de-excitation rates are much higher than the excitation rates. As noted above, this is not the case for meta-stable levels, which can cause a notable amount of the ions to not be in the ground state.

Without meta-stable levels the number of ions in the low-energy level can be considered the same as the total number of ions in the ionization state.

$$n_l(X^m) \approx n(X^m)\,, \tag{2.13}$$

where X^m represent the ionization state m, and the subscript 'l' denotes the excitations level, which is normally the ground level. We can express the number of ions in the lower level as

$$n_l(X^m) = \left(\frac{n(X^m)}{n(X)}\right)\left(\frac{n(X)}{n_H}\right) n_H\,, \tag{2.14}$$

where the first ratio is the fraction of the element in the correct ionization state and the second is the element abundance relative to hydrogen,

$$\frac{n(X)}{n_H} = A_b\,. \tag{2.15}$$

This abundance can, as a first approximation, be considered constant through the solar atmosphere. The ionization fraction on the other hand, varies a lot according to the temperature and density. We examine the ionization and recombination processes in Section 2.3.

2.3 Ionization and Recombination

It is the bound-free and free-bound processes that make an atom transfer from one ionization stage to the next as the surrounding environment changes. The ionization state is found by solving the rate equation,

$$\frac{\partial n(X^m)}{\partial t} + \frac{\partial}{\partial z}(n(X^m)u) = \text{ Sources } - \text{ Sinks}\,. \tag{2.16}$$

We will take a look at the ionization and recombination processes, which can be both sources and sinks:

- collisional ionization and 3-body recombination (Section 2.3.1)
- photoionization and radiative recombination (Section 2.3.2)
- autoionization and dielectronic recombination (Section 2.3.3)

2.3.1 Collisional Ionization and 3-Body Recombination

In collisional ionization, also called electron impact ionization, a free electron hits an atom and knocks free a bound electron. In the recombination process two free electrons enter at the same time into the volume of the ion, one of them is captured in an excited energy level while the other carries away the extra energy.

$$X_i^m + e \Leftrightarrow X_j^{m+1} + e + e \tag{2.17}$$

where m is the ionization state and i, j are the excitation levels.

As for the collisional excitation, the collisional ionization rate I_{col} is related to the collisional ionization cross section (σ). The total number of ionizations because of this process is given by

$$I_{(col)} n_e n_i(X^m) = n_e n_i(X^m) \int_{u_0}^{\infty} \sigma(u) f(u) u \, du \,, \tag{2.18}$$

where the threshold energy is given by $\frac{1}{2} m_e u_0^2$ and f is the electron velocity distribution function.

The 3-body recombination rate is denoted $R_{(3)}$. This rate is because of the detailed balance principle related to the collisional ionization rate by the Saha equation (Mihalas, 1978);

$$\left(\frac{n_i(X^m)}{n_j(X^{m+1})} \right)^* = C_1 n_e \frac{\omega^m}{\omega^{m+1}} T^{-1.5} e^{\frac{E(X^{m+1}) - E(X^m)}{k_B T_e}} \,, \tag{2.19}$$

where $C_1 = 2.07 \times 10^{-16}$ (in cgs units) and the superscript '$*$' denotes thermal equilibrium. The total number of recombinations due to the 3-body process is given by

$$R_{(3)} n_e n_j(X^{m+1}) = n_e n_j(X^{m+1}) I_{(col)} \left(\frac{n_i(X^m)}{n_j(X^{m+1})} \right)^* . \tag{2.20}$$

This holds also outside of TE as long as the velocity is Maxwellian.

Since the 3-body recombination requires the presence of two electrons at the same time, this rate is quite small for low density plasma, where the collisional ionization is the dominant ionization process.

2.3.2 Photoionization and Radiative Recombination

In photoionization a photon is absorbed by a bound electron which then breaks free from the atom. In the inverse process, radiative recombination, a free electron is captured by a 'bare' ion while a photon takes away the extra energy.

$$X_j^{m+1} + e \Leftrightarrow X_i^m + h\nu \tag{2.21}$$

The total number of ionizations because of photoionizations is given by

$$I_{(ph)} n_i(X^m) = n_i(X^m) 4\pi \int_{\nu_0}^{\infty} \frac{\alpha(\nu)}{h\nu} J_\nu \, d\nu \,, \tag{2.22}$$

where α is the photoionization cross section and J_ν is the mean intensity. Note that $I_{(ph)}$ is a function of the radiation temperature and that the total number of transitions of this kind do not depend on the electron density.

In TE the number of spontaneous recombinations must equal the number of photoionizations

$$R_{(r)} \left(n_j(X^{m+1}) \right)^* = I_{(ph)} \left(n_i(X^m) \right)^* \,. \tag{2.23}$$

The total number of radiative recombinations is therefore given by

$$\begin{aligned} R_{(r)} n_e n_j(X^{m+1}) = & n_e n_j(X^{m+1}) \left(\frac{n_i(X^m)}{n_j(X^{m+1})} \right)^* \times \\ & 4\pi \int_{\nu_0}^{\infty} \frac{\alpha(\nu)}{h\nu} B_\nu \; d\nu \,, \end{aligned} \tag{2.24}$$

where the mean intensity is given by the Planck function ($J_\nu = B_\nu$) in TE. This rate also holds when TE is not valid as long as the velocity distribution is Maxwellian.

The photoionization is negligible in optically thin plasma, because there are very few photons with enough energy to ionize the atom, while the radiative recombination, on the other hand, is the main recombination process.

2.3.3 Autoionization and Dielectronic Recombination

We can have a spontaneous ionization in a doubly excited atom if the energy of the lowest excited electron is larger than the binding energy of the other excited electron. This is called autoionization. The inverse process is of two steps. First, a free electron is captured into an excited state of the ion and another bound electron takes up the rest energy, and becomes excited too. This is the opposite of autoionization. To have dielectronic recombination we also need the second step; at least one of the two excited electrons goes through a radiative decay and sends out a photon.

$$\begin{aligned} X_g^{m+1} + e \Leftrightarrow & X_{ij}^m \\ & X_{ij}^m \rightarrow X_{gj}^m + h\nu \end{aligned} \tag{2.25}$$

Here g refers to the ground level and i, j to excited levels.

Recall from the discussion of coronal equilibrium that most of the atoms are in their ground states, so the autoionization process can not happen very often. The dielectronic recombination on the other hand, happens quite frequently in hot, low density plasma.

The dielectronic rate coefficient $R_{(d)}$ is a function of the electron temperature, and the total numbers of recombinations of this kind is given by

$$R_{(d)} n_e n_g(X^m) \,. \tag{2.26}$$

2.3.4 The Rate Equation

In the beginning of this section we stated the general rate equation (Equation 2.16), and we have now outlined its sources and sinks to see which of them that play an important role in our model. We found that in the transition region ionization is dominated by electron impact, and recombinations are dominated by radiative and dielectronic processes. We can thus simplify the rate equation by choosing $R = R_{(r)} + R_{(d)}$ and $I = I_{(col)}$. Further, if the left hand side of the rate equation is negligible, it is even more straightforward. It is negligible when the perturbation time scales are long compared to the rate characteristic times, which are in the order of tens of seconds. We can then set the left hand side of Equation 2.16 to zero and the sources and sinks have to balance each other,

$$n_e \left[n(X^{m-1}) I^{m-1} + n(X^{m+1}) R^{m+1} \right] = n_e \left[n(X^m)(I^m + R^m) \right] \,. \tag{2.27}$$

If we want to study effects that have shorter time scales than the rate characteristic time, we need to include the left hand side of the rate equation too.

Example: The Ionization Balance for Hydrogen

To clarify the concept of the rate equation we will solve it for the simplest case, that is, hydrogen with only two allowed states, neutral hydrogen with number density n_{HI} and ionized hydrogen with number density n_{HII}. We will study how the ionization fraction reacts to changes in the temperature and electron density, and relate this to the changes in the ionization and recombination rates. We also check if it is reasonable to ignore 3-body recombination, and if TE is a good approximation in the transition region.

The hydrogen atom does not have two electrons, so we can not have dielectronic recombination or autoionization. The rate equation for this system is thus given by

$$n_{HII} n_e \left[R_{(r)} + R_{(3)} \right] = n_{HI} \left[I_{(col)} n_e + I_{(ph)} \right] \,, \tag{2.28}$$

which can be rewritten

$$\frac{n_{HI}}{n_{HII}} = \frac{R_{(r)} + R_{(3)}}{I_{(col)} + \frac{I_{(ph)}}{n_e}} \,. \tag{2.29}$$

This is one equation with two unknowns, so we need one more equation to solve our problem. We can use the fact that the total number of hydrogen atoms must be constant,

$$n_{HI} + n_{HII} = n_H \,. \tag{2.30}$$

The fraction of ionized hydrogen to the total number of hydrogen atoms is thus given by

$$\frac{n_{HII}}{n_H} = \left(1 + \frac{n_{HI}}{n_{HII}}\right)^{-1} = \left(1 + \frac{R_{(r)} + R_{(3)}}{I_{(col)} + \frac{I_{(ph)}}{n_e}}\right)^{-1} \,. \tag{2.31}$$

To be able to solve this equation we need expressions for the different rates that are involved. The following expressions are taken from a hydrogen atomic model made by P. Judge for V. Hansteen in 1995. It includes atomic data from (Janev et al., 1987) as given by the HAO-DIAPER package (Judge and Meisner, 1994).

The Collisional Ionization Rate

$$I_{(col)}(T_e) = T_e^{1/2} e^{-h\nu/k_B T_e} \Upsilon(T_e) \tag{2.32}$$

with Υ being a slowly-varying function of T_e, with values around 4.2×10^{-11}.

The Photoionization Rate

$$I_{(ph)}(T_{rad}) = \frac{8\pi\alpha^{(ph)} g^{(ph)} \nu^3}{c^2} E_1 \left(\frac{h\nu}{k_B T_{rad}}\right) \tag{2.33}$$

where $\alpha^{(ph)} = 7.9 \times 10^{-18}$, $g^{(ph)} = 0.8$ is the gaunt factor, and E_1 is the exponential integral.

The Radiative Recombination Rate

$$R_{(r)}(T_e) = \alpha \left(\frac{T_e}{1 \times 10^4}\right)^{-\epsilon} \tag{2.34}$$

where $\alpha = 4.25 \times 10^{-13}$ and $\epsilon = 0.69$.

The 3-Body Recombination Rate

$$R_{(3)}(T_e, n_e) = I_{col} \times 2.07 \times 10^{-16} n_e \frac{\omega_{HI}}{\omega_{HII}} T_e^{-1.5} e^{h\nu/k_B T_e} \tag{2.35}$$

where the multiplicities are $\omega_{HI} = 2$ and $\omega_{HII} = 1$.

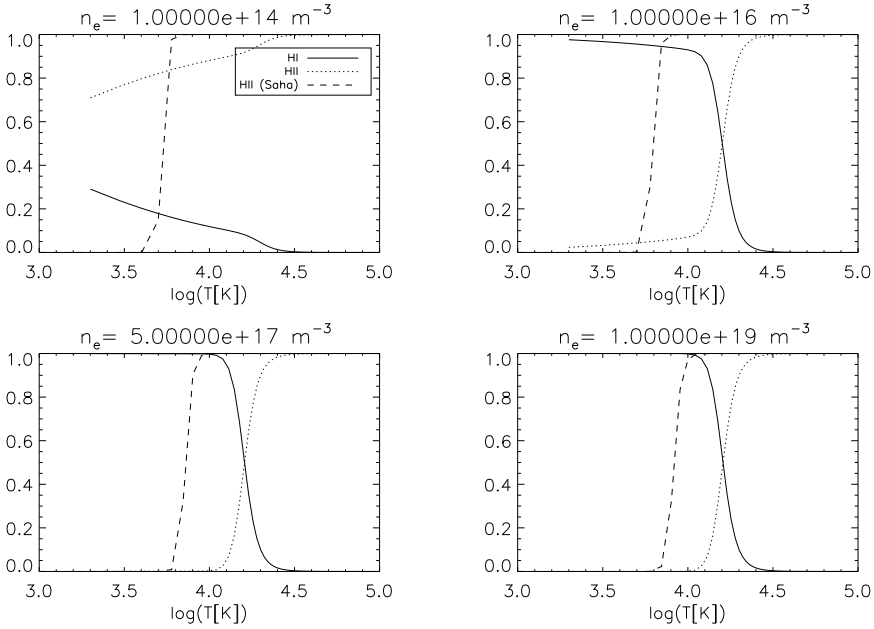

Figure 2.1: Ionization fraction for hydrogen for different electron densities; $n_e = 10^{14}$ m^{-3} (upper left), $n_e = 10^{16}$ m^{-3} (upper right), $n_e = 10^{17}$ m^{-3} (lower left), and $n_e = 10^{19}$ m^{-3} (lower right). The solid line is the fraction of neutral hydrogen, while the dotted line is the fraction of ionized hydrogen. The dashed line is the fraction of ionized hydrogen calculated from the Saha equation.

The fractions of ionized and neutral hydrogen to the total hydrogen population are plotted in Figure 2.1 as a function of temperature and for different electron densities. In the same figure we have also over-plotted the fraction of ionized hydrogen as computed from the Saha equation (Equation 2.19).

In the upper left panel, the ionization fraction is much larger for low temperatures compared to the other panels. The photoionization is neither dependent of the electron density nor the electron temperature. We would therefore expect this rate to become the dominating part of Equation 2.31 when the electron density and temperature is small. This is what we see in the upper left panel.

When the electron density is high we would expect that the 3-body recombination would dominate the radiative recombination, since the former varies as $\sim n_e^2$, while the latter varies as $\sim n_e$. This effect can not be seen in any of our plot. Probably the electron densities must be even higher than 10^{19} m^{-3} for the 3-body recombination to dominate. In CE the electron densities are less than 10^{18} m^{-3}. Therefore, it should be safe to ignore the 3-body recombination.

The Saha equation is only valid in TE, so plotting the solution to this equation shows us how far the corona approximation is from TE. We can

see that our results are getting closer to the Saha solution as the density is increasing, but clearly TE is not a good approximation for the densities we are interested in.

2.4 Emission Lines

So far we have discussed details about the atomic processes which contribute to emission line formation. It is now time to look at the observed emission line. First we explain how to compute the line intensity, Doppler velocity, and line width. Then we take a new look at how to compute the emission line intensity, and define the contribution function and branching fraction. At the end we collect the threads to get a better understanding of which plasma parameters that are important in the study of emission lines.

2.4.1 Line Profile

Emission lines are not, despite their names, infinitely thin lines but are in reality smeared out according to a line profile. The emission profile due to thermal Doppler broadening is given by

$$\phi_\nu = \frac{1}{\sqrt{\pi} w_D} \exp\left[-\left(\frac{\Delta\nu - \frac{u}{c}\nu\cos\theta}{w_D} \right)^2 \right], \tag{2.36}$$

where $\Delta\nu = \nu - \nu_0$ is the distance from the laboratory frequency, θ is the aspect angle, u is the gas velocity, and the Doppler width is given by

$$w_D = \frac{\nu_0}{c}\sqrt{\frac{2k_B T_e}{m_A}}, \tag{2.37}$$

where m_A is the mass of the radiating ion.

2.4.2 Line Momentum Analysis

The line's intensity, velocity and width are not the same throughout the solar atmosphere. We therefore have to perform a column-integration to find the values that we would observe with a spectrograph. A powerful way of doing this is momentum analysis.

Line Intensity

The total line intensity at a wavelength can be found by integrating the intensities at each depth point along the loop (z),

$$I_\nu = \int_0^z I_\nu(z)\, dz\,. \tag{2.38}$$

Doppler Velocity

Because of relative velocities between the gas and the observer the lines are shifted according to the Doppler effect,

$$\nu = \nu_0 \left(1 + \frac{u}{c}\right) , \tag{2.39}$$

where u is the velocity difference between the gas and the observer. We are here assuming motion along the line of sight only, and that the velocity is small compared to the speed of light.

The first moment,

$$M_1 = \Delta\nu = \frac{\int I_\nu(\nu - \nu_0)d\nu}{\int I_\nu d\nu} , \tag{2.40}$$

defines the mean line shift. This can be transformed to the mean velocity $\langle u \rangle$ by

$$\langle u \rangle = \frac{\Delta\nu}{\nu_0} c . \tag{2.41}$$

Line Width

As mentioned above, thermal Doppler broadening is one of the processes that increases the line width. When calculating the line width it is common to use the standard deviation,

$$\langle w_\nu \rangle = \sigma = \sqrt{M_2 - M_1^2} , \tag{2.42}$$

where the subscript 'ν' means that the width is measured in frequency, and the second moment is given by

$$M_2 = \frac{\int I_\nu(\nu - \nu_0)^2 d\nu}{\int I_\nu d\nu} . \tag{2.43}$$

The line width can also be expresses as a function of wavelength, by using

$$\Delta\lambda \approx c\frac{\Delta\nu}{\nu_0^2} , \tag{2.44}$$

so that we get

$$\langle w_\lambda \rangle = c\frac{w_\nu}{\nu_0^2} . \tag{2.45}$$

By using equation 2.37 we can express the line width as a function of temperature,

$$\langle w_T \rangle = \left(\frac{cw_\nu}{\nu_0}\right)^2 \frac{m_A}{2k_B T_e} . \tag{2.46}$$

2.4.3 The Emission Line Intensity

We started this chapter by giving an expression for the emission line intensity, Equation 2.2,

$$I_\nu = \frac{h\nu}{4\pi}\int_0^s n_u A_{ul}\,\phi_\nu\,ds\,.$$

Then we discussed the processes which contribute to emission line formation and found that in CE we can substitute Equation 2.12 and 2.14 into this expression. The emission line intensity is then given by

$$I_\nu = \frac{h\nu}{4\pi}A_b\int_0^s \frac{n(X^m)}{n(X)}n_e n_H C_{lu}\phi_\nu ds\,. \tag{2.47}$$

It is not intuitive from this expression which variables we need to know to be able to compute the emission line intensity. Let us therefore define some functions which include some of these parameters, and write explicitly which variables they depend on.

Contribution Function

The contribution function is defined as

$$\mathrm{G}(T_e, n_e) = \frac{n(X^m)}{n(X)}C_{lu}\,. \tag{2.48}$$

Since both the ionization fraction and the collision rate are dependent on the electron temperature (see Equation 2.10 and Section 2.3.4), so is the contribution function. Actually, it is strongly dependent on the temperature and weakly dependent on the electron density. The contribution function gives information about which temperature regimes in the stellar atmosphere that contribute to the emission line. A plot of the contribution function for two iron lines (Fe XI 188.2 Å and Fe XV 284.2 Å) and one sulfur line (S VIII 198.6 Å) made using the CHIANTI (Dere et al., 1997; Landi et al., 2006) function 'ch_synthetic' can be seen in Figure 2.2. Clearly the S VIII line originate at the coldest temperature regime, the Fe XI line at a warmer, and the Fe XV line at an even hotter temperature regime of the atmosphere. The contribution function is very narrow, thus we only need to consider a few dex[1] on each side of the temperature maximum, to include the regime where this function is non-zero.

Differential Emission Measure

We can also define the differential emission measure,

$$\mathrm{DEM}(T_e) = n_e n_H \frac{ds}{dT_e}\,. \tag{2.49}$$

[1]Dex is a measure of the difference in logarithmic values. E.g. the difference between $10^{5.5}$ and $10^{5.6}$ is one dex.

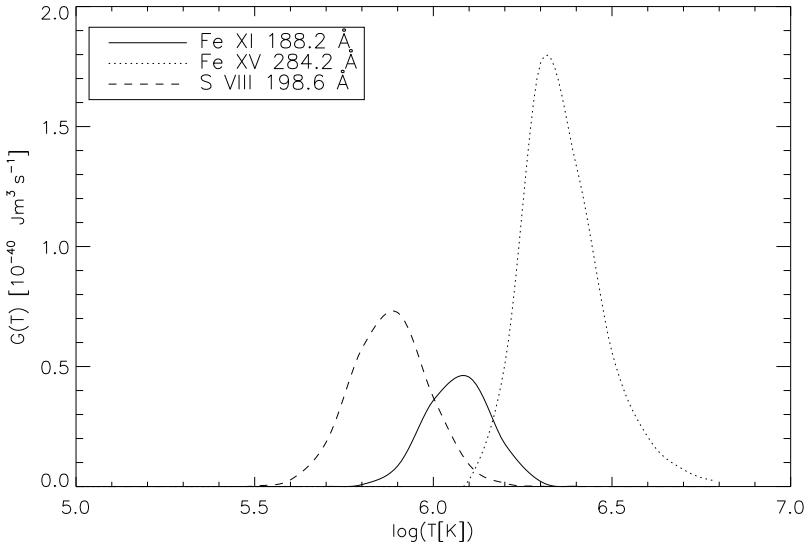

Figure 2.2: The contribution function for three UV lines, Fe XI 188.2 Å (solid), Fe XV 284.2 Å (dotted), and S VIII 198.6 Å (dashed).

The DEM gives an indication of the amount of plasma along the line of sight (s) that is emitting the radiation observed and has a temperature between T_e and $T_e + dT_e$.

The Branching Fraction

In Equation 2.2 we could also have included the branching fraction (Br_{ul}). This is a correction term that should be included if the electron has more than one lower level it can de-excite to. The branching fraction is the fraction of the ions that actually de-excites to the desired lower level, and is defined

$$Br_{ul} = \frac{A_{ul}}{\sum_k A_{uk}} \quad k < u \,, \tag{2.50}$$

where A_{uk} are the de-excitation rates for the different possible transitions from level 'u'.

Computing the Emission Line Intensity

By using our newly defined functions, the intensity can be written

$$I_\nu = \frac{h\nu}{4\pi} A_b \int_{\Delta T} G(T_e, n_e)\, \mathrm{DEM}(T_e)\, \phi \, dT_e \,, \tag{2.51}$$

where ΔT is the area where the contribution function is non-zero as explained above. The first part of this expression is as a first approximation considered

constant through the solar atmosphere, while the contribution function and DEM are functions of the electron density and temperature. To compute the emission line intensity we thus need to know how the electron temperature (T_e) and the density (n_e, n_H) vary as functions of time (t) and height (z). That is, we need to solve the hydrodynamic plasma equations.

2.5 The Hydrodynamic Plasma Equations

When describing the flow of plasma and gases it is common to use the hydrodynamic equations characterized by the density (ρ), velocity (u), and internal energy (e). We are actually interested in the temperature, which is related to the internal energy, $e \propto \rho T_e$.

We assume the magnetic field to be strong, that is that the tension in the magnetic field p_B (a magnetic analogous to pressure) is much stronger than the pressure p_g,

$$\beta = \frac{p_g}{p_B} = \frac{2\mu_0 n k_B T}{B^2} \ll 1\,, \tag{2.52}$$

where $\mu_0 = 4\pi \times 10^{-7}$ H/m is the magnetical permeability of empty space, n is the particle number density, and B is the magnetic field strength. When this is the case the plasma dynamics have to follow the magnetic field lines, and it is safe to restrict our calculations in one dimension along the magnetic field.

We consider a transition region flux tube with length z of time independent area, $A(z) = constant$, and assume the atmosphere to be homogeneous in the direction normal to z within the tube.

2.5.1 The Conservation Equations

As stated above, in a low-β plasma we can use the conservation equations in one spatial dimension.

Conservation of Mass

$$\frac{\partial \rho}{\partial t} + \frac{\partial}{\partial z}(\rho u) = 0 \tag{2.53}$$

This equation state that there are no sources or sinks for matter.

Conservation of Momentum

$$\rho \frac{\partial u}{\partial t} + \rho u \frac{\partial u}{\partial z} = -\frac{\partial}{\partial z}(p + Q) - \rho g_{\parallel}\,, \tag{2.54}$$

where $g_{\parallel}$ is the absolute value of the component of gravity parallel with the magnetic field, and the pressure is given by the ideal gas law,

$$p = \frac{\rho k_B T}{\overline{m}}\,. \tag{2.55}$$

To ensure a continuous solution through the shocks that may develop, we add an artificial viscous pressure (von Neumann and Richtmyer, 1950).

$$Q = \begin{cases} \frac{4}{3}\rho l^2 \left(\partial u/\partial z\right)^2 & \text{for } (\partial u/\partial z) < 0 \\ 0 & \text{for } (\partial u/\partial z) \geq 0 \end{cases} , \tag{2.56}$$

where l is chosen to be some fraction of the average grid spacing.

Conservation of Energy

$$\frac{\partial}{\partial t}(\rho e) + \frac{\partial}{\partial z}(\rho u e) + (p + Q)\frac{\partial u}{\partial z} = \frac{\partial}{\partial z}\left(F_c + F_r + F_h\right) , \tag{2.57}$$

where the internal energy (e) is the sum of the thermal and ionization energy and the source and sink terms on the right hand side are:

- the conductive flux (F_c)
- the radiative losses ($\partial F_r/\partial z$)
- the heating function (F_h)

We give more details about how these are computed in Section 3.1.1.

Chapter 3

The Simulation Code

In this chapter we give an introduction to our numerical analysis. First we explain what our problem is and why the solution has to be found numerically. Then we examine how our simulation code computes the solution to our problem. Finally, we describe how input is given to the program.

3.1 The Physical Problem

The aim of the thesis is to examine how the intensity and Doppler velocity of the emission lines detected by EIS respond to changes in the solar atmosphere. The intensity is computed from Equation 2.47

$$I_\nu = \frac{h\nu}{4\pi} A_b \int_0^s \frac{n(X^m)}{n(X)} n_e n_H C_{lu} \phi_\nu ds \,.$$

As we discussed in Section 2.3, the ionization fraction $\frac{n(X^m)}{n(X)}$ is determined by the rate equation (Equation 2.16),

$$\frac{\partial n(X^m)}{\partial t} + \frac{\partial}{\partial z}(n(X^m)u) = \text{ Sources}(T_e, n_e) - \text{ Sinks}(T_e, n_e) \,.$$

The sources and sinks in this equation are determined by the electron temperature and to a smaller degree by the electron density. How these parameters vary as a function of time and space are described by the conservation equations.

As explained in Section 2.5, we consider the magnetic field to be strong, $\beta \ll 1$, which restricts the plasma to follow the magnetic field lines. Thus we can use the one dimensional conservation equations given by Equations 2.53, 2.54, and 2.57:

$$\frac{\partial \rho}{\partial t} + \frac{\partial}{\partial z}(\rho u) = 0$$

$$\rho \frac{\partial u}{\partial t} + \rho u \frac{\partial u}{\partial z} + \frac{\partial}{\partial z}(p + Q) - \rho g_\parallel = 0$$

$$\frac{\partial}{\partial t}(\rho e) + \frac{\partial}{\partial z}(\rho u e) + (p+Q)\frac{\partial u}{\partial z} - \frac{\partial}{\partial z}\left(F_c + F_r + F_h\right) = 0$$

In Section 2.5.1 we did not go into the details about how we compute the sources and sinks in the energy equation. We look at this in the following section.

3.1.1 Energy Sources and Sinks

Radiative Losses

We consider radiative losses from the transition region to be optically thin. This should be a reasonable assumption, except for the Ly-α line which can be treated as effectively thin (cf. Section 2.1).

We calculate the radiative loss by summing up the losses from the individual processes

$$\frac{\partial F_r}{\partial z} = L_r = n_e \sum h\nu_{ul} n_l C_{lu} + L_{rec} + L_{ff}\,. \tag{3.1}$$

The resonance line losses are calculated by summing over all ionization stages of the major elements hydrogen, helium, carbon, oxygen, neon, nitrogen, and iron. L_{rec} is the loss from recombinations and L_{ff} is the loss from bremsstrahlung, which becomes important when the temperature exceeds 1 MK.

Conductive Flux

The conductive flux is mainly carried by electrons, and since the magnetic field is strong, the electrons can only run parallel with the magnetic field. Energy is transported away from the hot corona and down to the colder chromosphere.

The conductive flux is computed according to Spitzer (1962)

$$F_c = -\kappa_0 T_e^{5/2} \frac{dT_e}{dz}\,, \tag{3.2}$$

where $\kappa_0 = 1.1 \times 10^{-11}$ $\mathrm{Jm^{-1}s^{-1}K^{-7/2}}$. The heat conduction is not dependent of the number of electrons, only of the temperature and the temperature gradient.

Heating Function

The heating function is the main heat source of the corona, and it is not well known. We will not go into the physical details about it here, but only focus on the way the heat is distributed.

In our model the left and right hand side of the loop are heated independently. At the left hand side we add constant heat flux from $z = 0$ Mm and up to a given point z_0^{left}. From this point to the center of the loop the heat input decays exponentially with scale height z_H^{left}. Similarly, from the right hand side, the heat flux is constant from $z = 15$ Mm and down to a given point z_0^{right}, from where it decays exponentially with scale height z_H^{right}, to the center of the loop. The heating amplitudes $F_{h,0}$, can also be differing for the two sides of the loop.

The energy flux is for the left hand side given by

$$F_h(z) = F_{h,0}\, m(z_H, z_0) \begin{cases} 1 & \text{if} \quad z \leq z_0 \\ e^{-\frac{z-z_0}{z_H}} & \text{if} \quad z_0 < z < L/2 \end{cases} , \tag{3.3}$$

where L is the length of the loop. (Similar for the right hand side, but heating in the opposite direction.) The scaling function $m(z_H, z_0)$ is included to ensure that all of the energy is deposited into the chosen area, and is given by

$$m(z_H, z_0) = \frac{1}{1 - e^{-\frac{Z_{dis}}{\Delta z}}} , \tag{3.4}$$

where the heating distance is given by

$$Z_{dis} = \frac{L}{2} - z_0 . \tag{3.5}$$

The actual heating rate, i.e. the energy deposition per unit time and unit volume, is given by the negative divergence of the energy flux

$$W_h(z) = -\frac{dF_h}{dz} = \begin{cases} 0 & \text{if} \quad z \leq z_0 \\ z_H^{-1} F_h & \text{if} \quad z_0 < z < L/2 \end{cases} . \tag{3.6}$$

An example of the energy deposition is shown in Figure 3.1. A given total energy will produce higher temperatures when deposited in the corona than in the transition region or chromosphere, since there are fewer particles to share the energy.

3.1.2 Summary

To solve our problem we need to compute the rate equations, which are determined by the conservation equations. We found in the previous section that the energy equation has radiative losses ($\partial F_r / \partial z$) as one of its sink terms. The radiative losses are again determined by the rate equation. We clearly need a system that solves the conservation equations and the rate equations consistently. This system is a coupled set of non-linear equations, too large to be solved analytically. Therefore, we turn to numerically modeling and use the numerical simulation code TTRANZ (Hansteen, 1991).

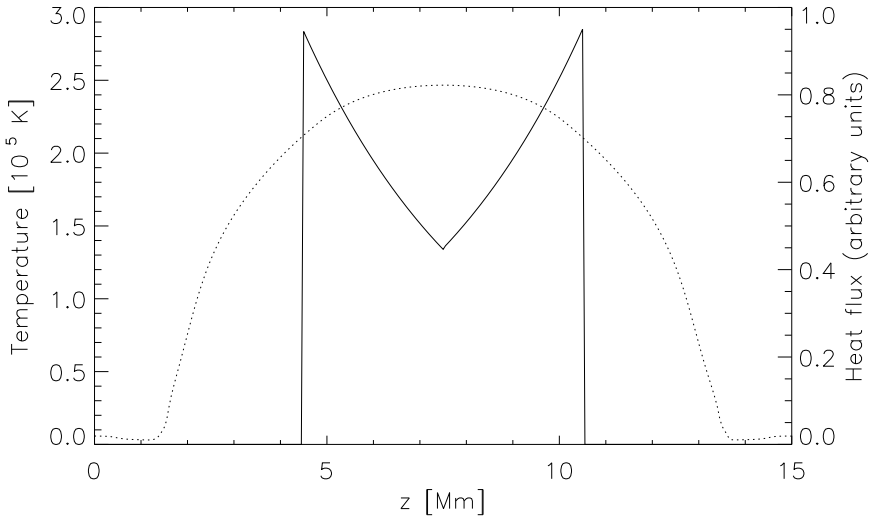

Figure 3.1: The gradient of the heating function, $W_h(z)$ (solid line) using $z_0^{left} = 4.5$ Mm, $z_0^{right} = 10.5$ Mm, and $z_H^{left} = z_H^{right} = 4.0$ Mm, over-plotted with a typical loop temperature distribution (dotted line).

3.2 TTRANZ

TTRANZ is a numerical simulation code made to study the ionization state and its coupling to line formation in the transition region. TTRANZ solves the conservation equations of mass, momentum, and energy consistently with the ionization rate equations, computed with the radiative losses consistent with the ionization state we included in the energy equation.

TTRANZ solves an initial value problem, that is, we give as input the solution to the problem at time $t = t_0$, and then the program tries to calculate the solution at the next time step. When the state at the new time is known, TTRANZ uses it as an input to calculate the solution at the next, and so forth, until a given time or number of time steps are reached. We will come back to the details about how this is done below.

3.2.1 Discretization

Our first concern is to transform a mathematically formulated problem to one that can be solved numerically. Thus, we have to discretize the equations we wish to solve, that is, the conservation equations and the rate equations. We choose to use the finite difference method. The equations are to be solved in one spatial dimension and in time. The temporal and spatial discretizations are done in two different ways.

Temporal Discretization

The temporal discretization is done by using a weighted average of the known, old value (superscript 'o') and the unknown, new value (superscript 'n'),

$$y = \theta y^{(n)} + (1-\theta) y^{(o)}, \qquad 0 \le \theta \le 1\,. \tag{3.7}$$

We will come back to the details about how the new solution is found in Section 3.2.2. For $\theta = 1$ this is an explicit scheme, for $\theta \neq 1$ this is an implicit scheme, and for $\theta = \frac{1}{2}$ this method is called the Crank-Nicolson method. We use $\theta = 0.55$.

Spatial Discretization

Even though we are doing our calculations in one dimension, we are still dividing our space (a line) into boxes, where each box only has two interfaces where plasma and heat can flow. The scalars, such as the density and internal energy, are defined in the center of the boxes, while the vectors, such as the velocity, are defined at the interfaces.

The spatial discretization is computed using the second order upwind scheme of van Leer (1974). Upwind means that we are choosing which cells to involve in the calculation by looking at which direction the advected quantity is moving. For instance, if the velocity is moving to the right we are using cells to the left of our point to estimate the momentum flux.

A second order method requires information from the two nearest neighbor cells on either side of the computational cell being considered. This results in a block penta-diagonal system which needs to be inverted.

The Adaptive Grid

In order to resolve the large gradients and shocks that might arise, the equations are formulated on an adaptive grid. That is, the mesh points are moved towards the regions where the spatial gradients are large, so that the grid density is greatest where it at any time is needed the most. The grid step can vary in size both as a function of the loop length (z) and time (t).

The grid is allocated to follow gradients in the dynamic variables. The spatial grid density, $\rho_z = 1/(z_{i+1} - z_i)$, is computed by solving the grid equation of Dorfi and Drury (1987),

$$\rho_z(z) \propto R(z) \equiv \sqrt{1 + \left(\frac{z_{av}}{f_{av}} \frac{df}{dz}\right)^2}\,, \tag{3.8}$$

where R is the required resolution, f represent any quantity that the grid should respond to; e.g. u or T_e. The subscript 'av' means that we should use some appropriate average of the subscripted variable, with f_{av} used to

weight quantities for which resolution is vital. There is a limit on how far a given mesh point is allowed to move from one time step to the next.

Allowed changes in grid position as a function of time are controlled in a similar manner.

3.2.2 Calculating the Next Time Step

To go from one (known) time step to the next we have to solve the coupled set of non-linear equations including the grid equation, the conservation equations, and the rate equations for hydrogen and helium. The rate equations for the other elements are calculated separately afterwards.

Mathematically the set of equations can be written

$$F_i(x_1, x_2, ..., x_N) = 0, \qquad i = 1, 2, ..., N\,, \tag{3.9}$$

where $\mathbf{F}$ is the vector containing the conservation equations and rate equations, while $\mathbf{x}$ is the vector containing our variables, z, ρ, n, T_e, $n_{HI}...n_{Hm_H}$, $n_{HeI}...n_{Hem_{He}}$, and n_e. Assuming that we have m_H levels of hydrogen and m_{He} levels of helium, this gives $4 + m_H + m_{He} + 1$ variables at each depth (grid) point. In total we then have

$$\text{ndep} \times (5 + m_H + m_{He}) \tag{3.10}$$

unknowns to be solved at each time step, where ndep is the number of depth points.

Each of the functions in $\mathbf{F}$ can be expanded in a Taylor series

$$F_i(\mathbf{x} + \delta\mathbf{x}) = F_i(\mathbf{x}) + \sum_{j=i}^{N} \frac{\partial F_i}{\partial x_j}\delta x_j + O(\delta\mathbf{x}^2)\,. \tag{3.11}$$

If F_i is linear in x_j then $\partial F_i/\partial x_j$ is independent of x_j and our problem is linear. Hence, the solution for δx_j will converge immediately. If F_i is non-linear, we must iterate to the correct solution at time step 'n'.

Let us denote the current and next iteration step with superscript 'k' and '$k+1$', respectively, and neglect the terms of order $\delta\mathbf{x}^2$ and higher, so that

$$\mathbf{x}^{(k+1)} = \mathbf{x}^{(k)} + \delta\mathbf{x}\,. \tag{3.12}$$

By introducing vector form and writing the Jacobian $\frac{\partial F_i}{\partial x_j} \equiv J_j$ we get

$$\mathbf{F}(\mathbf{x}^{(k+1)}) = \mathbf{F}(\mathbf{x}^{(k)}) + \mathbf{J}\delta\mathbf{x} = 0\,. \tag{3.13}$$

The correction term can be found by inverting the Jacobian

$$\delta\mathbf{x} = \mathbf{J}^{-1}(-\mathbf{F}(\mathbf{x}^{(k)}))\,. \tag{3.14}$$

Since the equations in **F** are non-linear we can not find the correct solution directly, but if we are sufficiently close to the solution, this method should converge. We can now use these new values to recalculate the radiative losses, and put them back into the conservation equations for a better calculation to be done.

Iterating like this until the correction is less than some preset value is called the Newton-Raphson method. The convergence of this method is quadratic, meaning that an error of magnitude $\epsilon < 1$ reduces to ϵ^2 in the next step. This is a very fast convergence, as long as it converges at all. If the initial guess is too far from the solution it never converges, and we have to restart the calculation of the new time step with a shorter dt. In our case the convergence usually takes 4-5 iterations.

3.3 Input

We have now discussed how TTRANZ solves our problem, but we have not said anything about how we are feeding the program with information. Since TTRANZ solves an initial value problem, the initial state must be given. In addition, we must inform the program about what our environment looks like. This is given through the atomic models and the initialization file 'init'. We take a look at these three input sources below.

3.3.1 The Atomic File

Every atom that we want to include in the model must have its one atomic file, where all the information about the atom is listed. We have included the elements hydrogen, helium, carbon, oxygen, iron, and magnesium. We are interested in emission lines from helium and iron and therefore, we return to the details about these elements in Chapter 4. The other elements are included because they are among the most abundant elements in the Sun, and therefore these atoms play an important part in the radiative losses at temperatures around 10^5 K. Thus, it is important to calculate their states correctly also when they are driven out of equilibrium.

The atomic model used by TTRANZ is defined by a text file structure designed by Carlsson (1986, and later modifications) for the computer program MULTI. The file is divided into different parts containing the needed input:

- the element abundances
- the energy levels
- the excitation and de-excitation rates
- the ionization rates

We will take a look at the different parts of the file below. Lines marked with '$*$' are comments for the reader and are not used by the program. We use examples from the iron atomic model

Most of he data in the atomic files are from the HAO-DIAPER package (Judge and Meisner, 1994). We have made some modifications to the iron and helium atomic models, which we discuss in details in Sections 4.2 and 4.3.

We use the same set of atomic files throughout the thesis.

Element Abundances

The element abundance is considered constant through the solar atmosphere and is calculated relative to the hydrogen abundance according to the formula

$$\frac{n(X)}{n_H} = 10^{Ab_{dex}-12}. \tag{3.15}$$

Ab_{dex} is listed in the atomic file like this:

```
fe rrum
*
* Ab_dex [dex]  mass[mu]   atom(Z)
     7.67        55.85       26
```

Energy Levels

For every atom we need to state which energy levels to include. There is a balance between including as few levels as possible to ensure computational efficiency while still retaining enough levels to maintain physical fidelity. That is, to ensure that there are enough levels for the ionization balance and intensity output to be correct.

In this section of the atomic file we list the energy value in cm^{-1}, the multiplicity, and the spectroscopic notation for each energy level:

```
* #levels      #transitions      #continuum      #fix
    33             31                0             0
*
* energy       multiplicity        spectr. notation        ion
        0.000      1.00            'fe vii 4s2 1se 0'       7
  1008184.600      2.00            'fe viii 4s 2se 1/2'     8
  2226555.500      1.00            'fe ix 3p6 1se 0'        9
  4122265.250      6.00            'fe x 3p5 2po 3/2'       10
  4137948.450      2.00            'fe x 3p5 2po 1/2'       10
      [..]
```

Excitation and De-excitation Rates

In addition to listing the energy levels we also need to list the possible transitions between the different energy levels and what their transition rates are.

The radiative rates are listed like this:

```
* radiative transitions
* upper lower  f-value           A coefficient
    10   5     5.900e-01  [..]   2.22e+11       [..]
        [..]
```

Even though both the oscillator strength (f) and the Einstein A coefficient are listed in the atomic file, TTRANZ only read the oscillator strength. Thereafter it uses Equation 2.7 to calculate the Einstein A coefficient,

$$A_{ul} = 6.671 \times 10^{15} \frac{\omega_l}{\omega_u} \frac{f_{ul}}{\lambda^2} \,.$$

The collision rates are found from CHIANTI (Dere et al., 1997; Landi et al., 2006), which uses the design by Burgess and Tully (1992). They are listed in the atomic file like this:

```
* temperature spline (2 indicates two knots)
temp
    2    1.00000e+06     1.00000e+07
*
* thermally averaged collision strengths
ohm
* lower  upper
    5     6     2.69e-01    2.69e-01
```

TTRANZ uses the thermally averaged collision strength (Υ). When we add lines and need to find this quantity we first use the CHIANTI procedure 'rate_coeff.pro' to find the rate coefficient C_{lu}, and thereafter Equation 2.10 to find Υ,

$$\Upsilon_{lu}(T_e) = C_{lu} \frac{\omega_l}{C_0} T_e^{1/2} \, e^{\Delta E / k_B T_e} \,.$$

The energy differences are taken from CHIANTI.

Ionization and Recombination Rates

In the atomic file we also need to include the possible ionization and recombination rates from the different levels in one ion to the different levels in adjacent ions.

The radiative recombination rates are given by Shull and van Steenberg (1982), and listed in the atom file like this:

```
 shull82
* lower upper    acol      tcol      arad      xrad
   1     2     0.00e+00  1.45e+06  4.12e-11  7.59e-01
*
*                adi       bdi       t0        t1
                2.91e-01  2.29e-01  7.73e+05  6.54e+05
```

The electron impact ionization rates are given by Arnaud and Raymond (1992), and listed in the atomic file like this:

```
 * electron impact ionization coefficients
 ar85-cdi
 * lower upper
    1     2
 * #shell
    3
 *  potential (eV)   A        B        C        D
    124.20         14.60    -4.36     5.98   -10.50
    180.00         67.90   -20.60     9.82   -53.70
    220.90         15.60    -2.29     2.30   -10.60
```

The autoionization rates are given by Arnaud and Raymond (1992), and listed in the atomic file like this:

```
 ar85-cea
 * lower upper
    1     2
 * Autoionization rate
 1.000e+00
```

The dielectronic recombination rates are given by Burgess (1965), and listed in the atomic file like this:

```
burgess
 * lower upper  rate
   8      11    1.00e+00
```

3.3.2 The Init File

Input from the user to the program is given through the init file. In this file we state what kind of simulation should be done and which considerations that should be taken during the program run. The init file must be updated before each simulation, in contrast to the atomic files, which are made only once for one special type of study.

The init file is divided into two parts. In the first section we set the time length of our simulation, how often we save data, and how many iterations we allow. Here we also specify quantities like the weighting in the temporal discretization, the correction limit for the Newton-Raphson method, the maximum allowed change in the grid, which elements to include in the simulations, and so forth.

In the second part of the init file we decide the length of the loop, where the heating is added, and what the heating scale height is. Here we can also choose to add waves of different amplitudes to the system. We will address the specific input in this part of the init file when discussing our simulations in Chapter 5.

3.3.3 The Initial Solution

When starting TTRANZ we need the solution to our equations at time $t = t_0$, the initial values. The most common way to solve this challenge is to restart the program with the output we have from an earlier run. E.g. if we want a model with a different temperature structure than we already have, we change the heating function in the init file, start the program and let it simulate an hour or two (solar time), until the loop has settled. Then we have the starting point we want for our new simulation.

Chapter 4

The Atomic Model

In this chapter we describe our atomic models. Recall from Section 3.3.1 that every atom included in our model must be defined in an atomic file, where all the energy levels, transitions, and rates are listed. We limit ourselves to go through in detail the atoms which have interesting lines in the EIS wavelength band.

Before designing our atoms, we first have to look at the possibilities and limitations of the spectrograph we are analyzing. We identify the spectral lines usable for our purpose and plot the contribution functions for the most interesting ones. Thereafter, we look in details at the atoms we choose to use lines from, that is iron and helium. We identify which energy levels and lines to include and check that our ionization balances are correct.

4.1 Identifying Spectral Lines

We want to simulate detections from the extreme ultraviolet (EUV) imaging spectrograph (EIS) on board Hinode (Solar-B). EIS can observe in two wavelength intervals, 170–210 Å (the short wavelength band) and 250–290 Å (the long wavelength band). It is expected to have a spectral resolution of 3 km/s for Doppler velocities (Culhane et al., 2007). Some EIS specifications are listed in Table 4.1. We have to consider these specifications when choosing which spectral lines to examine.

Wavelength coverage	170–210 Å and 250–290 Å
Dispersion	0.0223 Å/CCD pixel
Pixel equivalent width	34.3 km/s for 195 Å, and 23.6 km/s for 284 Å

Table 4.1: EIS specifications.

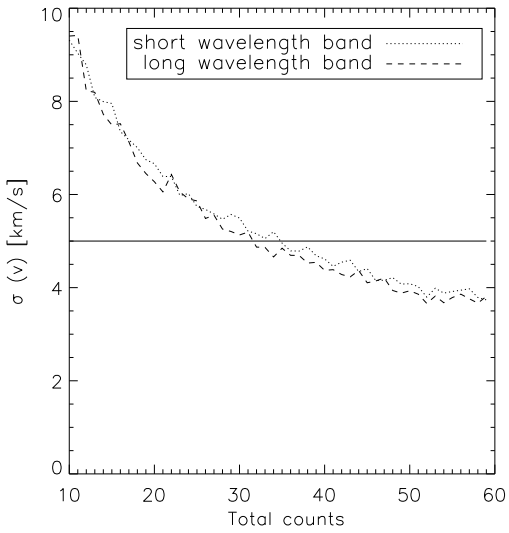

Figure 4.1: Root-mean-square error in velocity due to counting statistics for the short (dotted line) and long wavelength band (dashed line) as a function of total number of counts.

4.1.1 Resolution Requirements

We are interested in examining the changes to the EIS spectral lines caused by velocity changes in the solar atmosphere. Some of these velocities are caused by oscillations with periods on the order of three or five minutes, and we expect the velocity amplitudes to be in the order of 5–10 km/s. To resolve these events we need to find spectral lines with which it is possible to measure the velocity with an accuracy better than 5 km/s, with less than about 60 seconds of exposure. Since EIS has a pixel equivalent width of about 35 km/s for the short wavelength band and 25 km/s for the long wavelength band (see Table 4.1), we clearly need sub-pixel accuracy to fulfill our demands.

As noted in Section 2.4.1, an emission line is not an infinitely thin line, but is in reality smeared out according to a line profile. Because of this, all photons from one line are detected not only in one pixel, but are by EIS actually detected in 5–7 neighboring pixels. By assuming that this emission line has a given shape, e.g. Gaussian, we can estimate the maximum peak better than the accuracy of the pixel equivalent width.

When using this technique we of course have to account for the counting (Poisson) statistics, which is related to the total number of counts. The more counts we get, the better our assumption of the line's profile will be, and thus also the assumption of the position of the peak.

In Figure 4.1 we have plotted the root-mean-square error in velocity due

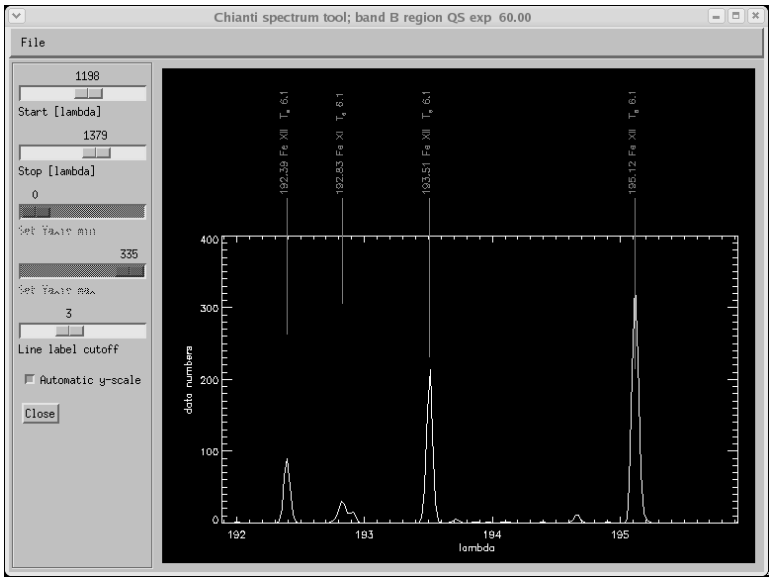

Figure 4.2: A synthetic spectra from a part of the short wavelength region made with 'xspecplot.pro', simulating an exposure time of 60 seconds with quiet sun.

to counting statistics. Here we have assumed that the lines are Gaussian and the full width at half maximum (FWHM) is 0.05 Å (Mariska, 2005). To get better resolution than 5 km/s we need 35-40 counts in total from the emission line, both for the short and the long wavelength band.

4.1.2 Estimating the Number of Counts

To find the lines that give more than 35–40 counts in 60 seconds, which is the criteria to resolve the expected velocity changes, we use the Solarsoft (Bentely and Freeland, 1998) program 'xspecplot.pro'. This program is based on the results from the CHIANTI atomic database (Dere et al., 1997; Landi et al., 2006) and accounts for EIS' effective area[1]. From this program we are able to read out the maximum intensities for a line in data number[2] (DN $= N_{\max}$) as a function of the wavelength. See Figure 4.2. We need to find how many counts we get in total (N_{tot}) for each spectral line. Therefore, we need a relation between N_{tot} and $N_{\max}$. This can be found if we assume the line to be Gaussian.

[1]The effective area describes how sensitive the detector is as a function of wavelength.
[2]Data number is the same as counts per pixel.

Relation Between $N_{\mathbf{max}}$ and $N_{\mathbf{tot}}$ for a Gaussian

The equation for a Gaussian distribution $G(x)$ with area $N_{\rm tot}$ (which can be associated by the total number of counts from one line) and standard deviation σ is given by

$$G(x) = \frac{N_{\rm tot}}{\sigma\sqrt{2\pi}} e^{-\left(\frac{x^2}{2\sigma^2}\right)} \,. \tag{4.1}$$

The relation between $N_{\rm max}$ and $N_{\rm tot}$ is given by

$$\begin{aligned} G(0) = N_{\rm max} &= \frac{N_{\rm tot}}{\sigma\sqrt{2\pi}} \\ &\Downarrow \\ N_{\rm tot} &= N_{\rm max} \cdot \sigma\sqrt{2\pi} \,. \end{aligned} \tag{4.2}$$

The half maximum is found when $e^{-\left(\frac{x^2}{2\sigma^2}\right)} = \frac{1}{2}$, that is $x = \sigma\sqrt{2\ln 2}$. FWHM is twice this size, and thus given by

$$\text{FWHM} = 2\sigma\sqrt{2\ln 2} \,. \tag{4.3}$$

This leads to the standard deviation

$$\sigma = \frac{\text{FWHM}}{2\sqrt{2\ln 2}} \,. \tag{4.4}$$

Putting this into Equation 4.2 gives

$$\begin{aligned} N_{\rm tot} &= N_{\rm max} \cdot \text{FWHM} \cdot \frac{\sqrt{\pi}}{2\sqrt{\ln 2}} \\ &\approx N_{\rm max} \cdot \text{FWHM} \,. \end{aligned} \tag{4.5}$$

If we assume that we need a total of at least 40 counts from each line, this relates to DN as

$$DN = N_{\rm max} = \frac{N_{\rm tot}}{\text{FWHM}} = \frac{40 \text{ counts}}{\frac{0.05\text{Å}}{0.0223\text{Å/pix}}} \approx 18 \text{ counts/pix} \,, \tag{4.6}$$

where we have converted the FWHM of 0.05 Å into pixels by dividing by the dispersion, 0.0223/pix (see Table 4.1). To be able to resolve the velocity better than 5 km/s, we must thus have a spectral line with maximum counts per pixel greater than 18.

Wavelength [Å]	Ion	Temp. [lg(T)]	DN [counts/pix]	Lower level	Upper level
Short band					
184.5	Fe X	6.0	18	$3p^5\ ^2P_{3/2}$	$3p^4\ (^1D)\ 3d\ ^2S_{1/2}$
186.9	Fe XII	6.1	21	$3p^3\ ^2D_{5/2}$	$3p^2\ (^3P)\ 3d\ ^2F_{7/2}$
188.2	Fe XI	6.1	65	$3p^4\ ^3P_2$	$3p^3\ (^2D)\ 3d\ ^3P_2$
192.4	Fe XII	6.1	77	$3p^3\ ^4S_{3/2}$	$3p^2\ (^3P)\ 3d\ ^4P_{1/2}$
192.8	Fe XI	6.1	26	$3p^4\ ^3P_1$	$3p^3\ (^2D)\ 3d\ ^3P_2$
193.5	Fe XII	6.1	182	$3p^3\ ^4S_{3/2}$	$3p^2\ (^3P)\ 3d\ ^4P_{3/2}$
195.1	Fe XII	6.1	285	$3p^3\ ^4S_{3/2}$	$3p^2\ (^3P)\ 3d\ ^4P_{5/2}$
198.6	S VIII	5.9	27	$2p^5\ ^2P_{3/2}$	$2s\ 2p^6\ ^2S_{1/2}$
202.0	Fe XIII	6.2	72	$3p^2\ ^3P_0$	$3p\ 3d\ ^3P_1$
203.2	Fe XIII	6.2	2	$3p^2\ ^3P_1$	$3p\ 3d\ ^3P_0$
203.8	Fe XIII	6.3	16	$3p^2\ ^3P_2$	$3p\ 3d\ ^3D_3$
Long band					
256.3	He II	4.9	22	$1s\ ^2S_{1/2}$	$3p\ ^2P_{3/2}\ (P_{1/2})$
274,2	Fe XIV	6.3	20	$3p\ ^2P_{1/2}$	$3s\ 3p^2\ ^2S_{1/2}$
284,2	Fe XV	6.3	30	$3s^2\ ^1S_0$	$3s\ 3p\ ^1P_1$

Table 4.2: Wavelength, temperature of peak abundance, spectral notation, and counts per pixel (assuming quiet sun) for the chosen EIS spectral lines. Full shells are not included in the spectral notation.

4.1.3 Selected Lines

From 'xspecplot.pro' we find the spectral lines which have $N_{\max}$ higher than 18 for quiet sun with an exposure time of 60 seconds. Their wavelengths, temperatures of peak abundance, spectral notations, and data numbers are listed in Table 4.2. To this list we have also added the Fe XIII lines 203.2 Å and 203.8 Å, which can be used for density diagnostics in combination with the Fe XIII 202.0 Å line. He II 256.317 Å and 256.318 Å are for simplicity treated as only one line, He II 256.3 Å. This line is blended by Si X 256.4 Å.

The list include interesting lines from the atoms iron, helium, and sulfur. We have not included the element sulfur in our atomic model, but we will go through the two other elements in greater details below.

The Contribution Functions

As stated in Section 2.4.3, the contribution function gives information about which temperature interval an emission line is formed at. The temperature noted in Table 4.2 is the temperature where the contribution function has the greatest value. To get a better understanding about where the lines are formed we have plotted the contribution functions for our iron lines in Figure

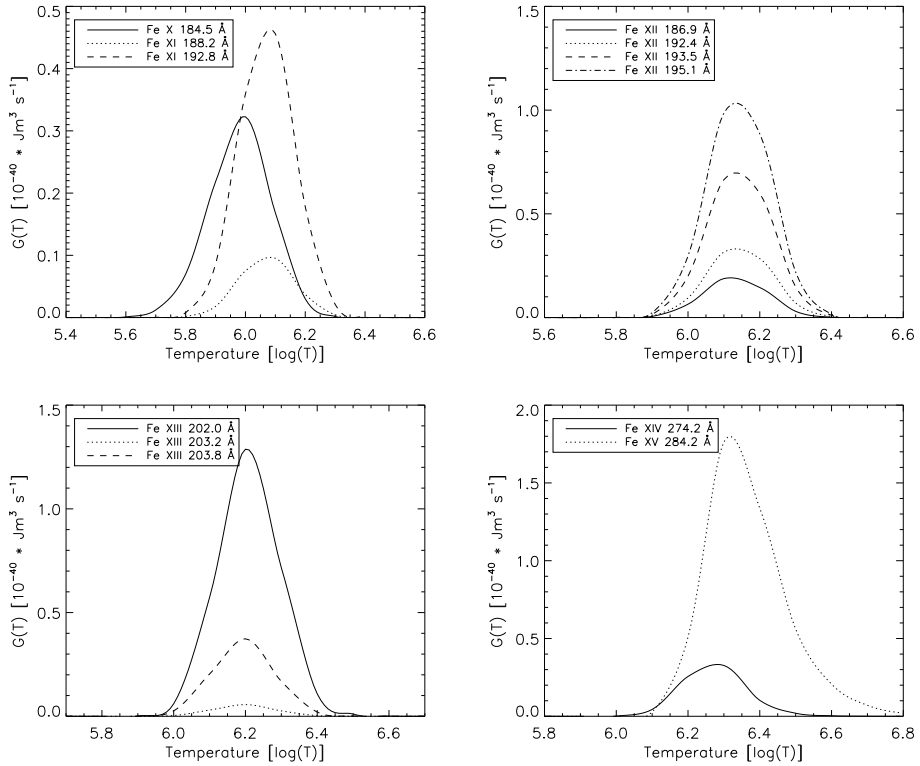

Figure 4.3: The contribution functions, G(T), for our interesting iron lines. Upper left: Fe X 184.5 Å (solid), Fe XI 188.2 Å (dotted), Fe XI 192.8 Å (dashed). Upper right: Fe XII 186.9 Å (solid), Fe XII 192.4 Å (dotted), Fe XII 193.5 Å (dashed), Fe XII 195.1 Å (dash-dotted). Lower left: Fe XIII 202.0 Å (solid), Fe XIII 203.2 Å (dotted), Fe XIII 203.8 Å (dashed). Lower right: Fe XIV 274.2 Å (solid), Fe XV 284.2 Å (dotted).

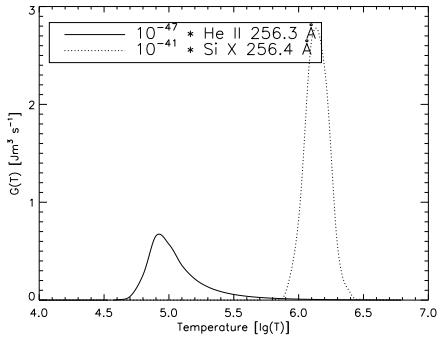

Figure 4.4: The contribution function, G(T), for the He II 256.3 (solid) and the Si X 256.4 blend (dotted).

4.3, and the helium line with the silicon blend in Figure 4.4.[3] Note that the helium and silicone lines are formed in two different temperature intervals, and that the silicone line's contribution function takes on much higher values than the helium one.

4.2 Designing the Iron Model

When we do numerical simulations it is important to decide to what degree we want to include physical details in the simulations. The more details we include, the more computationally demanding the simulations become. It is important to find the balance between computational complexity and accuracy. Because of this we have to pay attention to the information we include in the atomic model. In the following subsections we will go through the different iron ions and explain which levels we have chosen to include in our model.

To make our iron-model we use the HAO-DIAPER package (Judge and Meisner, 1994) as a starting point. Where this model lacks information we use the CHIANTI atomic database (Dere et al., 1997; Landi et al., 2006) to find the wavelength and spectral configuration, and the NIST online database (Ralchenko et al., 2005) to find the oscillator strength. We will come back to details about this below.

4.2.1 Included Ions

As can be seen from Table 4.2 we are interested in lines from the ions Fe X – Fe XV. If we include only these ions, the ionization balance would not be correct, because there exist other iron ions in the same temperature interval. Therefore, we must include extra iron ions, even if we are not interested in their lines. We choose to include the ions Fe VII – Fe XVIII in our model. Ions outside this interval will only marginally influence our results. We will come back to the ionization balance in Section 4.2.4.

4.2.2 Included Energy Levels

Now we have chosen which ions to include, and it is time to consider which energy levels to include for each of them. The de-excitation rates for most of the excited levels are much higher than the rates at which they are excited. Therefore, there are very few ions in the excited stages. As noted in Section 2.2.3, this is not the case for meta-stable levels. We include the ground level, which of course is the state in which most of the ions are, and the upper and lower levels of our lines. In addition, we must consider whether there are

[3]These figures are made with the CHIANTI procedure 'ch_synthetic' with data from Mazzotta et al. (1998).

any low-lying meta-stable levels which a notable fraction of the ions might be in. If so, these must be included too.

Ions Without Interesting Lines

We are not interested in lines from the ions Fe VII – Fe IX and Fe XVI – Fe XVIII. These are included only for the ionization balance to be correct. It does not matter for us whether the ions are in the ground or excited states, since this does not affect the ionization balance notably. Therefore, we only include the ground levels of these ions.

Ions With Interesting Lines

For the ions Fe X – Fe XV we are interested in the lines listed i Table 4.2. In addition to the levels listed in this table, we use the CHIANTI procedure 'show_pops.pro' to examine if there are any meta-stable levels that a notable part of the ions are in. We choose only to include levels with population higher than 5% of the total ion population. We go through the results below. The levels we include are summarized in Table 4.3, and the Grotrian diagrams[4] for the different ions can be seen if Figure 4.5.

Fe X has only one line we are interested in, 184.5 Å. We include the lower and upper level of this line, $3p^5\ ^2P_{3/2}$ and $3p^4\ (^1D)\ 3d\ ^2S_{1/2}$. The first is also the ground level of the ion. In addition this ion has one meta-stable level which has a substantial fraction of the ion's population (19%), $3p^5\ ^2P_{3/2}$, which we include. Fe X is plotted in the upper left panel of Figure 4.5.

Fe XI has two lines we are interested in, 188.2 Å and 192.8 Å. The first line has the ground level as its lower level, $3p^4\ ^3P_2$, while the second line has a meta-stable level as its lower level, $3p^4\ ^3P_1$. The lines have a common upper level, $3p^3\ (^2D)\ 3d\ ^3P_2$. In addition to these levels, we also include two meta-stable levels, $3p^4\ ^3P_0$ which has 6% of the ion's population and $3p^4\ ^1D_2$ which has 12%. Fe XI is plotted in the upper right panel of Figure 4.5.

Fe XII has four lines we are interested in, 186.9 Å, 192.4 Å, 193.5 Å, and 195.1 Å. The first line has $3p^3\ ^2D_{5/2}$ as its lower level while the three others have $3p^3\ ^4S_{3/2}$. Their upper levels are $3p^2\ (^3P)\ 3d\ ^2F_{7/2}$, $3p^2\ (^3P)\ 3d\ ^4P_{1/2}$, $3p^2\ (^3P)\ 3d\ ^4P_{3/2}$, and $3p^2\ (^3P)\ 3d\ ^4P_{5/2}$, respectively. In addition to these levels we also include the ground level, $3p^3\ ^2D_{3/2}$. Fe XII is plotted in the middle left panel of Figure 4.5.

[4]The Grotrian diagrams are made with the HAO-DIAPER procedure 'termdiag.pro'.

Ion	Spectr. not.	Pop.	Comment
Fe X	$3p^5\ ^2P_{3/2}$	66 %	Ground level, lower level
	$3p^5\ ^2P_{3/2}$	19 %	Meta-stable level
	$3p^4\ (^1D)\ 3d\ ^2S_{1/2}$	<1 %	Upper level
Fe XI	$3p^4\ ^3P_2$	53 %	Ground level, lower level
	$3p^4\ ^3P_1$	18 %	Meta-stable level, lower level
	$3p^4\ ^3P_0$	6 %	Meta-stable level
	$3p^4\ ^1D_2$	12 %	Meta-stable level
	$3p^3\ (^2D)\ 3d\ ^3P_2$	<1 %	Upper level
Fe XII	$3p^3\ ^2D_{3/2}$	12 %	Ground level
	$3p^3\ ^2D_{5/2}$	25 %	Meta-stable level, lower level
	$3p^3\ ^4S_{3/2}$	58 %	Meta-stable level, lower level
	$3p^2\ (^3P)\ 3d\ ^2F_{7/2}$	<1 %	Upper level
	$3p^2\ (^3P)\ 3d\ ^4P_{1/2}$	<1 %	Upper level
	$3p^2\ (^3P)\ 3d\ ^4P_{3/2}$	<1 %	Upper level
	$3p^2\ (^3P)\ 3d\ ^4P_{5/2}$	<1 %	Upper level
Fe XIII	$3p^2\ ^3P_0$	15 %	Ground level, lower level
	$3p^2\ ^3P_1$	30 %	Meta-stable level, lower level
	$3p^2\ ^3P_2$	44 %	Meta-stable level, lower level
	$3p^2\ ^1D_2$	10 %	Meta-stable level
	$3p\ 3d\ ^3P_1$	<1 %	Upper level
	$3p\ 3d\ ^3P_0$	<1 %	Upper level
	$3p\ 3d\ ^3D_3$	<1 %	Upper level
Fe XIV	$3p\ ^2P_{1/2}$	54 %	Ground level, lower level
	$3p\ ^2P_{3/2}$	46 %	Meta-stable level
	$3s\ 3p^2\ ^2S_{1/2}$	<1 %	Upper level
Fe XV	$3s^2\ ^1S_0$	92 %	Ground level, lower level
	$3s\ 3p\ ^1P_1$	<1 %	Upper level

Table 4.3: Spectral notation (spectr. not.) and population percentage (pop.) for the included levels in our iron atomic model. Only states with more than 5% of the ion's population and the states participating in making our lines are included. The percentages have been rounded and full shells are not included in the spectral notation.

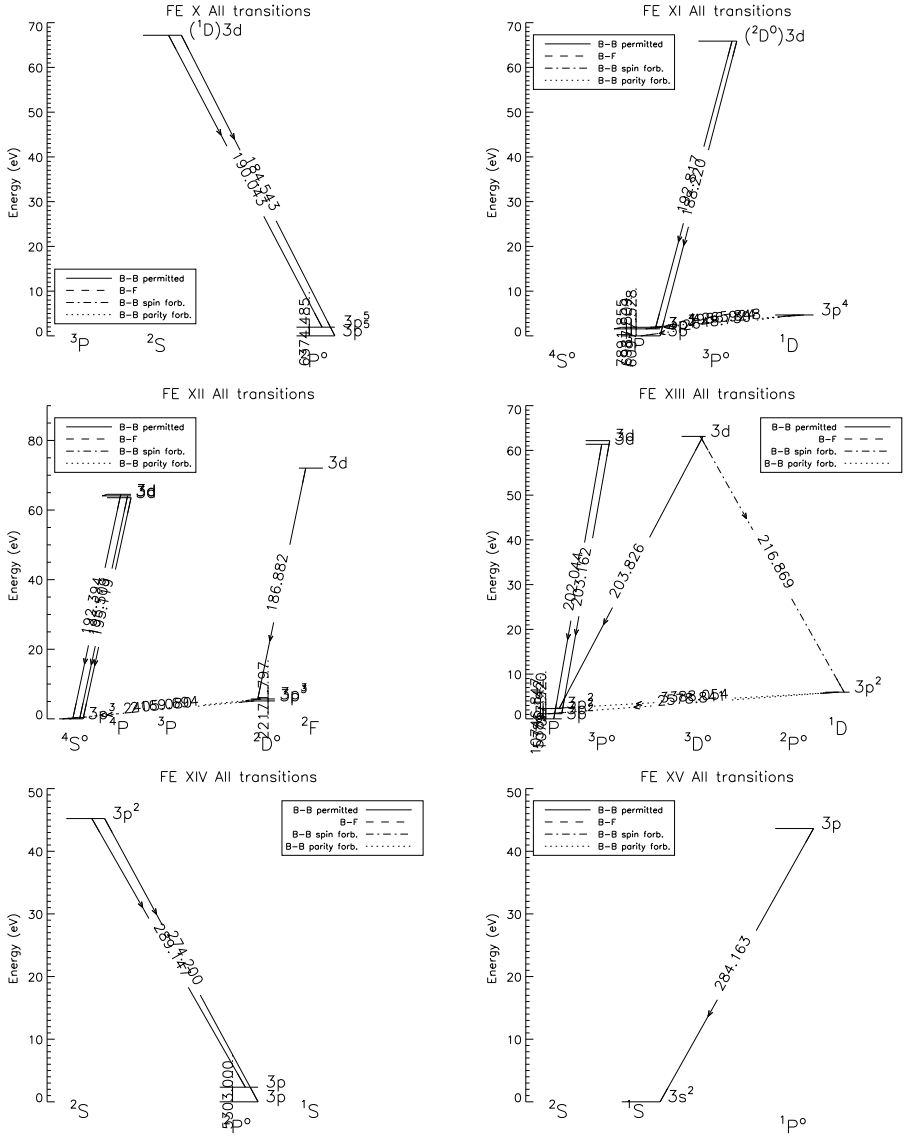

Figure 4.5: Grotrian diagrams for the iron ions: Fe X (upper left), Fe XI (upper right), Fe XII (middle left), Fe XIII (middle right), Fe XIV (lower left), and Fe XV (lower right).

Fe XIII has three interesting lines, 202.0 Å, 203.2 å and 203.8 Å. The first line has the ground level as its lower level, $3p^2\ ^3P_0$, while the others have two meta-stable levels as their lower levels, $3p^2\ ^3P_1$ and $3p^2\ ^3P_2$. Their upper levels are 3p 3d $^3P_1$, 3p 3d $^3P_0$, and 3p 3d $^3D_3$, respectively. In addition, we include a meta-stable level, $3p^2\ ^1D_2$, which has 10% of the ion's population. Fe XIII is plotted in the middle right panel of Figure 4.5.

Fe XIV has only one line we are interested in, 274.2 Å. This line has the ground level as its lower level, 3p $^2P_{1/2}$, and 3s $3p^2\ ^2S_{1/2}$ as its upper level. In addition to these levels we include the meta-stable level, 3p $^2P_{3/2}$, which has 46% of the ion's population. Fe XIV is plotted in the lower left panel of Figure 4.5.

Fe XV has only one line we are interested in, 284.2 Å. This line has the ground level as its lower level, $3s^2\ ^1S_0$, and 3s 3p $^1P_1$ as its upper level. This ion has no meta-stable levels in which a substantial fraction of these ions are in. Fe XV is plotted in the lower right panel of Figure 4.5.

4.2.3 Particular Changes

Two of the ions in the HAO-DIAPER package, Fe XIII and Fe XV, do not include the levels and lines we are interested in. We therefore take a look at the changes we have made to them below.

FE XIII

The 202.0 Å line is not included in the DIAPER file, but both the upper and lower levels are. We add this line with the oscillation strength from Aggarwal and Keenan (2004) and the collision strengths from CHIANTI.

The 203.2 Å line is listed with the wrong wavelength and further examinations show that the upper level is listed with wrong energy compared to CHIANTI. This is therefore changed from 503340 cm^{-1} to 501520 cm^{-1}.

FE XV

The 284.2 Å line is not included in the DIAPER file. When comparing the spectral notation with levels and lines in CHIANTI and NIST we find that the upper level is listed with wrong energy value and therefore the wavelength is wrong. We change the energy from 355439.156 cm^{-1} to 351911.000 cm^{-1}, and keep the rest of the parameters unchanged.

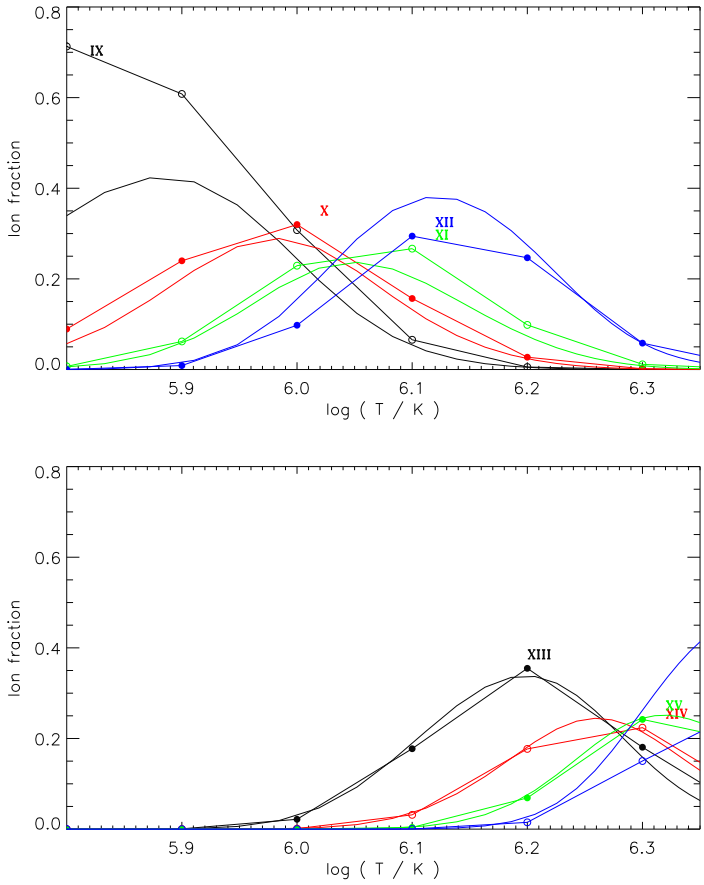

Figure 4.6: Ionization balance for iron. The lines with the dots are CHIANTI values using data from Mazzotta et al. (1998) and the lines with equal colors without dots are our values for the same ion. Top panel: Fe IX (black), Fe X (red), Fe XI (green), and Fe XII (blue). Bottom panel: Fe XIII (black), Fe XIV (red), Fe XV (green), and Fe XVI (blue).

4.2.4 Comparing the Ionization Balance

To get an impression of how good our model is we can look at the ionization balance, that is, the fraction of each ion to the total density of the element,

$$\frac{n(X^{+m})}{n(X)} \,. \tag{4.7}$$

Recall from Section 2.3 that the ionization and recombination rates are dependent on the electron temperature (and weakly dependent on the electron density), and therefore this fraction is also a function of temperature.

In Figure 4.6 we plotted the ionization equilibrium for our model (solid line), together with the ionization equilibrium from CHIANTI using data

from Mazzotta et al. (1998) (dotted line). The ions have the same color for both models. Note that there are much fever data points in the CHIANTI data, which makes the comparison more difficult.

Our Fe IX and Fe XVI ionic data do not agree with the CHIANTI data; the former gives a much lower ionization fraction, while the latter gives a much higher fraction. This disagreement is acceptable since we have no lines from these ions. On the other hand, the ions we are interested in, Fe X – Fe XV agree quite well with the CHIANTI data. Fe X, Fe XI and Fe XII show a bit too low ionization fraction at temperatures lower than 10^6 K, but are elsewhere in good agreement, assuming the CHIANTI data are missing the point of maximum fraction for the Fe XII ion. Fe XIII, Fe XIV and Fe XV are in good agreement, assuming the CHIANTI data are missing the point of maximum fraction for the Fe XIV and Fe XV ions.

4.3 Designing the Helium Model

Helium is the other atom we want to design to be able to examine the Hinode lines. The only helium line we are interested in is the He II 256.3 Å line. This is in reality two lines (256.317 Å and 256.318 Å), but the wavelength difference is so small that we consider them as only one line. This line is blended by the Si 256.4 Å line.

4.3.1 Included Ions and Levels

Helium has only three possible ionization stages, so for the ionization balance to be as correct as possible we include all of them.

Our atom file was originally made to study the 10840 Å line and includes nine energy levels. This file is made with the HAO-DIAPER package and uses excitation and ionization rates from Arnaud and Rothenflug (1985); Shull and van Steenberg (1982); Burgess (1965), and photoionization rates from Avrett et al. (1976). Instead of spending a lot of time examining which levels could be removed, we choose to keep these nine levels and only add the extra energy level and the transition rates for our line.

The information about the energy levels and rates for the combined 256.3 line are found from the HAO-DIAPER package. A Grotrian diagram[5] for our helium atom can be seen in Figure 4.7.

4.3.2 Comparing the Ionization Balance

As for hydrogen, we want to examine how good our model is. In Figure 4.8 we have plotted the ionization equilibria for our helium model (solid line) along with the ionization equilibrium from CHIANTI using data from

[5]The Grotrian diagrams are made with the HAO-DIAPER procedure 'termdiag.pro'.

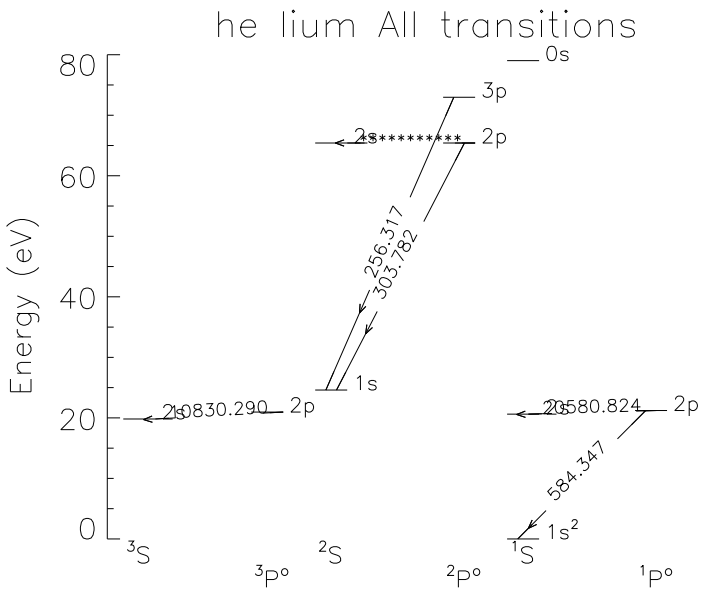

Figure 4.7: Grotrian diagram for the helium atom.

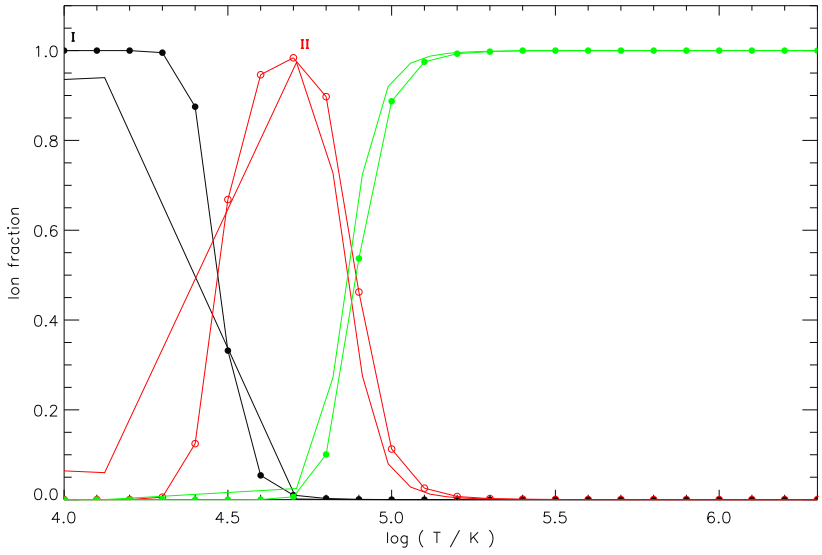

Figure 4.8: Ion balance for helium. He I (black), He II (red), and He III (green). The lines with the dots are CHIANTI values using data from Mazzotta et al. (1998) and the lines with equal colors without dots are our values for the same ion.

Mazzotta et al. (1998) (dotted line). As can be seen, the fit is generally quite good. At $T = 10^{4.9}$ K and warmer, where our helium line is formed, the fit is very good. Note that here it is our data which has less data points. This is because the adaptive grid allocates the grid points away from the almost isothermal chromosphere and towards the transition region where the temperature and density gradients are larger.

Chapter 5

Simulations

In this chapter we perform numerical simulations using the simulation code TTRANZ and our atomic model. First we give an introduction to our loop model and a short repetition of the heating mechanisms. Then we run three distinct experiments: an initially hot loop that cools, an initially cold loop that is rapidly heated, and a loop buffeted by acoustic waves from below. For each simulation we go through the morphological changes in the loop. Thereafter, we study how the different EIS spectral lines react to the event, and examine whether any of our lines are driven out of ionization equilibrium. Finally, we discuss which changes EIS is actually able to detect and whether these changes can give us information about the physical processes in the solar atmosphere.

5.1 The Loop Model

Loop Geometry and Boundary Conditions

The topology of the magnetic field in the solar atmosphere consists of loops with footpoints connecting different photospheric regions. When the magnetic field is strong (low β) the dynamics in the plasma are constrained to follow the magnetic field lines. Our loop model tries to resemble the plasma in one loop. z is defined as a 180° semi-circular flux tube of length 15 Mm and with no inclination relative to the vertical. The loop has footpoints in the middle chromosphere, stretching through the transition region and up into the almost isothermal corona. The area of the flux tube is kept constant, which should be acceptable for a low β coronal loop.

The footpoint boundaries are set up so that the temperature and pressure are driven towards 7000 K and 100 Pa, respectively, while at the same time varying in a manner that allows the propagation of sound waves out of the computational domain without reflection.

The Heating Mechanism

As described in Section 2.5 the internal energy, and thus the temperature, are defined by the conservation of energy equation (Equation 2.57),

$$\frac{\partial}{\partial t}(\rho e) + \frac{\partial}{\partial z}(\rho u e) + (p+Q)\frac{\partial u}{\partial z} = \frac{\partial}{\partial z}\left(F_c + F_r + F_h\right) .$$

Radiative losses ($\partial F_r/\partial z$) are determined by radiation mainly in the spectral lines of highly ionized elements such as carbon, oxygen, and iron, and in part by radiative recombination, and at temperatures higher than 1 MK, by bremsstrahlung. The conductive flux (F_c) is determined solely by the temperature profile, while the amplitude and scale height of the heating function (F_h) are set manually in the 'init' file (cf. Section 3.3.2). It is therefore the latter parameter we can adjust to make changes in the temperature distribution of our atmosphere. All our simulations are run with a heating function that exponentially decays with a scale height of 4 Mm, while the heating amplitude is varied according to the experiment being conducted. Equal amounts of energy are inserted into both footpoints. The sources and sinks in the energy equation are described in greater detail in Section 3.1.1.

In this work we are not interested in the nature of the heating, only the dynamic effects it has on the emission lines' intensities and Doppler shifts as detected by the EIS instrument. Our aims are to present a physically reasonable scenario and to pursue its consequences in the EIS spectral lines.

Before starting our simulations we let the system relax into a steady state, which is reached when the three sources and sinks are in balance,

$$\frac{\partial}{\partial z}\left(F_c + F_r + F_h\right) = 0 . \tag{5.1}$$

This is done to ensure that we are starting from an atmospheric state that is more or less in equilibrium, so that we can isolate the effects we are specifically studying here.

5.2 Warm Loop Cooling

An initially warm loop has been constructed and is shown in Figure 5.1. In the left panel we plot the logarithm of the temperature, pressure and electron density as functions of position along the loop (z). In the right panel we plot the plasma velocity as a function of z.

The temperature is of order 6000 K in the loop footpoints ($z = 0$ Mm and $z = 15$ Mm) extending almost 1 Mm up before the rapid transition region temperature rise is encountered. Here at $z \sim 0.6$ Mm the temperature rises to some 1.8 MK in a few Mm. This temperature structure is maintained by an input heat flux of 6000 W/m^2 in both sides of the loop, deposited from $z_0^{left} = 4.5$ Mm and $z_0^{right} = 10.5$ Mm, with a scale height $z_H^{left} = z_H^{right} =$

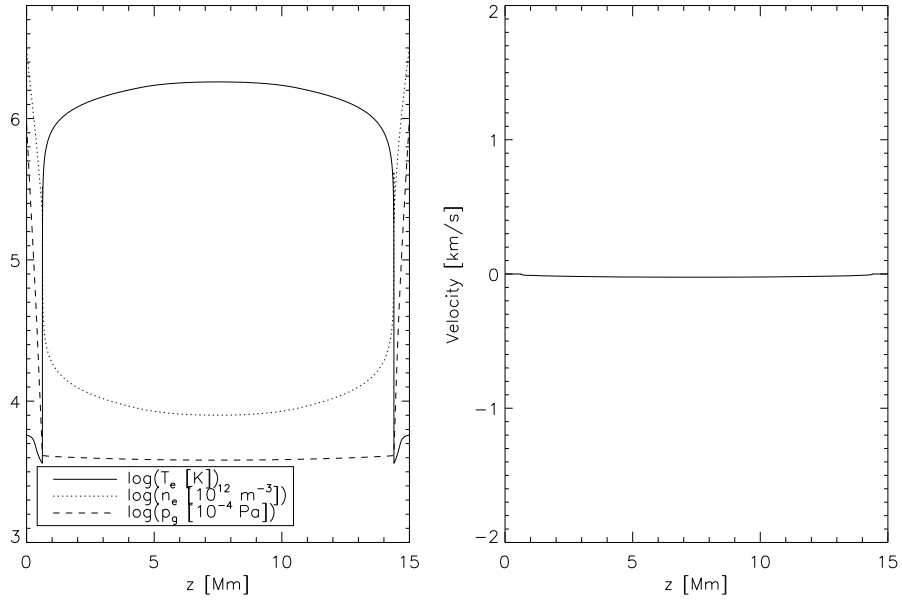

Figure 5.1: Left panel: The initial distribution of temperature (solid), pressure (dashed) and electron density (dotted) with distance (z) along loop. Right panel: The initial velocity distribution with distance (z) along loop.

4.0 Mm. See Figure 3.1. The electron density starts out at 3×10^{18} m^{-3} in the footpoints, decreasing to 2×10^{17} m^{-3} in the upper part of the chromosphere. In the transition region the density drops of even more, and continues to decrease down to 10^{16} m^{-3} in the corona.

The pressure starts of at 100 Pa in the footpoints, decreasing rapidly with a scale height[1] of some 100 km in the chromosphere, to about 0.5 Pa at the bottom of the transition region. As the temperature rises the pressure scale height increases and the pressure is almost constant through the upper part of the loop. As seen in the right panel of Figure 5.1, the velocity is nearly zero through the entire initial model.

At time $t = 0$ s the heating amplitude is reduced to 60 W/m^2, and kept at that value throughout the simulation. No other changes are made.

5.2.1 Loop Changes

We will describe the morphology of the loop plasma in terms of the thermodynamical variables temperature, velocity, and density, and describe the changes caused by the abrupt reduction in heat deposition. Have in mind that these are actually changes in the loop morphology, and not necessarily

[1]The pressure scale height is given by $H_p = \frac{k_B T}{\overline{m} g}$, where $g = \frac{GM_r}{r^2}$ is the local acceleration of gravity.

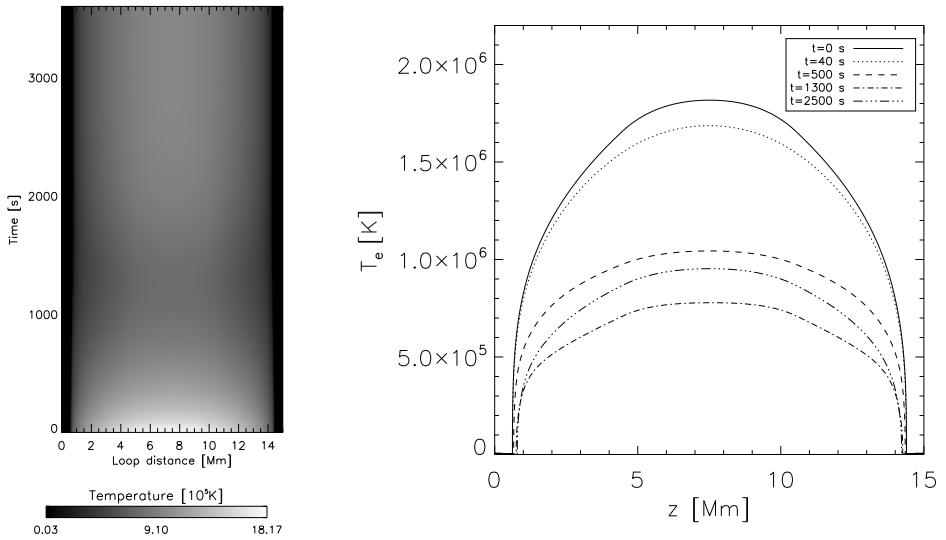

Figure 5.2: Temperature variations in the cooling loop. Left panel: Temporal evolution of the temperature along the loop. Right panel: A time series of footpoint to footpoint temperature profiles as a function of the distance (z) along the loop taken at $t = 0$ s (solid), $t = 40$ s (dotted), $t = 500$ s (dashed), $t = 1300$ s (dash-dotted), and $t = 2500$ s (dash-dot-dot-dotted).

changes that would be detected by the EIS instrument. We will come back to the detectable changes, that is, the line intensity and Doppler velocity in Section 5.2.2, and discuss which changes EIS is actually able to detect in Section 5.2.4.

Temperature

When the heat flux is reduced, the loop cools. The evolution of the loop temperature is shown in Figure 5.2 for the first hour after the heat flux is reduced. Initially, the apex temperature falls some 0.1 MK, to less than 1.7 MK, during the first 40 seconds. The decrease is most rapid in the hottest upper part of the loop, presumably due to the temperature sensitivity of the conductive flux (Equation 3.2) which is the main energy loss mechanism in the loop corona.

The loop continues to cool rapidly, falling some additional 0.7 MK to 1 MK in the next 460 s. After this time the temperature decrease is somewhat slower and the lowest loop temperatures are found 1300 s after the heat flux was reduced. At this time the loop apex has a temperature of 0.7 MK. In the period $t = 1300$ s to $t = 2500$ s the loop apex temperature rises slowly to some 0.9 MK at which time the temperature structure becomes static.

While the temperature of the upper, coronal part of the loop changes

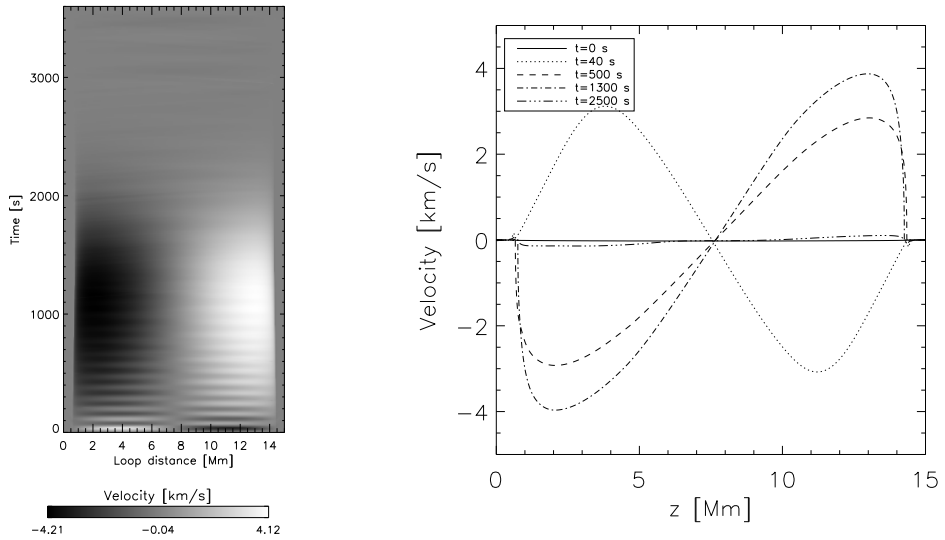

Figure 5.3: Velocity variations in the cooling loop. Left panel: Temporal evolution of the velocity along the loop. Right panel: A time series of footpoint to footpoint velocity profiles as a function of the distance (z) along the loop. The curves are labeled in the same manner as in Figure 5.2.

rapidly, only small changes can bee seen in the loop footpoints. The upper part of the chromosphere cools slightly, and the bottom of the transition region moves upward some 0.2 Mm.

Velocity

The abrupt reduction in heat flux also has an effect on the plasma velocity in the loop. There are no movements in the plasma at the onset of the simulation, but after $t = 0$ s velocities start propagating along the loop, as can be seen in Figure 5.3. The left panel of this figure shows a wave pattern in the first 1000 s, fading out as time passes. From $t = 500$ s to $t = 2000$ s there are plasma moving away from the loop apex and down into both footpoints. After some 2500 s there are almost no movements left in the loop.

The preferential rapid cooling of the loop apex causes a pressure drop which generates a sound wave propagating towards the loop apex. The sound speed is given by

$$u_s = \sqrt{\frac{\gamma\, p_g}{\rho}}\,. \tag{5.2}$$

In our loop the coronal pressure is ~ 0.5 Pa and the density is $\sim 10^{-11}$ kg/m^3, which yield a sound speed of some 100 km/s, assuming the ratio of specific

heats to be $\gamma = 5/3$. From the left panel of Figure 5.3 the sound wave period is estimated to be 100 s, giving a wavelength of some 10 Mm. This wavelength is much larger than the temperature scale height in the transition region and the wave is reflected due the rapid change in sound speed. Thus, the wave is trapped in the corona, and is bouncing back and forth between the two footpoints. It is this standing wave which is visible in the left panel of Figure 5.3 during the first 1000 s of our simulation. The amplitude of the wave is initially some 3 km/s, which can be seen at $t = 40$ s (dotted line) in the right panel of the figure. The velocity drops steadily as the wave is damped, presumably due to leakage into the transition region or by radiative damping. The amplitudes in the lower parts of the loop decrease fastest because of the higher density.

The changes in temperature described above have consequences for the pressure balance in the loop. The loop is being supported by the pressure gradient, and when the temperature changes, so does the pressure, according to Equation 2.55,

$$p = \frac{\rho k_B T}{\overline{m}} \, .$$

As the plasma cools it loses hydrostatic support, causing the material to drain out of the loop. First, as noted above, the temperature and thus the pressure near the top of the loop falls very rapidly, causing a short lived upflow towards the loop apex. As the loop continues to cool, the flow is being moved downwards with an increasing velocity, reaching a 4 km/s maximum some 1300 s after the simulation begins. As the loop re-heats, the flow slows and the velocity is nearly zero after 2500 s.

Density

As seen in Figure 5.4 the density is almost unchanged during the first 500 s after the onset of our simulation. However, after this time and until $t = 1300$ s the density at the loop apex is reduced by a factor three as material drains out of the loop, from $\log(\rho) = -10.8$ to $\log(\rho) = -11.2$. After this time the density continues to decrease, though more slowly, and first stabilizes after 2500 s at $\log(\rho) = -11.4$. While the fall of density in the corona is dramatic, only small changes are seen in the density structure of the transition region and none is seen in the chromosphere.

The measured drop in density can explain the temperature increase in the latter stages of our simulation after $t = 1300$ s. The energy input is constant throughout the simulation, and a reduction in density causes fewer particles to share this energy input. As a result the temperature will rise slightly as the density drops.

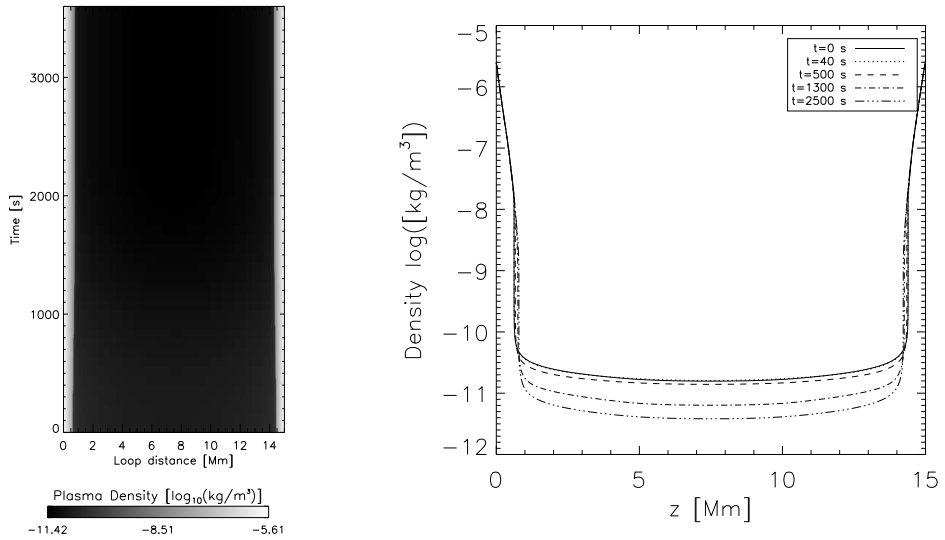

Figure 5.4: Density variations in the cooling loop. Left panel: Temporal evolution of the density along the loop. Right panel: A time series of footpoint to footpoint density profiles as a function of the distance (z) along the loop. The curves are labeled in the same manner as in Figure 5.2.

5.2.2 The EIS Lines' Response to the Changes

Let us now see how the EIS spectral lines are affected with the changes in loop temperature, density and velocity as described above. The lines' intensity and velocity are calculated according to the line momentum analysis described in Section 2.4.2.

In order to cover a large span in temperature we choose to study in detail six iron lines, one from each of the ions Fe X to Fe XV, as well as one He II line. The lines' wavelengths and temperatures of peak abundance are listed in Table 5.1.

Intensity

Changes in intensity as a function of time are shown in Figure 5.5. The intensity of the three iron lines with the lowest temperatures of peak abundance, Fe X 184.5 Å, Fe XI 188.2 Å, and Fe XII 195.1 Å, are plotted with solid, dotted, and dashed lines, respectively. These lines' intensity increases slightly during the first few hundred seconds of the simulation. After this time, their intensities fall dramatically until $t \approx 1300$ s. The coolest line (184.5) drops off by a factor ten from its initial value, while the warmest line (195.1) decreases by three orders of magnitude. After $t \approx 1300$ s, as the loop re-heats the decrease of intensity is halted, and the intensity increases.

Wavelength [Å]	Ion	Temperature $\log(T[K])$
184.5	Fe X	6.00
188.2	Fe XI	6.08
195.1	Fe XII	6.13
202.0	Fe XIII	6.20
274.2	Fe XIV	6.28
284.2	Fe XV	6.32
256.3	He II	4.92

Table 5.1: Temperature of peak abundance for the examined EIS lines.

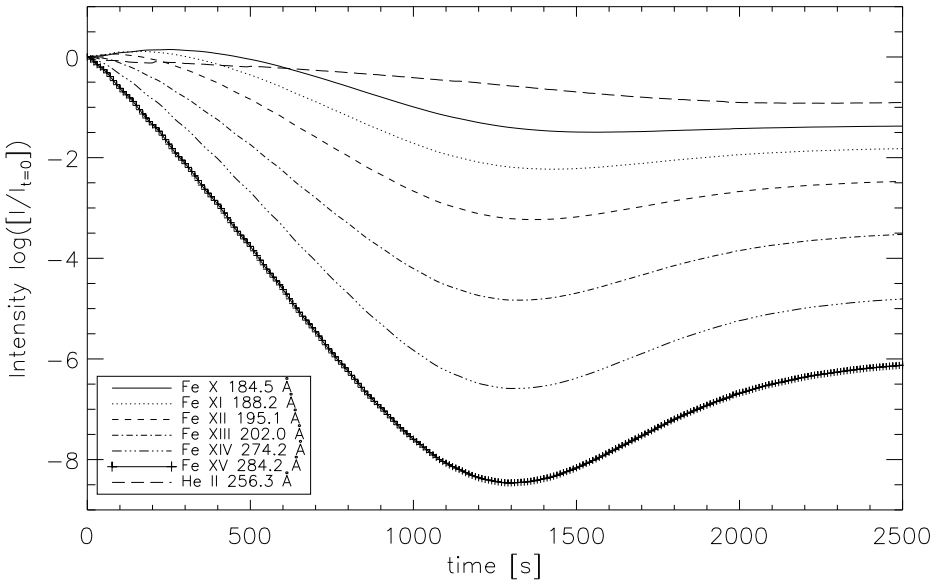

Figure 5.5: Intensity variations for the EIS spectral lines Fe X 184.5 Å (solid), Fe XI 188.2 Å (dotted), Fe XII 195.1 Å (dashed), Fe XIII 202.0 Å (dash-dotted), Fe XIV 174.2 Å (dash-dot-dot-dotted), Fe XV 284.2 Å (plus), and He II 256.3 Å (long dashes) as a function of time. The intensities have been normalized to be one at $t = 0$ s.

When the loop has stabilized after 2500 s, the intensity of the first line has been reduced by a factor 30 compared to its level at the onset of the simulation, the second has fallen by two orders of magnitude, and the third by three orders of magnitude.

The three hotter iron lines Fe XIII 202.0 Å, Fe XIV 274.2 Å, and Fe XV 284.2 Å are also plotted in Figure 5.5. These lines start decreasing in intensity immediately, with the ion of highest temperature of peak abundance falling very rapidly indeed. All these lines have a minimum after about 1300 s, when the coolest (202.0) has been reduced by five orders of magnitude while the warmest (284.2) has been reduced by nine orders of magnitude. When the loop has stabilized after 2500 s, the 202.0 line has fallen by four orders of magnitude compared to the onset of the simulation, the 274.2 line is reduced by five orders of magnitude, and the 284.2 line by six orders of magnitude.

In contrast, the He II 256.3 Å, which is formed in the lower transition region, shows fairly small variations in intensity. This line is plotted with long dashes in Figure 5.5. The intensity of this line falls less than a factor ten, and it has no distinct minimum at $t \approx 1300$ s when the loop is at its minimum temperature.

Let us now try to explain why these lines' intensity changes as it does. The intensity is related to the number density in the upper level that contributes in the line formation (n_u) as stated in Equation 2.2,

$$I_\nu = \frac{h\nu}{4\pi} \int_0^s n_u A_{ul}\, \phi_\nu \, ds \,.$$

When coronal equilibrium is valid, n_u should relate to the temperature and density as (cf. Equation 2.12)

$$n_u = n_l n_e \frac{C_{lu}}{A_{ul}} \propto \rho^2 f(T) \,. \tag{5.3}$$

We will now try to explain the variations in n_u by the changes in temperature and density, and examine whether these variations relate to the changes in the lines' intensity.

The number density of the upper level of the three iron lines which start by increasing in intensity the first few hundred seconds, Fe X 184.5 Å, Fe XI 188.2 Å, and Fe XII 195.1 Å, are plotted in the upper left, upper right, and middle left panels of Figure 5.6, respectively. At time $t = 0$ s these lines are mostly formed in the transition region and lower corona. After 40 s, the number density in each of the upper levels has barely decreased in these regions while it has increased substantially in the corona, where the temperature is falling rapidly. In total n_u for these lines has increased (or at least not decreased), resulting in a stronger emission from these lines.

The temperature keeps falling, and is reduced to 1 MK after 500 s. In the mean time, the number density population has continued to fall of in

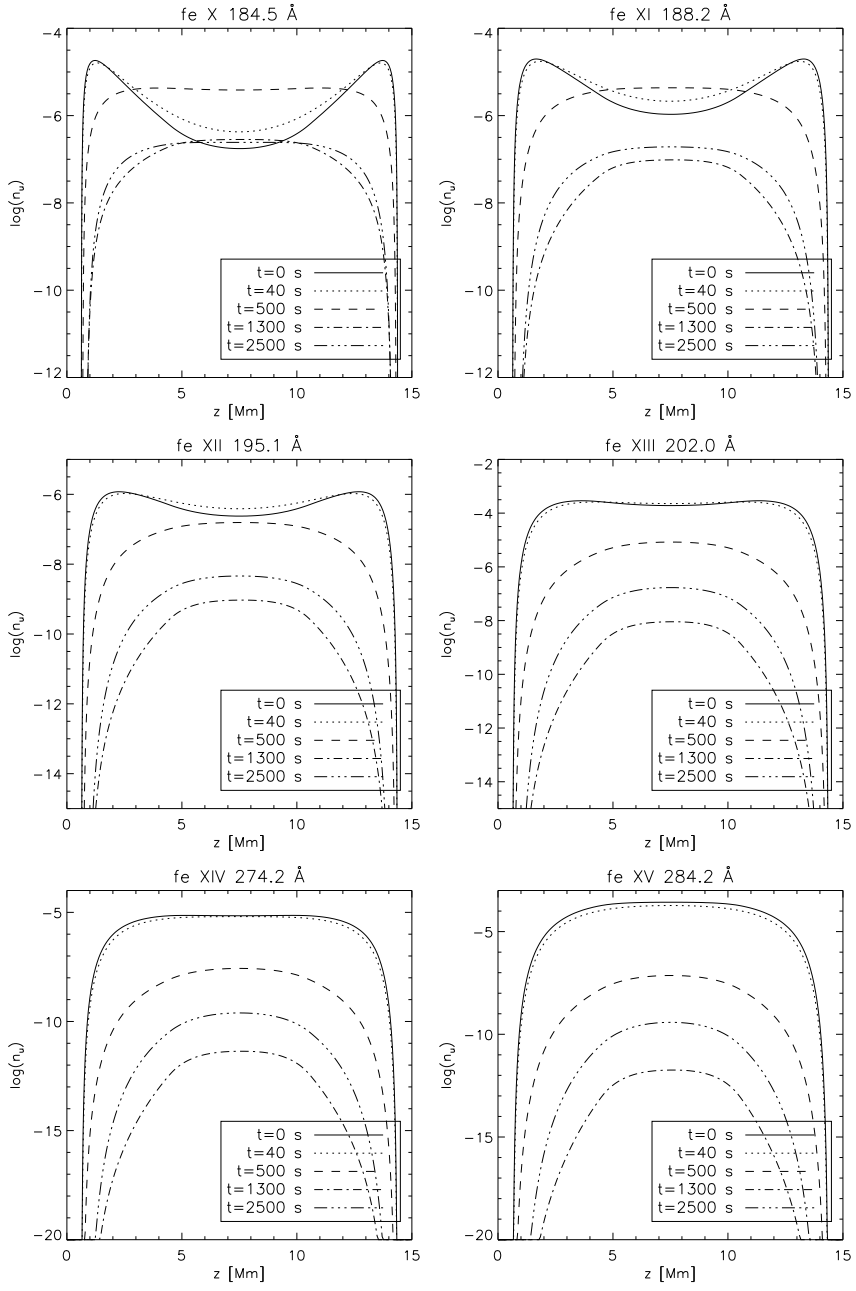

Figure 5.6: Variations in the number density of the upper level (n_u) for the EIS spectral lines Fe X 184.5 Å (upper left panel), Fe XI 188.2 Å (upper right panel), Fe XII 195.1 Å (middle left panel), Fe XIII 202.0 Å (middle right panel), Fe XIV 174.2 Å (lower left panel), and Fe XV 284.2 Å (lower right panel) as a function of the loop distance (z) plotted for different times. The curves are labeled in the same manner as in Figure 5.2.

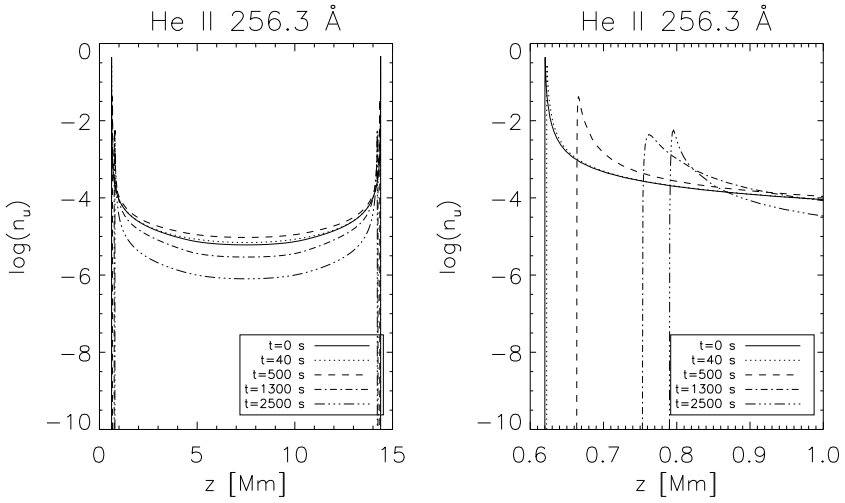

Figure 5.7: Variations in the number density of the upper level (n_u) for the EIS spectral line He II 256.3 Å as a function of the loop length (z). The left panel shows the whole loop, while the right panel only shows the left transition region. The curves are labeled in the same manner as in Figure 5.2.

the transition region and increased in the corona. Now n_u is greatest in the loop apex. This transfer in line formation region, in addition to the small reduction in density so far, yield that the total n_u has not decreased substantially. After $t = 500$ s, there are no places in the loop warm enough for these ions to be formed in sufficient numbers, as the apex temperature is lower than the ions temperature of peak abundance. In addition, the density (ρ) in the upper parts of the loop starts decreasing. Therefore, the number population of the upper level of these ions falls of, and n_u reaches a minimum after 1300 s as the temperature reaches its minimum value. From $t = 1300$ s to $t = 2500$ s n_u increases slightly in all parts of the loop as a result of the rise in temperature, and despite the continuing reduction in density.

After 2500 s, n_u for the 184.5 line is reduced by almost a factor 30, the 188.2 lines is reduced by almost a factor 100, while n_u for the 195.1 line is reduced by a factor 3000. This is exactly the same difference as we found for the intensity for these lines.

The number density of the upper level of the three hotter iron lines, Fe XIII 202.0 Å, Fe XIV 274.2 Å, and Fe XV 284.2 Å, are plotted in the middle right, lower left, and lower right panels of Figure 5.6, respectively. These lines are mostly formed in the upper parts of the loop at the onset of the simulation ($t = 0$ s), and as the temperature falls there are no warmer places where the population can increase, as it was for the lines formed at lower temperatures. Therefore, the total n_u for these lines is reduced immediately, and so is the intensity. As the temperature continues to drop

off and the density is reduced substantially in the upper parts of the loop, n_u continues to decrease. This causes the intensity to fall of by a large number of magnitudes and the lines to essentially disappear.

The number density of the upper level of the transition region He II 256.3 Å line is plotted in Figure 5.7. This line is mostly formed in the transition region, but also partly in the corona. Therefore, we plot n_u for different times as a function of the loop distance in the left panel, while in the right panel we focus on the left footpoint transition region only. As the loop cools, its apex never reaches the temperature of peak abundance for the helium line at $10^{4.9}$ K. Therefore, the reduction in temperature does not effect the n_u-population as much as for the iron lines. This causes the intensity to decrease as the density goes down, but in much less degree than the iron lines. After 2500 s, n_u for this line has been reduced by almost a factor ten, which is the same as the reduction in intensity. The moving transition region is clearly visible in the right panel of Figure 5.7.

Doppler Velocity

The Doppler velocity for the lines discussed above is plotted in Figure 5.8. Each line shows a sum of the two velocity signals, that is, the sound wave with period of 100 s and on longer time-scales the mass flow from the apex and down into the footpoints.

The velocity is different for the different lines, with the iron ions with lowest temperature of peak abundance having the greatest negative velocities the first 500 s, and after this the helium line has greatest negative velocity. The maximum velocity of the plasma movement along the loop was found in the previous section to be after 1300 s, which is almost the same time as the maximum Doppler velocity measured by the helium line. The iron lines on the other hand, do not show an exact minimum but have their greatest negative velocity from 400 to 700 s after the onset of the simulation. The reason for this is that in the beginning of the simulation, the plasma velocity is greatest in the corona, where the iron lines are formed. As time passes the region of the maximum velocity is moving down into the lower corona and transition region, where the helium line is formed. This can be seen in the right panel of Figure 5.3. Therefore, the velocity of this line is rising (negatively) as long as the loop velocity is increasing. The iron lines, on the other hand, stop increasing as the plasma velocity peak passes the region of their peak abundance. In addition, the lines with lowest temperature of peak abundance are formed more in the lower regions of the loop, where the velocities contribute more to the line of sight velocity.

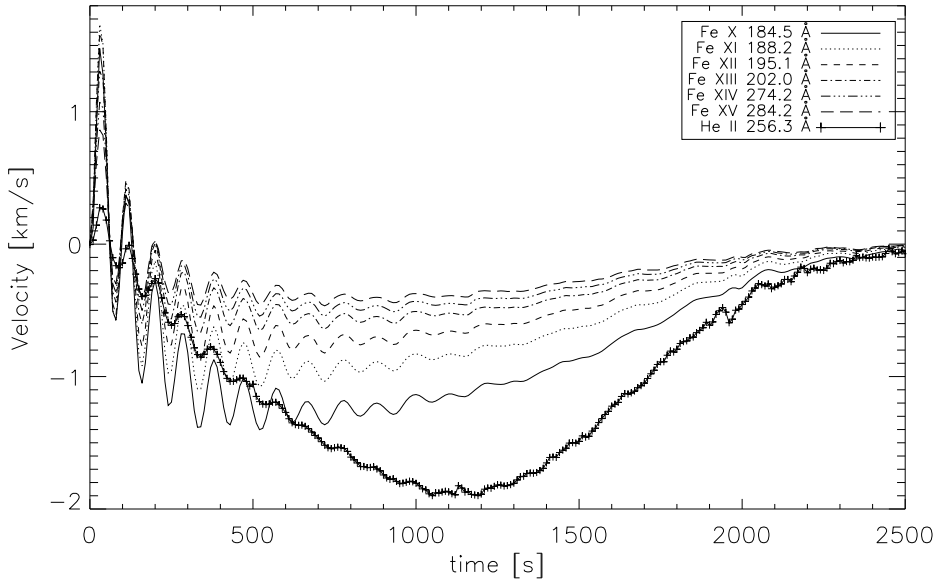

Figure 5.8: Doppler velocity variations for the EIS spectral lines Fe X 184.5 Å (solid), Fe XI 188.2 Å (dotted), Fe XII 195.1 Å (dashed), Fe XIII 202.0 Å (dash-dotted), Fe XIV 174.2 Å (dash-dot-dot-dotted), Fe XV 284.2 Å (long dashes), and He II 256.3 Å (plus) as a function of time. Velocities are defined as positive towards a detector situated vertically above the loop apex.

The amplitude of the sound wave pattern is also different for the different lines. There are not many differences between the iron lines, but the helium line has clearly smaller amplitudes. This comes from the fact that the helium line is formed in the transition region, where the density is much higher than in the corona.

5.2.3 Ionization Equilibrium

We want to examine whether any of our lines go out of equilibrium during the simulation. This is done by looking at how the fraction of the number density of the upper level of the line to the total density of the element is, compared to the contribution function.

In ionization equilibrium it is assumed that the ion populations respond instantaneously to changes in the plasma temperature (and density), e.g. for iron according to Figure 4.6. However, if there is a rapid change in temperature, such as in this simulation, then we could have cases where this assumption might not be valid. For instance, this might result in ions of high charge state existing at much lower temperatures than they would if they where in ionization equilibrium. Emission lines can be driven out of equilibrium by mass flows through temperature gradients. In this case, the

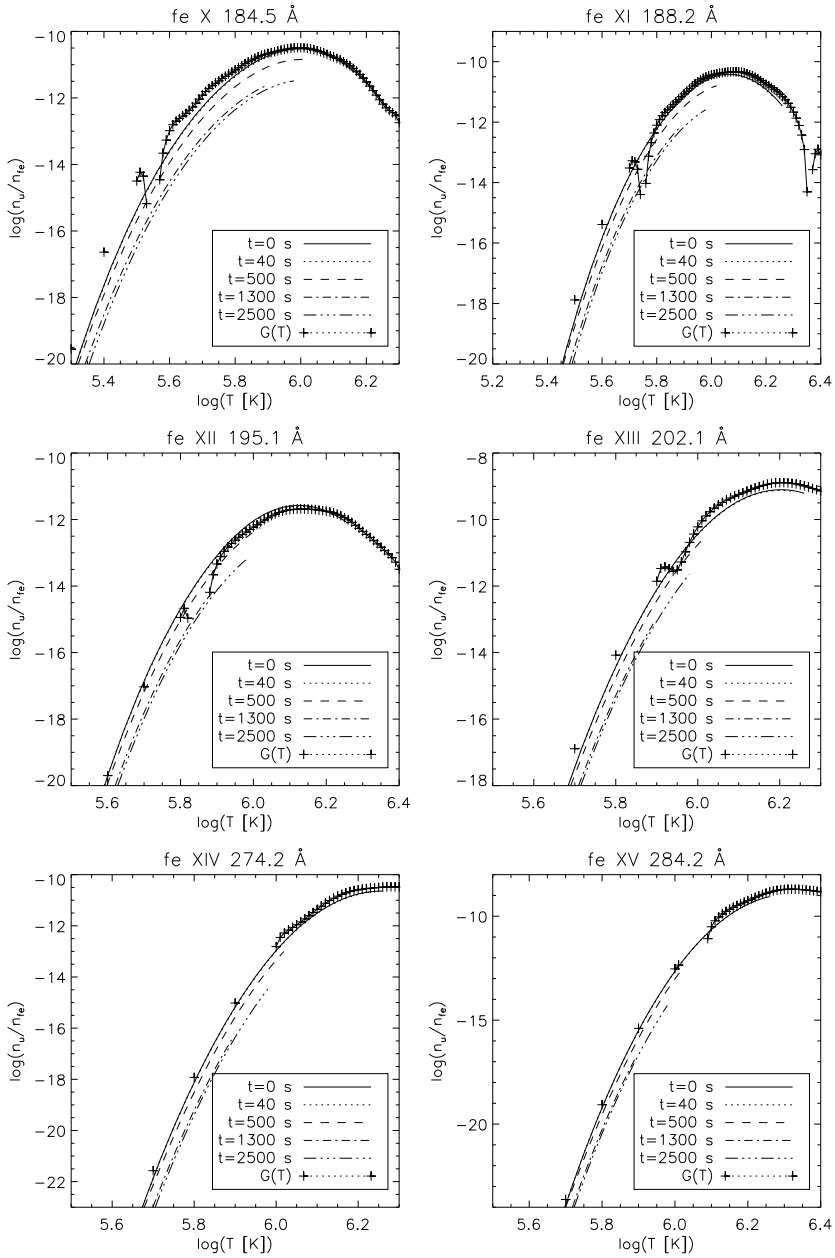

Figure 5.9: Variations in the ratio of the number density of the upper level (n_u) to the total number density of iron ($n_{\rm fe}$) for the EIS spectral lines as a function of temperature and for different times. Fe X 184.5 Å (upper left panel), Fe XI 188.2 Å (upper right panel), Fe XII 195.1 Å (middle left panel), Fe XIII 202.0 Å (middle right panel), Fe XIV 174.2 Å (lower left panel), and Fe XV 284.2 Å (lower right panel). The curves are labeled in the same manner as in Figure 5.2. All panels are over-plotted by the contribution function of the line (plus) in arbitrary units.

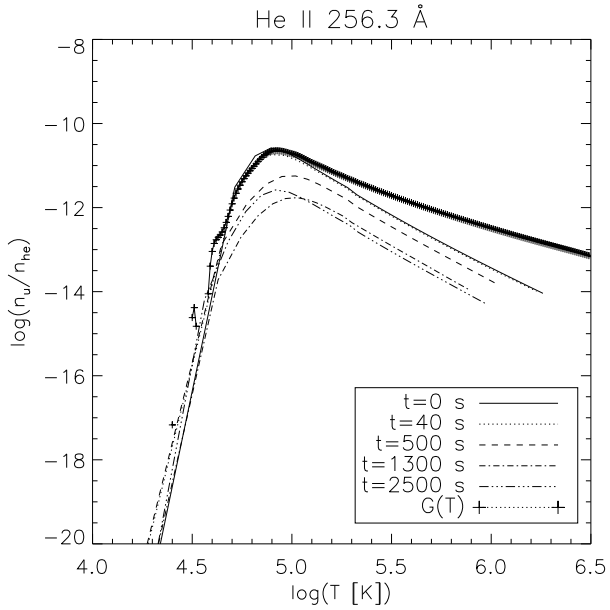

Figure 5.10: Variations in the ratio of the number density of the upper level (n_u) for He II 256.3 Å to the total number density of helium ($n_{\rm he}$) as a function of temperature and for different times, over-plotted by the contribution function of the line (plus) in arbitrary units. The curves are labeled in the same manner as in Figure 5.2.

ions might be transported into regions with temperatures different from their temperature of peak abundance before they have time to recombine or ionize (Joselyn et al., 1979). In low density plasma the characteristic time-scale of an ionic population can be many minutes.

It is important to know whether the lines go out of equilibrium if one want to use the lines to do temperature or density diagnostics. In addition, one should pay attention to the ionization equilibrium when using the assumption $I \propto n_e n_H G(T)$, since the lines can have non-zero contribution also where the contribution function is zero.

The fraction of the number density population of the upper level to the total element number density is plotted for the iron lines in Figure 5.9 and for the helium line in Figure 5.10. In the same figures we have also plotted the contribution functions for the lines to examine whether the populations have moved out of equilibrium during the simulation.

At $t = 0$ s, all our lines are in ionization equilibrium; this is expected since the loop was relaxed into a steady state before the onset of the simulation. Despite the rapid changes in the temperature and the subsequent mass flows in the beginning of this simulation, none of our iron lines go notably out of equilibrium. The helium line does not go far out of equilibrium, but it might seem like the temperature of peak abundance at $t = 500$ s and $t = 1300$ s are

a bit higher than they should be in ionization equilibrium. At $t = 2500$ s, the loop has settled and the line is brought back to equilibrium.

The helium line is more easily brought out of equilibrium since it is formed in the transition region where the temperature scale height is much shorter than in the corona. In this region only small plasma velocities are needed to move the ions away from their equilibrium.

5.2.4 Interim Conclusion

We have in the previous sections discussed the real changes in temperature, velocity and density in our loop, as a consequence of the abrupt reduction of heat input at time $t = 0$ s, and how these changes would affect some of the EIS spectral lines. EIS has limitations in its spectral resolution, so all the changes we have seen here might not actually be detected by the spectrograph. When choosing which lines to study in Chapter 4, we set the requirements to lines for which it is possible to resolve velocities of 5 km/s with 60 s exposure time.

The sound wave periods detected in this simulation are in the order of 100 s, with only the first period having amplitudes greater than 1.5 km/s (see Figure 5.8). This would unlikely be resolved by EIS. The greatest Doppler velocity amplitude is the one of the He 256.3 Å line of 2 km/s which is also probably a bit too small to be detected, but since the flow lasts for more than 500 seconds the cooling loop flow may be marginally detectable.

Even so, the EIS spectrograph is still not useless for detecting this kind of event. The enormous reduction in intensity, e.g. the Fe XV 284.2 Å decreasing with nine orders of magnitude, would definitely be detected, and give a hint that the heating rate and thus the temperature has been reduced. Not all of the lines react as violently to the changes though, e.g. He II 256.3 Å which falls by almost a factor ten, and Fe X 184.5 Å which is reduced by almost a factor thirty.

We have also seen that none of our iron lines go far out of equilibrium during this simulation, so we can relatively safely use these lines for temperature and density diagnostics. We can also assume that $I \propto n_e n_H G(T)$ is a good model for the iron line formation for a cooling loop. With the helium line on the other hand, more care must be taken, since this line might be brought out of equilibrium by the cooling event that defines this simulation.

5.3 Cold Loop Heating

The starting point of this simulation is the cool loop that resulted from the simulation described in Section 5.2, that is, $t = 3600$ s is now set to $t = 0$ s. The initial temperature, pressure, electron density, and velocity as functions of position along the loop can be seen in Figure 5.11.

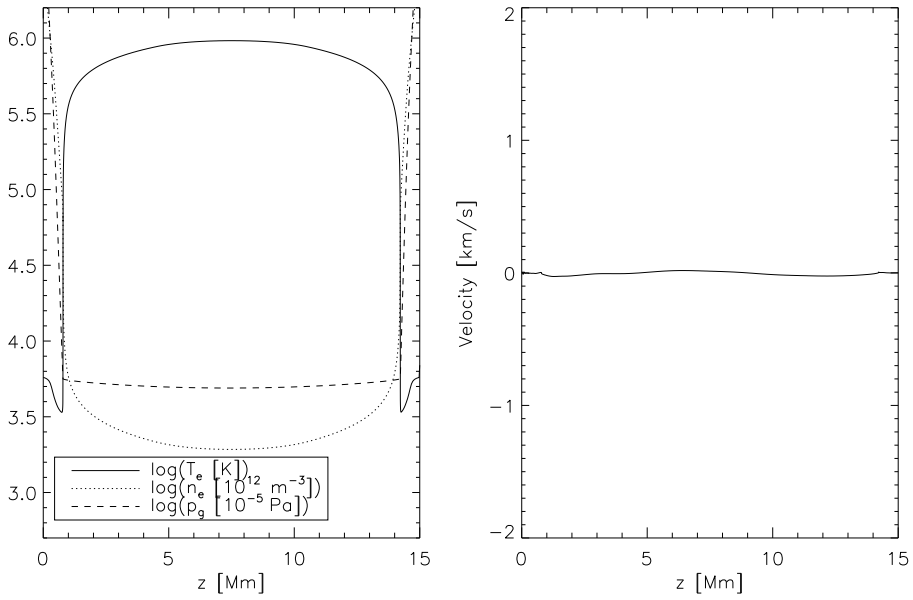

Figure 5.11: Left panel: The initial distribution of temperature (solid), pressure (dashed) and electron density (dotted) with distance (z) along loop. Right panel: The initial velocity distribution with distance (z) along loop.

The temperature is of order 6000 K in the loop footpoints extending almost 1 Mm up before the rapid transition region temperature rise is encountered. Here, at $z \approx 0.8$ Mm, the temperature rises to almost 1 MK over a few Mm. This temperature structure is maintained by an input heat flux of 60 W/m^2 in both sides of the loop, deposited from $z_0^{left} = 4.5$ Mm and $z_0^{right} = 10.5$ Mm, with a scale height $z_H^{left} = z_H^{right} = 4.0$ Mm. The electron density starts out at 3×10^{18} m^{-3} in the footpoints, decreasing to 2×10^{17} m^{-3} in the upper part of the chromosphere. In the transition region the density drops of even more, and continues to decrease down to 10^{15} m^{-3} in the corona.

The pressure starts of at 100 Pa in the footpoints, decreasing rapidly to less than 0.05 Pa, until the end of the transition region. As the temperature rises, the pressure scale height increases, and the pressure is almost constant through the upper part of the loop. As seen in the right panel of Figure 5.11, the velocity is nearly zero through the entire initial model. At $t = 0$ s we change the heating flux back to what it was before the cooling started in the previous section, namely 6000 W/m^2, and start our new experiment. No other changes are made.

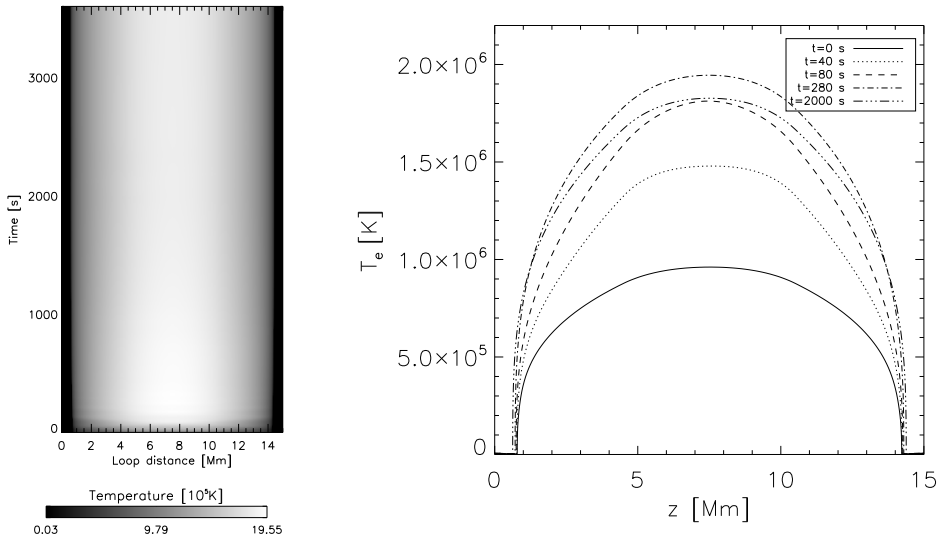

Figure 5.12: Temperature variations in the heating loop. Left panel: Temporal evolution of the temperature along the loop. Right panel: A time series of footpoint to footpoint temperature profiles as a function of the distance (z) along the loop taken at $t = 0$ s (solid), $t = 40$ s (dotted), $t = 80$ s (dashed), $t = 280$ s (dash-dotted), and $t = 2000$ s (dash-dot-dot-dotted).

5.3.1 Loop Changes

As in the Section 5.2.1 we first describe the morphology of the loop plasma in terms of the thermo-dynamical variables temperature, velocity, and density, and study the changes caused by the abrupt rise in heat deposition.

Temperature

When we increase the heat flux, the loop heats. The evolution of the loop temperature is shown in Figure 5.12 for the first hour after the heat flux is increased. Initially, the loop heats rapidly with the apex temperature rising some 0.5 MK during the first 40 seconds, and some additional 0.3 MK over the next 40 s. The heat flux is added in the upper parts of the loop, so this is where the loop temperature rises first, but since conduction is effective in transporting heat, the other parts of the upper loop soon follow. The temperature continues to increase another 200 s, but much more slowly, and the loop apex has a maximum temperature of almost 2 MK at $t = 280$ s. Then the loop cools slightly to some 1.8 MK, at which the temperature is stable after some 2000 s.

While the temperature of the upper, coronal part of the loop changes rapidly, only small changes can bee seen in the footpoints. The upper part

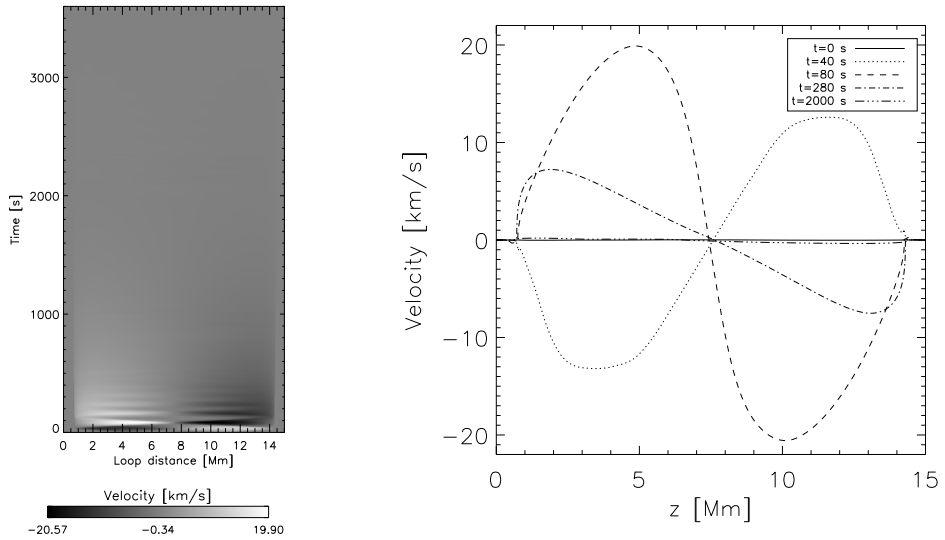

Figure 5.13: Velocity variations in the heating loop. Left panel: Temporal evolution of the velocity along the loop. Right panel: A time series of footpoint to footpoint velocity profiles as a function of the distance (z) along the loop. The curves are labeled in the same manner as in Figure 5.12.

of the chromosphere heats up slightly, moving the bottom of the transition region downwards some 0.2 Mm.

Velocity

Also in this experiment does the change in heat input affect the velocities in the plasma, and this time more violently and on shorter time-scales than in the previous experiment. The loop velocities for the first hour of the simulation can be seen in Figure 5.13. The left panel of this figure shows a wave pattern the first 300 s, and a mass flux from the footpoints towards the apex during the first 1500–2000 s.

The rapidly increasing temperature in the loop apex causes an increased pressure which creates a sound wave propagating from the loop apex and down towards the footpoints. With a pressure of ~ 0.05 Pa and density of $\sim 10^{-12}$ kg/m^3 we get a sound velocity of some 100 km/s. As in the previous experiment the wave is being reflected when it reaches the transition region due to the rapid change in sound speed. The wave amplitude reaches its maximum of 20 km/s after 80 s, and thereafter it is being quickly damped. The left panel of Figure 5.13 shows only three oscillations, with a period of about 100 s. As in the previous experiment the wave is damped presumably due to leakage into the transition region or by radiative damping. The oscillations disappear in the lower parts of the loop first, because of the

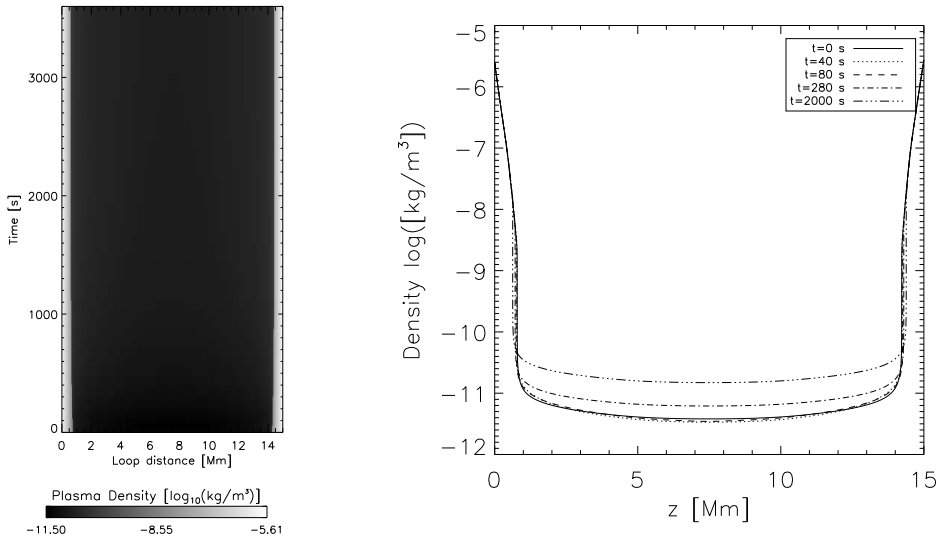

Figure 5.14: Density variations in the heating loop. Left panel: Temporal evolution of the density along the loop. Right panel: A time series of footpoint to footpoint density profiles as a function of the distance (z) along the loop. The curves are labeled in the same manner as in Figure 5.12.

higher density. As noted above, the plasma is first moving downwards, but as the loop heats it is able to support more mass, causing the material to flow upwards. This mass flux lasts some 2000 s, with continuously decreasing velocity.

Density

As can be seen in Figure 5.14, the density is almost constant the first 80 seconds, except for a small decrease around the loop apex and increase in the lower part of the corona. From 80 s the density is increasing through all of the upper parts of the loop, with the apex value increasing with a factor four, from $\log(\rho) = -11.4$ at $t = 0$ s to $\log(\rho) = -10.8$ at $t = 3600$ s. As in the previous experiment, only small changes are seen in the density structure of the transition region and none is seen in the chromosphere.

The increased density causes the loop heating to stabilize and the loop cools slightly after 280 s. This is the opposite effect of what was seen in the previous experiment.

5.3.2 The EIS Lines' Response to the Changes

Now we take a look at what happen to the EIS spectral lines as a result of the loop changes in temperature, density, and velocity as described above. The

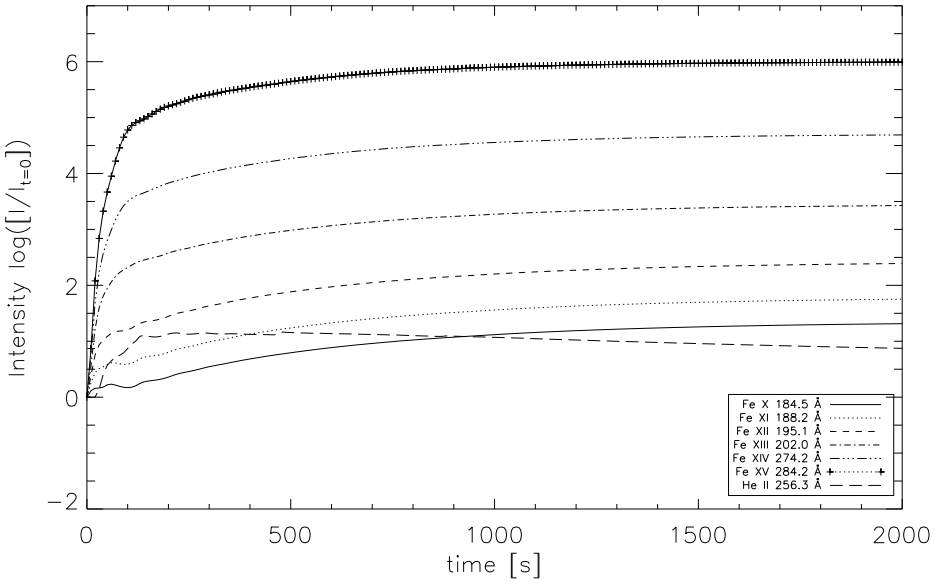

Figure 5.15: Intensity variations for the EIS spectral lines Fe X 184.5 Å (solid), Fe XI 188.2 Å (dotted), Fe XII 195.1 Å (dashed), Fe XIII 202.0 Å (dash-dotted), Fe XIV 174.2 Å (dash-dot-dot-dotted), Fe XV 284.2 Å (plus), and He II 256.3 Å (long dashes) as a function of time. The intensities have been normalized to be one at $t = 0$ s.

lines' intensity and velocity are calculated according to the line momentum analysis described in Section 2.4.2.

We discuss the same lines as in the previous simulation. Their wavelength and temperature of peak abundance are listed in Table 5.1.

Intensity

The four hottest iron lines, Fe XII 195.1 Å, Fe XIII 202.0 Å, Fe XIV 274.2 Å, and Fe XV 284.2 Å, show a rapid intensity rise the first few hundred seconds after the heat flux is increased. Changes in intensity as a function of time is shown in Figure 5.15. The lines with the highest temperature of peak abundance are increasing the most, with 284.2 increasing by five orders of magnitude in 100 s. The two coldest iron lines (Fe X 184.5 Å and Fe XI 188.2 Å) do not share that rapid increase, but rather more varying intensity, before they start rising. After the first few hundred seconds the iron lines' intensity out-level, and after 1000 s it is more or less constant. The hottest line (284.2) has then increased by six orders of magnitude, while the coldest (184.5) has increased by a factor ten.

The helium line shows a different pattern after the rise in the first few hundred seconds. Thereafter, the intensity is almost constant until $t =$

500 s, and then it falls of slowly the rest of the simulation, ending up having increased by less than a factor ten.

As in the previous experiment, we take a look at the number density of the upper level that contributes to each of the lines and examine whether the changes in this variable relates to the changes in density and temperature, and if it can explain the variations in intensity. n_u is plotted for the iron lines in Figure 5.16 and for the helium line in Figure 5.17.

At the onset of the simulation, the two coldest iron lines, Fe X 184.5 Å and Fe XI 188.2 Å, are formed mainly in the upper parts of the loop. n_u for these lines is plotted in the upper left and upper middle panel of Figure 5.16, respectively. As the temperature starts rising, the lower corona is getting warm enough and the upper corona is getting too warm for these ions to be formed in sufficient numbers. Therefore, the number density falls in the loop apex and increases in the transition region and lower corona. These changes cause the varying intensity the first 100 s for these lines. As the density starts increasing after 80 s, n_u increases in all parts of the loop, and the intensity starts rising. At the end of the simulation, n_u for the 184.5 line has increased by a factor ten and for the 188.2 line by a factor hundred.

The number density of the upper level of the four hotter iron lines, Fe XII 195.1 Å, Fe XIII 202.0 Å, Fe XIV 274.2 Å, and Fe XV 284.2 Å, increases all over the loop. n_u for these lines is plotted in the middle left, middle right, lower left, and lower right panels of Figure 5.16, respectively. The lines n_u increases rapidly in the beginning of the simulation, because of the enormous rise in temperature. This explains the rapid intensity growth during the first 100 s of the simulation. The 195.1, 202.0 and 274.2 lines get a small 'bump' at the apex at $t = 280$ s, probably because of the temperature there being greater than their temperature of peak abundance. n_u continues to increase after $t = 280$ s, even if the temperature goes down, since the density is still rising. At the end of the simulation, n_u for the 284.2 line has increased by six orders of magnitude, the 274.2 by five orders of magnitude, the 202.0 line by three orders of magnitude, and the 195.1 line by two orders of magnitude. This matches the intensity variations.

The number density of the upper level of the He 256.3 Å line is plotted in Figure 5.17. The peak abundance of this line is at $10^{4.9}$ K, but the contribution function is non-zero up until 10^6 K (cf. Figure 4.4). As the temperature rises in the loop apex, n_u decreases there, which can be seen in the left panel of the figure. At the same time, n_u increases in the transition region and lower corona, so that in total n_u increases. After 80 s the density starts rising, causing n_u, and thus the intensity, to increase even further. n_u is increasing the first 280 s, and then decreases slightly as the temperature falls. n_u increases from $t = 0$ s to $t = 2500$ s by almost a factor ten, which is the same as for the intensity. The moving transition region is clearly visible in the right panel of Figure 5.17.

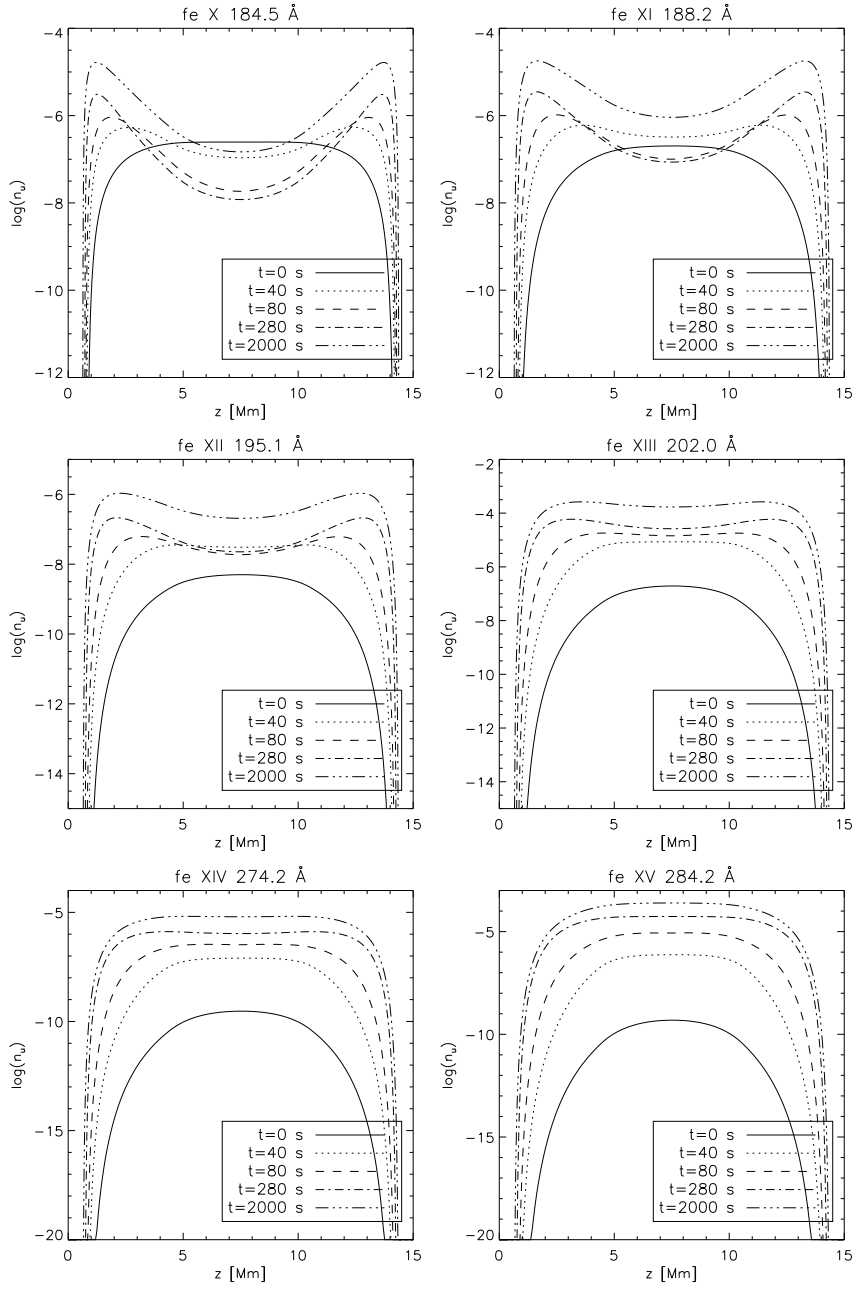

Figure 5.16: Variations in the number density of the upper level (n_u) for the EIS spectral lines Fe X 184.5 Å (upper left panel), Fe XI 188.2 Å (upper right panel), Fe XII 195.1 Å (middle left panel), Fe XIII 202.0 Å (middle right panel), Fe XIV 174.2 Å (lower left panel), and Fe XV 284.2 Å (lower right panel) as a function of the loop distance (z) plotted for different times. The curves are labeled in the same manner as in Figure 5.12.

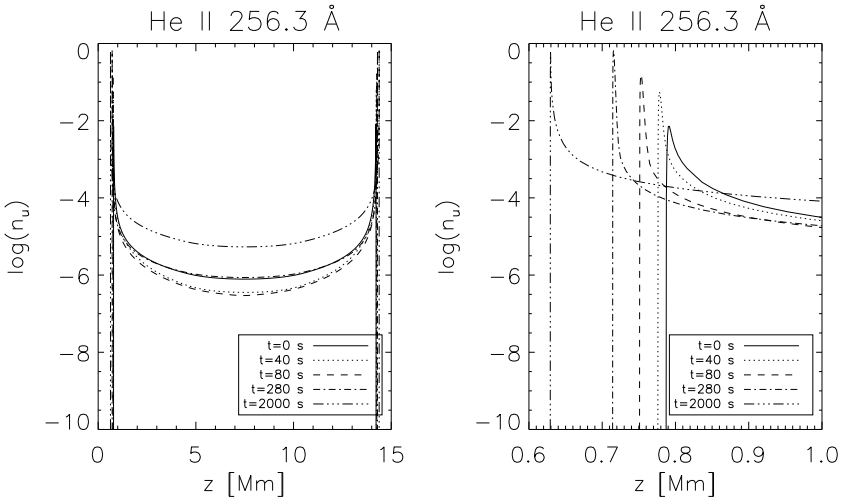

Figure 5.17: Variations in the number density of the upper level (n_u) for the EIS spectral line He II 256.3 Å as a function of the loop length (z) plotted for different times. The left panel shows the whole loop, while the right panel only shows the left transition region. The curves are labeled in the same manner as in Figure 5.12.

Doppler Velocity

The Doppler velocity for the lines discussed above is plotted in Figure 5.18. The iron lines show both the sound wave bouncing back and forth in the corona the first 300 s and the mass flux towards the apex. The helium line shows only the first period of the sound wave and a small mass flow towards the apex until $t = 700$ s, before it shows essentially no velocity.

At the onset of this simulation all iron lines are formed in the corona, whereas the helium line is formed in the transition region. Because of the lower density in the loop apex the iron lines show more of the wave pattern than the helium line does.

As in the previous experiment the lines with lowest temperature of peak abundance, except the helium line, have the greatest Doppler velocity. The reason for this is that the lines formed furthest down in the loop contribute more to the line of sight velocity. After 80 s the loop velocity is at its maximum, with greatest amplitude around $z = 5$ Mm (and $z = 10$ Mm). Therefore, the iron lines, which are formed in this region, have their greatest Doppler velocity at this time. The helium line has its maximum velocity a bit later when the maximum loop velocity amplitude reaches the region of the helium line's peak abundance. As the loop stabilizes, the mass flow decreases, until there are essentially now velocities left after 2000 s.

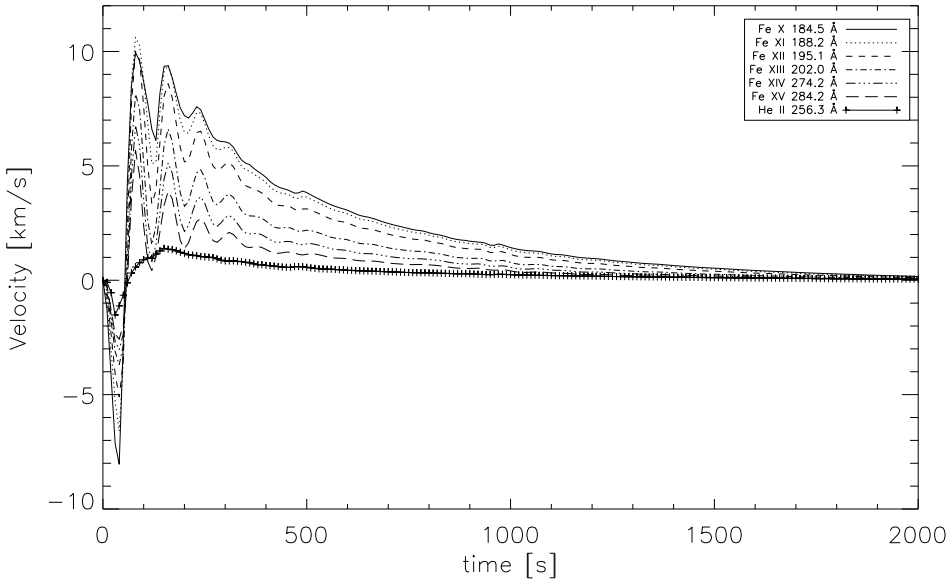

Figure 5.18: Doppler velocity variations for the EIS spectral lines Fe X 184.5 Å (solid), Fe XI 188.2 Å (dotted), Fe XII 195.1 Å (dashed), Fe XIII 202.0 Å (dash-dotted), Fe XIV 174.2 Å (dash-dot-dot-dotted), Fe XV 284.2 Å (long dashes), and He II 256.3 Å (plus) as a function of time. Velocities are defined as positive towards a detector situated vertically above the loop apex.

5.3.3 Ionization Equilibrium

As in the previous section, we want to examine whether any of our lines go out of equilibrium during the simulation. This is done by looking at how the fraction of the number density of the upper level of the line to the total density of that element is, compared to the contribution function. This is plotted as a function of temperature and for different times for the iron lines in Figure 5.19 and for the helium line in Figure 5.20.

At $t = 0$ s all our lines are in ionizational equilibrium. This is expected since the loop was relaxed into a steady state before the onset of the simulation. Despite the rapid changes in temperature and the subsequent mass flows in the beginning of this simulation, none of our iron lines go far out of equilibrium.

The helium line, on the other hand, does go out of ionizational equilibrium. Already after 40 s, the n_u peak of this line has moved to a higher temperature than it should be at in equilibrium. The line continues to stay out of equilibrium for at least the next 300 s, but has returned to equilibrium at $t = 2000$ s when the loop is back in a steady state.

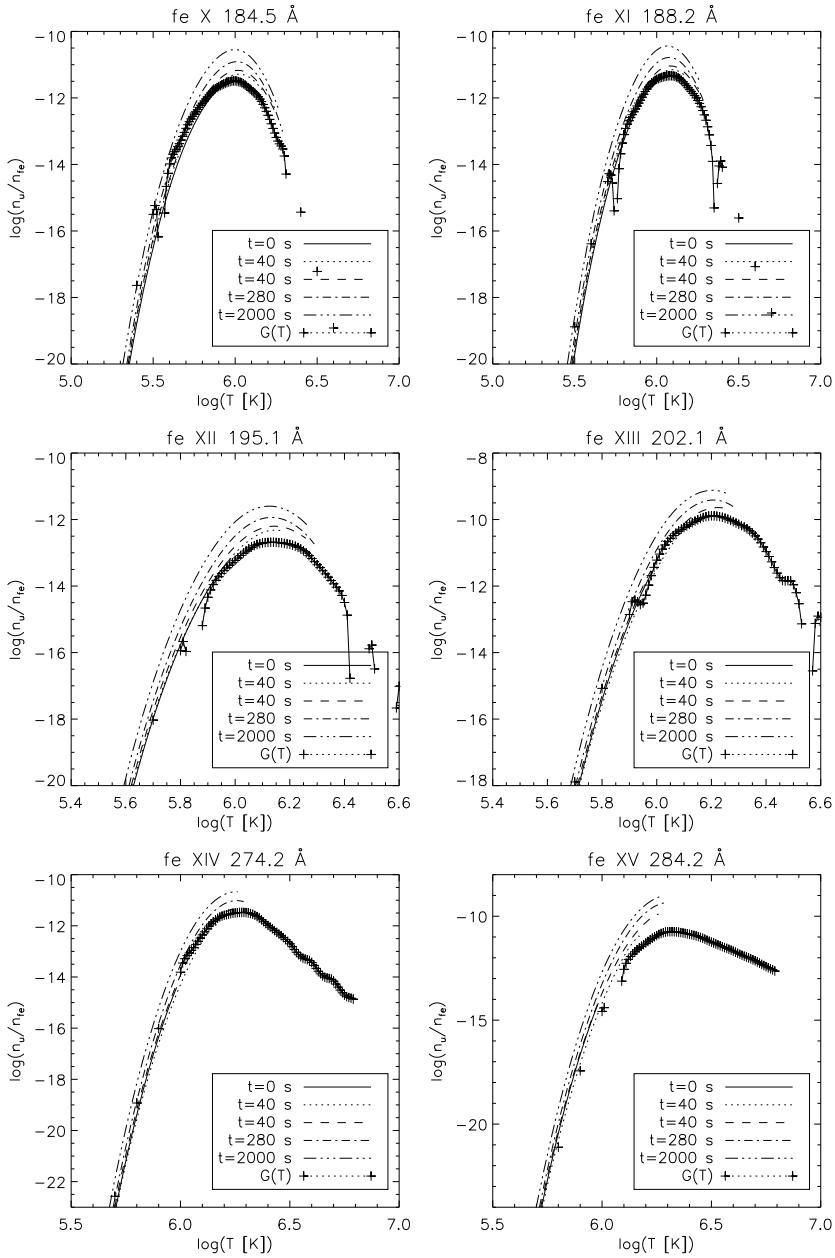

Figure 5.19: Variations in the ratio of the number density of the upper level (n_u) to the total number density of iron for the EIS spectral lines as a function of temperature and for different times. Fe X 184.5 Å (upper left panel), Fe XI 188.2 Å (upper right panel), Fe XII 195.1 Å (middle left panel), Fe XIII 202.0 Å (middle right panel), Fe XIV 174.2 Å (lower left panel), and Fe XV 284.2 Å (lower right panel). The curves are labeled in the same manner as in Figure 5.12. All panels are over-plotted by the contribution function of the line (plus) in arbitrary units.

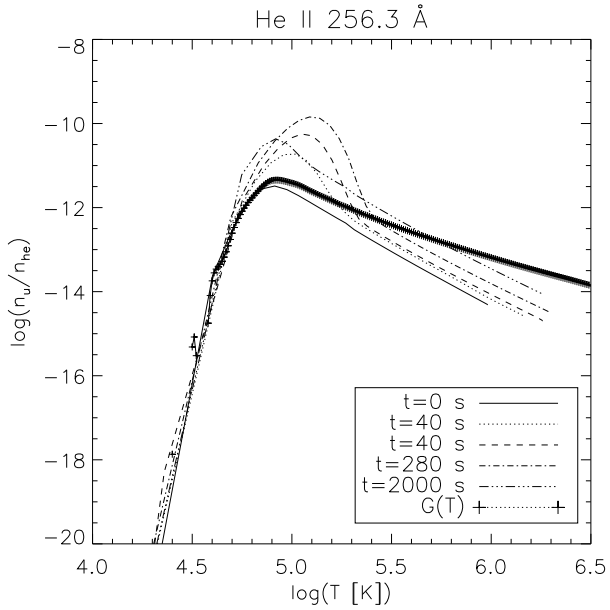

Figure 5.20: Variations in the ratio of the number density of the upper level (n_u) for He II 256.3 Å to the total number density of helium as a function of temperature and for different times, over-plotted by the contribution function of the line (plus) in arbitrary units. The curves are labeled in the same manner as in Figure 5.12.

5.3.4 Interim Conclusion

We have in the previous sections discussed the real changes in temperature, velocity and density in our loop model, as a consequence of the abrupt increase of heat input at time $t = 0$ s, and how these changes affect some of the EIS spectral lines. It is now time to discuss which of these changes EIS would actually be able to detect.

The iron lines, and especially those with low temperature of peak abundance, show great Doppler velocity amplitudes the first few hundred seconds after the onset of the simulation. The detector will probably be able to detect these mass flow velocities of more than 5 km/s, but not likely notice the sound wave signal because of the rapid amplitude damping. EIS will not be able to detect the Doppler velocities of the helium line and the iron lines with highest temperature of peak abundance. The great intensity increase in the iron lines will surely be noted by EIS. The Fe 284.2 Å line increases with five orders of magnitude in only 100 s. The helium line and the iron lines with low temperature of peak abundance do not have this violent increase in intensity. The He II 256.3 Å and Fe X 184.5 Å increase by about an order of magnitude. Both the Doppler velocity and the intensity increase would indicate a change in the heating rate, causing the temperature in the loop to rise.

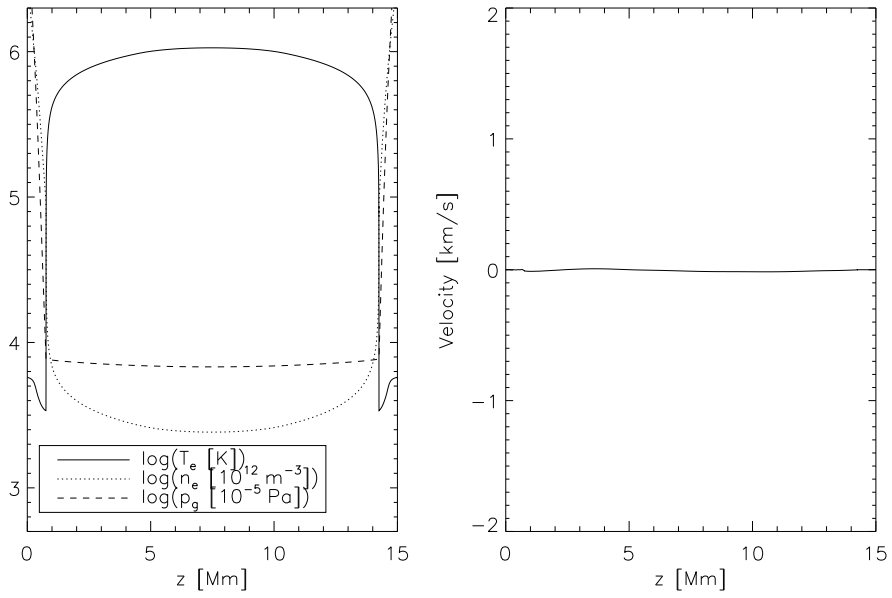

Figure 5.21: Left panel: The initial distribution of temperature (solid), pressure (dashed) and electron density (dotted) with distance (z) along loop. Right panel: The initial velocity distribution with distance (z) along loop.

We also see that care must be taken with ionization equilibrium assumptions. The He II 256.3 Å line observed by EIS is easily brought out of equilibrium by the heating event that defines this simulation.

5.4 Medium Hot Loop with Waves

An initially medium hot loop has been constructed and is shown in Figure 5.21. In the left panel we plot the logarithm of the temperature, pressure, and electron density as functions of position along the loop (z). In the right panel we plot the plasma velocity as a function of z.

The temperature is of order 6000 K in the loop footpoints. At $z \approx 0.8$ Mm the transition region begin, and the temperature rises to some 1.1 MK over a few Mm. This temperature structure is maintained by an input heat flux of 850 W/m^2 in both sides of the loop, deposited from $z_0^{left} = 4.5$ Mm and $z_0^{right} = 10.5$ Mm, with a scale height $z_H^{left} = z_H^{right} = 4.0$ Mm. The electron density starts out at 3×10^{18} m^{-3} in the footpoints and decreases to 2×10^{16} m^{-3} in the upper part of the chromosphere. In the transition region the density drops of even more, and continues to fall down to some 10^{15} m^{-3} in the corona.

The pressure starts of at 100 Pa in the footpoints, decreasing rapidly to

less than 0.1 Pa until the end of the transition region. As the temperature rises, the pressure scale height increases and the pressure is almost constant through the upper parts of the loop. As seen in the right panel of Figure 5.21, the velocity is nearly zero through the entire initial model.

At time $t = 0$ we start forcing on waves from the left footpoint of the loop. To introduce the sound wave, the lower left boundary moves as a piston with velocity

$$u = u_{\text{amp}} \cos\left(2\pi f_r t - \pi/2\right) , \tag{5.4}$$

where t is the time, $f_r = 0.0056$ Hz is the frequency (three minute oscillation), and $u_{\text{amp}} = 0.7$ km/s is the amplitude. No other changes are made.

5.4.1 Loop Changes

Now we describe the morphology of the loop plasma in terms of the thermodynamical variables temperature, velocity, and density, and study the changes caused by the forced oscillation.

Velocity

There are no movements in the loop at the onset of the simulation, but starting at $t = 0$ s we force a wave from the left footpoint every 180 s. The loop velocity the first hour of the simulation can be seen in the left panel of Figure 5.22. A wave can be seen traveling from left to right, the first starting from the left transition region ($z \sim 1$ Mm) after 100 s, and then a new wave starts every 180 seconds. At first, the velocity amplitude increases for each oscillation, but from $t = 1000$ s the amplitude is constant. The right panel of the same figure shows the footpoint to footpoint velocity profile as a function of the loop length for chosen time steps through one wave period.

The first wave is visible in the lower left part of the corona after 100 s. In the chromosphere the pressure is about 100 Pa and the density is about 10^{-6} kg/m^3, which yield a sound speed of some 10 km/s. With this speed it should take about 60 s to pass trough the chromosphere, where the density is high, so the wave amplitude will be small and barely visible. In addition, with the piston movement given in Equation 5.4, the first sound wave maximum originates in the left footpoint ($z = 0$) after some 45 s. Therefore, the wave is first visible when it reaches the corona after some 100 s, as is shown in the left panel of Figure 5.22.

In the corona the pressure is about 0.07 Pa and the density is about 5×10^{-12} kg/m^3, which yield a sound speed of 150 km/s. As in the two previous experiments, the wave is reflected when it reaches the right footpoint transition region due to the rapid reduction in sound speed. With this sound speed and a distance of some 13.5 Mm from one transition region to the other, it should take the wave about 180 s back and forth through the corona. This is exactly what is seen in the left panel of Figure 5.22; a new wave is starting

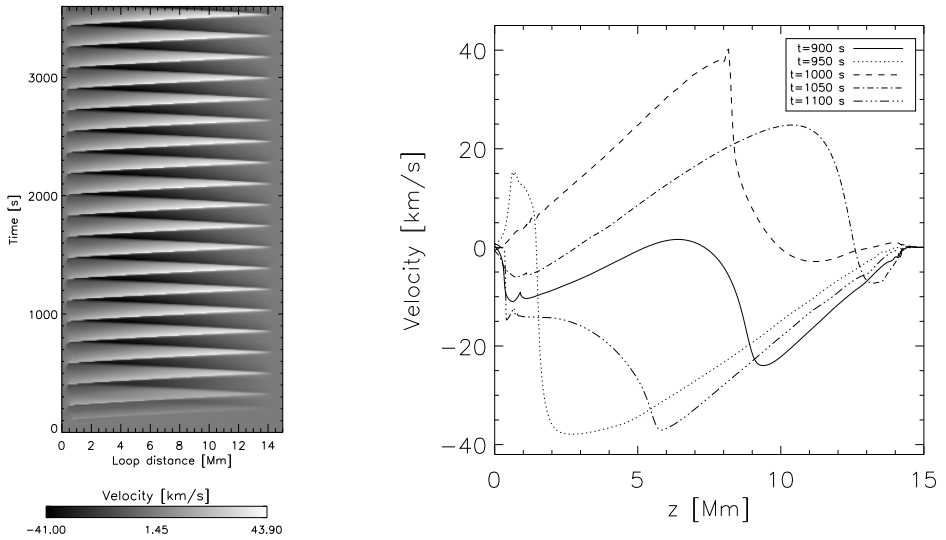

Figure 5.22: Velocity variations in the loop with forced oscillations. Left panel: Temporal evolution of the velocity along the loop. Right panel: A time series of footpoint to footpoint velocity profiles as a function of the distance (z) along the loop taken at $t = 900$ s (solid), $t = 950$ s (dotted), $t = 1000$ s (dashed), $t = 1150$ s (dash-dotted), and $t = 1100$ s (dash-dot-dot-dotted).

when the previous one has come back to the left transition region. The first few waves show greater and greater velocity amplitude because the reflected wave is added to the new. After some 1000 s an equilibrium situation has occurred, and all successive waves have the same amplitude.

In the right panel of Figure 5.22 we follow the sixth wave, starting at $t = 900$ s. The new wave is starting from $z = 0$ Mm, but is not yet visible, while the previous wave has been reflected and is moving back towards the loop apex. At $t = 950$ s, the wave has come up into the transition region and the amplitude has increased, an effect of the reduced density. 50 s later, the wave amplitude is at its maximum, some 40 km/s, passing the loop apex. At $t = 1050$ s, the wave has been reflected at the right transition region and is moving back towards the loop apex. Another 50 s later, the wave is still moving towards lower z-values, now passing the loop apex again. At the same time, a new wave is forming at $z = 0$ Mm. The amplitude of the reflected wave is slightly less than the one of the original wave.

Density and Temperature

The waves we are forcing on the system are sound waves, which of course compress the plasma as they travel along the loop, causing the density and temperature to increase. At the same time, the density and temperature are

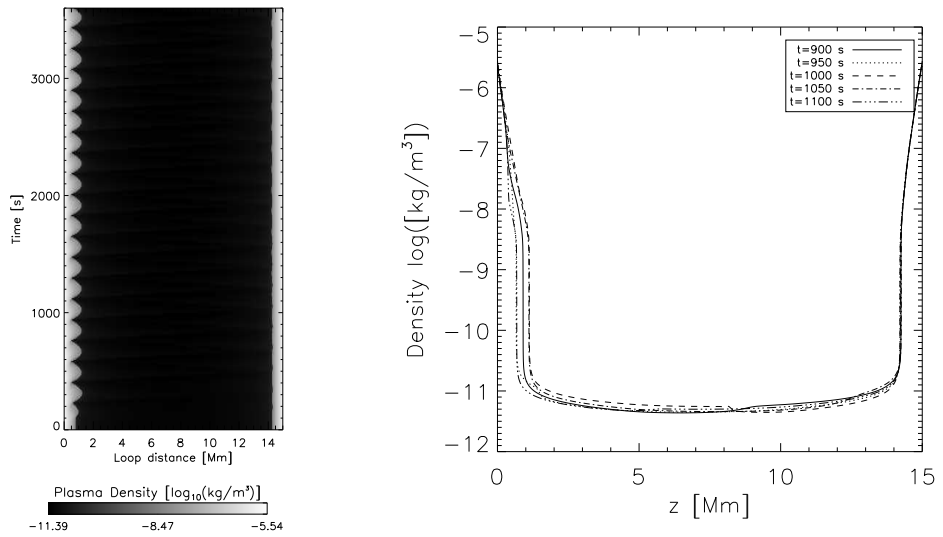

Figure 5.23: Density variations in the loop with forced waves. Left panel: Temporal evolution of the density along the loop. Right panel: A time series of footpoint to footpoint density profiles as a function of the distance (z) along the loop. The lines are labeled as in Figure 5.22.

reduced in the tracks of the previous wave front, with a minimum 90 s after the maximum. The evolution of the loop density can be seen in Figure 5.23 and the loop temperature in Figure 5.24. The left panels show the evolution the first hour after we started forcing on the waves, while the right panels show the footpoint to footpoint density and temperature, respectively, along the loop for some chosen times.

At $t = 900$ s, the previous wave has been reflected and is now moving towards lower z-values. This can be seen by the density decrease in the left hand side of the loop, in the tracks of the wave before it was reflected, and the increased density around the wave at $z = 10$ Mm. No effect of the new wave that is forming can yet be seen in the left footpoint. The transition region is oscillating with a period of 180 s, moving some 0.3 Mm up and down from its starting point, which can be clearly seen in the left panel of Figure 5.23. At $t = 950$ s, the new wave reaches the beginning of the transition region, where the density now is at its minimum. At $t = 1000$ s, the wave passes the apex and increases the density there. As the wave is reflected, the wave amplitude in the left footpoint reaches its maximum. 50 s later, the increased density due to the reflected wave can be seen at the right transition region. The reflected wave increases the density, but not as much as it did before it was reflected.

In addition to the increased density in the region of the wave peak, there is always a temperature increase too, as can be seen in the right panel of

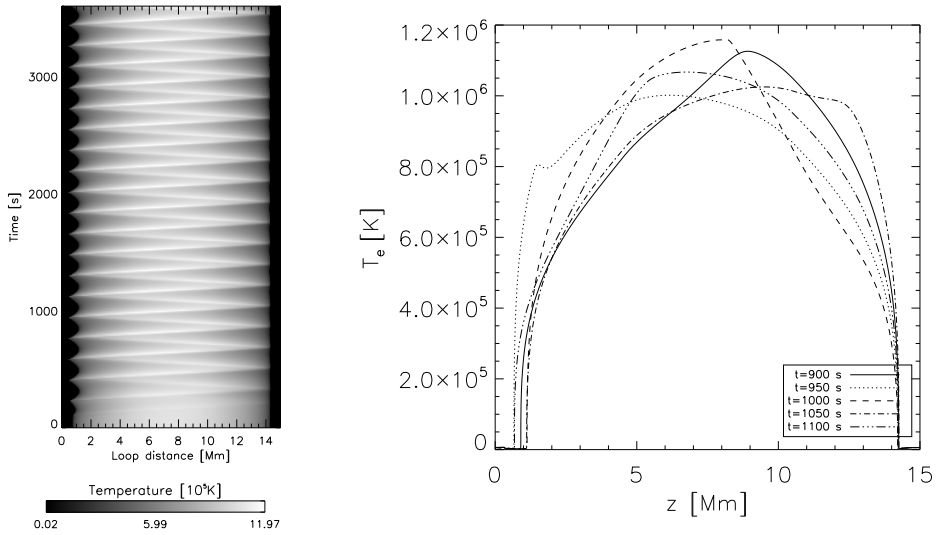

Figure 5.24: Temperature variations in the loop with forced oscillations. Left panel: Temporal evolution of the temperature along the loop. Right panel: A time series of footpoint to footpoint temperature profiles as a function of the distance (z) along the loop. The lines are labeled as in Figure 5.22.

Figure 5.24. The temperature increase is, as for the density, smaller when it is the reflected wave that passes. The velocity amplitude is largest in the upper parts of the loop, where the density is smallest. The propagating wave amplitude, the reduced temperature in the tracks of the previous wave, and the moving transition region is clearly seen in the temperature plot in the left panel of the same figure.

5.4.2 The EIS Lines' Response to the Changes

Now we take a look at how to the EIS spectral lines react to the loop changes in temperature, density, and velocity described above. The lines' intensity and velocity now to be discussed are calculated according to the line momentum analysis described in Section 2.4.2.

We are discussing the same lines as in the two previous experiments. Their wavelength and temperature of peak abundance are listed in Table 5.1.

Intensity

The changes in the lines' intensity as a function of time is shown in Figure 5.25. All lines show oscillating intensities with periods of some 180 s. The amplitudes are increasing for every new wave for the first 1000 s and then

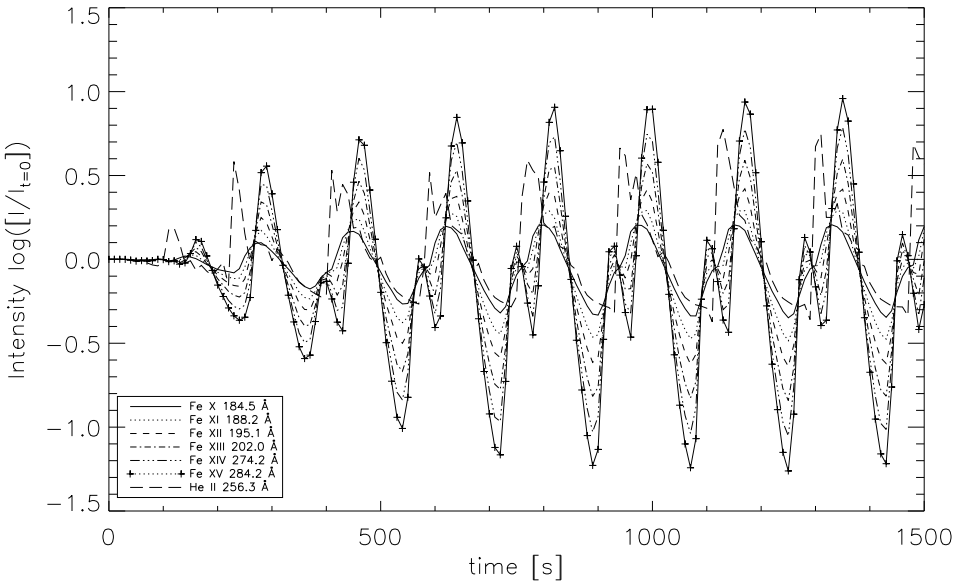

Figure 5.25: Intensity variations for the EIS spectral lines Fe X 184.5 Å (solid), Fe XI 188.2 Å (dotted), Fe XII 195.1 Å (dashed), Fe XIII 202.0 Å (dash-dotted), Fe XIV 174.2 Å (dash-dot-dot-dotted), Fe XV 284.2 Å (plus), and He II 256.3 Å (long dashes) as a function of time. The intensities are normalized to one at $t = 0$ s.

stabilizes. The iron lines are in phase, but have different amplitudes. The ions with highest temperature of peak abundance show the greatest intensity variations, with Fe XV 284.2 Å increasing and decreasing with more than a factor ten. The helium line has its top some 50 s earlier and its bottom some 50 s later than the iron lines. This line has at maximum three times its original intensity.

Let us now see if we can explain the varying intensities by the changes in the loop morphology. As the wave passes, both the density and the temperature increase, and afterwards they both decrease, as discussed above. This cause the number density of the upper levels of our lines (n_u) to change according to Equation 5.3,

$$n_u \propto \rho^2 f(T)\,.$$

This again affects the intensity as stated in Equation 2.2,

$$I_\nu = \frac{h\nu}{4\pi} \int_0^s n_u A_{ul}\, \phi_\nu \, ds\,.$$

The number density of the upper level for the iron lines is plotted in Figure 5.26 and for the helium line in Figure 5.27.

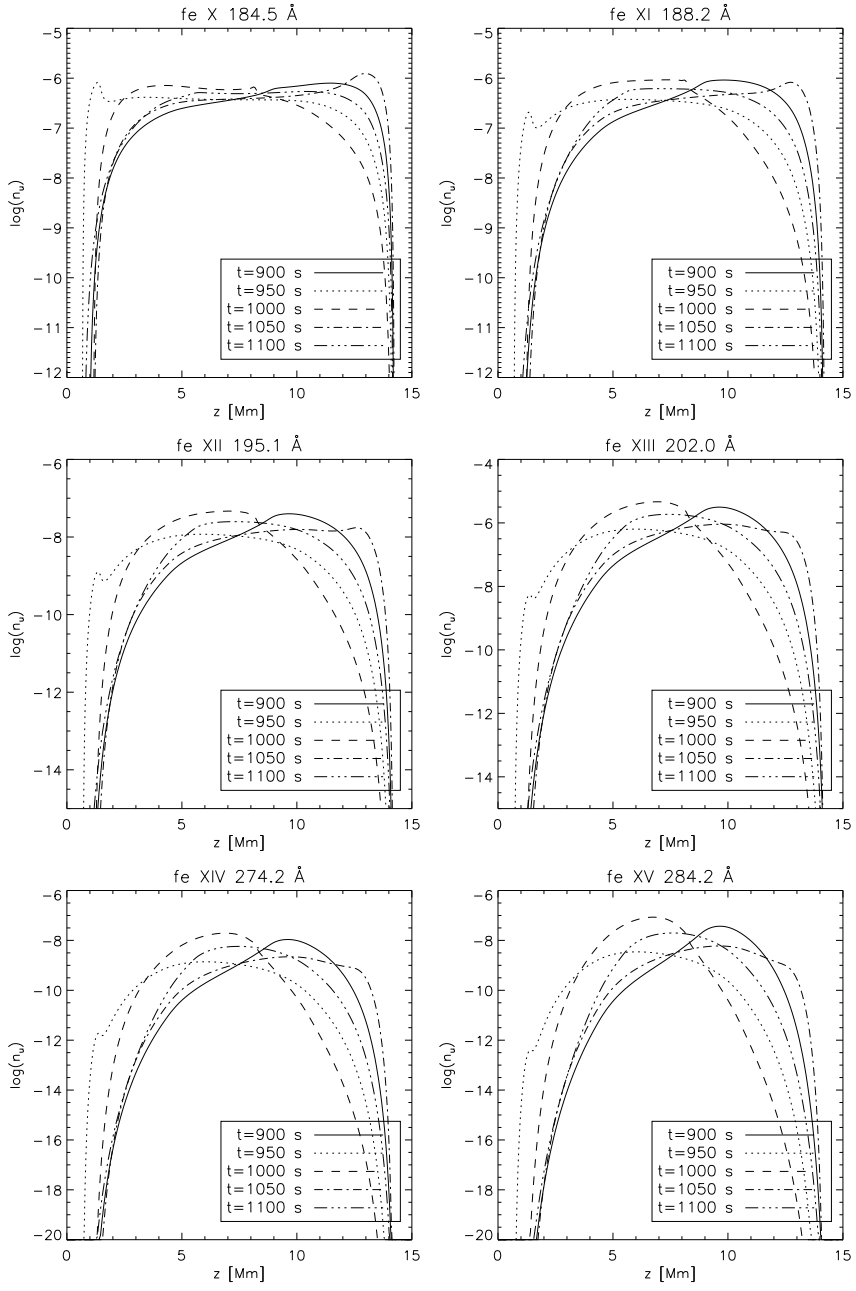

Figure 5.26: Variations in the number density of the upper level (n_u) for the EIS spectral lines Fe X 184.5 Å (upper left panel), Fe XI 188.2 Å (upper right panel), Fe XII 195.1 Å (middle left panel), Fe XIII 202.0 Å (middle right panel), Fe XIV 174.2 Å (lower left panel), and Fe XV 284.2 Å (lower right panel) as a function of the loop distance (z) plotted for different times. The curves are labeled in the same manner as in Figure 5.24.

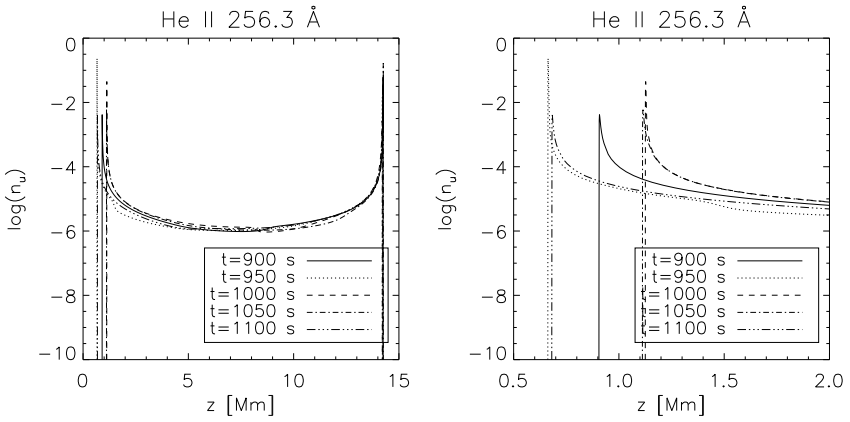

Figure 5.27: Variations in the number density of the upper level (n_u) for the EIS spectral line He II 256.3 Å plotted for different times. The left panel shows the whole loop, while the right panel shows only the left transition region. The curves are labeled in the same manner as in Figure 5.24.

At $t = 900$ s, the wave is in the right part of the loop, which can be seen by the increased n_u in all panels of Figure 5.26. At the same time, n_u is decreased in the left part of the loop including the loop apex, due to the reduced density and temperature in the track of the wave that just passed by. Therefore, the iron lines have reduced intensity. The larger the line's temperature of peak abundance is, the greater is the reduction in the left part of the loop, causing the warmest lines to have the greatest drop-off in intensity. A few tens of seconds later the reflected wave passes the loop apex, and the temperature and density in this area increase. This give a small growth in the iron lines' intensity. The helium line, which is now partly formed in the reduced density area from the previous wave, has almost its lowest intensity.

At $t = 950$ s, the new wave has reached the left transition region. This can be seen by the n_u increase in this region in all panels of Figure 5.26. But, at the same time the n_u reduction in the right hand side including the apex, is much greater than the increase, which causes these lines to have reduced intensity. The helium line has a larger population in the upper level now, due to the down-movement of the transition region. Therefore, the helium line brighten. As the wave reaches the corona, some 30 s later, the intensity of the iron lines also increases. The density is lowest in the loop apex, causing the wave amplitude, and thus the density and temperature to increase more in this region. Therefore, the lines with highest temperature of peak abundance, which are formed furthest up in the loop, show the largest intensity amplitude. This amplitude is at its maximum when the wave passes the loop apex at $t = 1000$ s. As the wave passes, n_u increases in the right side of the loop, but falls off in the left part and the loop apex, so the the

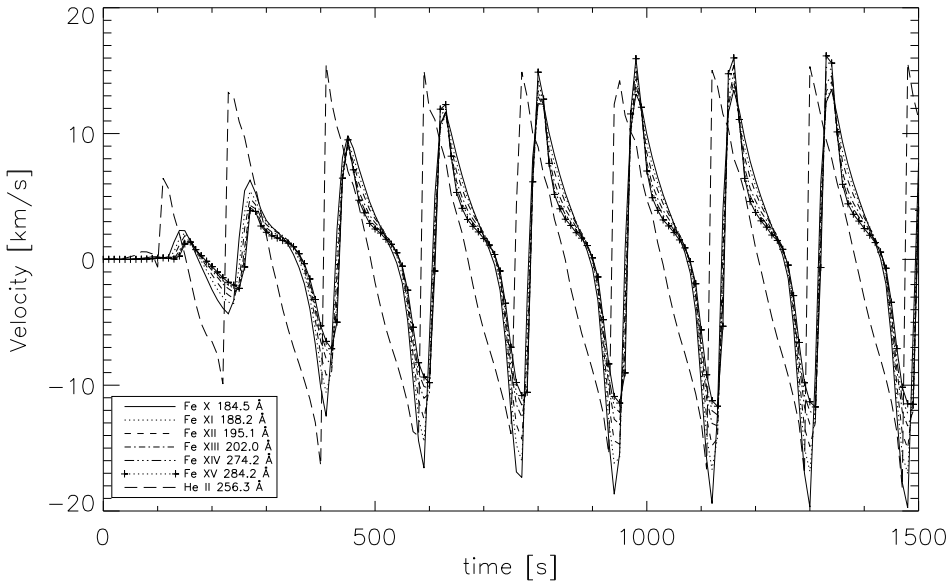

Figure 5.28: Doppler velocity variations for the EIS spectral lines Fe X 184.5 Å (solid), Fe XI 188.2 Å (dotted), Fe XII 195.1 Å (dashed), Fe XIII 202.0 Å (dash-dotted), Fe XIV 174.2 Å (dash-dot-dot-dotted), Fe XV 284.2 Å (long dashes), and He II 256.3 Å (plus) as a function of time. Velocities are defined as positive towards a detector situated vertically above the loop apex.

total n_u is reduced. Therefore, the intensity of the iron lines is reduced. As the transition region moves upwards, the total n_u for the helium line also falls, causing this line's intensity to decrease. After 180 s a new wave starts forming, and the variations are repeated.

Doppler Velocity

The Doppler velocity for the lines discussed above is plotted in Figure 5.28. All lines show a wave pattern with periods of 180 s, but the helium line is a bit out of phase compared to the iron lines. The helium line and the iron lines with highest temperature of peak abundance are the ones with largest positive amplitude, while the iron lines with lowest temperature of peak abundance have greatest negative amplitude. As for the intensity, the velocity amplitude is increasing for the first 1000 s and is thereafter constant. The velocity peak is then some 15 km/s for the helium line and -20 km/s for the Fe X 184.5 Å line.

At $t = 900$ s, the reflected wave causes most of the loop plasma to travel towards the left hand side of the loop, with less movement in the apex and most movement in the left transition region. This causes the iron lines to show almost no velocity while the helium line shows negative velocity. As

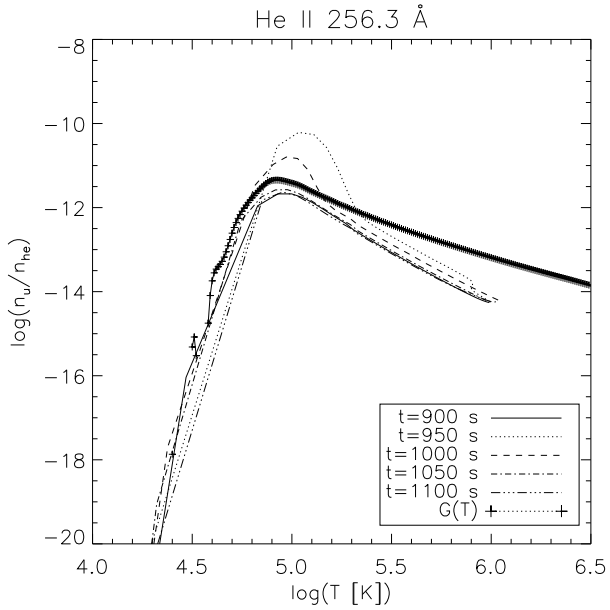

Figure 5.29: Variations in the ratio of the number density of the upper level (n_u) for He II 256.3 Å to the total number density of helium as a function of temperature and for different times, over-plotted by the contribution function of the line (plus) in arbitrary units. The curves are labeled in the same manner as in Figure 5.24.

the wave passes the loop apex, the iron lines show negative velocity too. Some 40 s later, the new wave passes through the transition region where the helium line is formed. Thus, this line changes instantly from a negative to a positive velocity. At this time the iron lines still show negative velocity, but a few tens of seconds later, when the wave reaches the area where the iron lines are formed, they get a positive velocity too. As the wave passes the loop apex around $t = 1000$ s, all lines still have positive velocity, but the amplitudes are decreasing.

5.4.3 Ionization Equilibrium

As in the two previous experiments, we want to examine whether any of our lines go out of equilibrium during the simulation. This is done by looking at how the fraction of the number density of the upper level of the line to the total density of that element is, compared to the contribution function. This is plotted as a function of temperature and for different times for the iron lines in Figure 5.30 and for the helium line in Figure 5.29.

At the onset of the simulations the loop is in a steady state and thus all lines are in ionization equilibrium. Despite the forced waves, with subsequent changes in temperature and density, none of our iron lines go far out of equilibrium. The helium line on the other hand, does go out of ionizational

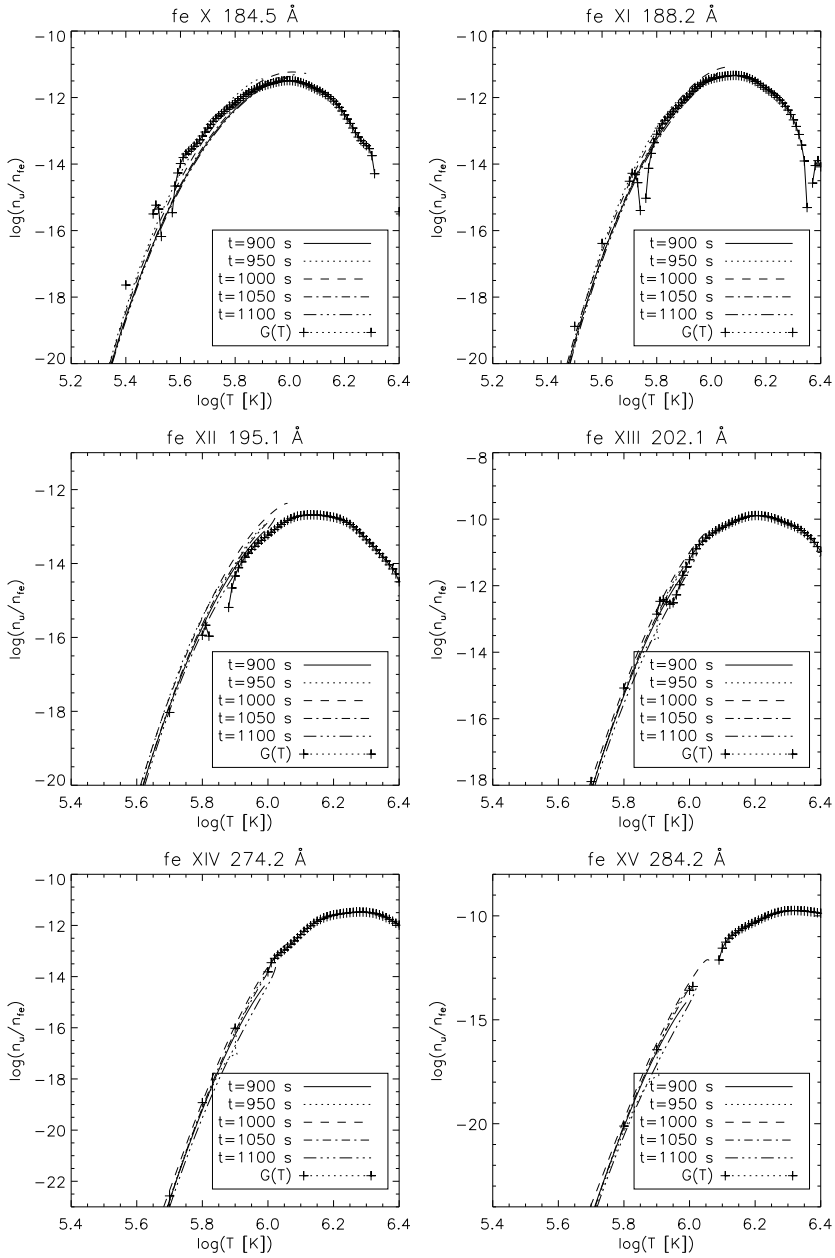

Figure 5.30: Variations in the ratio of the number density of the upper level (n_u) to the total number density of iron for the EIS spectral lines as a function of temperature and for different times. Fe X 184.5 Å (upper left panel), Fe XI 188.2 Å (upper right panel), Fe XII 195.1 Å (middle left panel), Fe XIII 202.0 Å (middle right panel), Fe XIV 174.2 Å (lower left panel), and Fe XV 284.2 Å (lower right panel). The curves are labeled in the same manner as in Figure 5.24. All panels are over-plotted by the contribution function of the line (plus) in arbitrary units.

equilibrium. As the sound wave passes through the transition region, e.g. at $t = 950$ s, the greatest number density of He II ions is transported to a warmer part of the loop than it would normally be, because of the large temperature gradient in this region. This is easily seen at $t = 950$ s in Figure 5.29. As the mass flow is reduced the helium line starts returning to equilibrium, and reaches it before $t = 1050$ s.

5.4.4 Interim Conclusion

We have in the previous sections discussed the real changes in temperature, velocity, and density in our loop as a result of the forced sound waves, and examined how this would affect some of the EIS spectral lines. It is now time to discuss which of these changes EIS would actually be able to detect.

All our spectral lines show Doppler velocity oscillations with a period of 180 s. With amplitudes of more than 10 km/s EIS will clearly be able to detect these. The iron lines with highest temperature of peak abundance show an intensity increase and decrease of about one order of magnitude, while the iron lines with lowest temperature of peak abundance only show 50 per cent variation. All have a period of 180 s. Even though these intensity changes are not as violent as for the previous experiments, they should still be detected by EIS. Both the intensity variations and the Doppler velocities will indicate a three minute oscillation traveling through the loop, changing the density and temperature.

We also find that the He II 256.3 Å line might be brought out of equilibrium when waves travel through the loop, as observed in this simulation. The iron lines do not go far out of equilibrium, and should thus be safe to use for temperature and density diagnostics.

Chapter 6

Conclusion

6.1 Summary

The aim of this thesis is to find out more about how we can relate the EIS observations to the physical phenomena in the solar atmosphere. More explicitly, we want to examine how the EIS spectral emission lines' intensity and velocity react to temperature, density, and velocity changes. We are especially interested in the iron lines formed in the corona around 10^6 K. To solve this problem we do numerical simulations of phenomena in the solar atmosphere and estimate how the quantities detectable with EIS react to the changes.

Before we start simulating, we need to know which spectral lines are observable with EIS. To identify these lines, we make use of a Solarsoft (Bentely and Freeland, 1998) program based on the CHIANTI atomic database (Dere et al., 1997; Landi et al., 2006). We need lines for which the velocity is possible to resolve with an accuracy better than 5 km/s with 60 seconds quiet sun observation. The following lines fulfill our demands: Fe X 184.5 Å, Fe XII 186.9 Å, Fe XI 188.2 Å, Fe XII 192.4 Å, Fe XI 192.8 Å, Fe XII 193.5 Å, Fe XII 195.1 Å, S VIII 198.6 Å, Fe XIII 202.0 Å, He II 256.3 Å, Fe XIV 274.2 Å, and Fe XV 284.2 Å. The helium line is actually two separate lines, 256.317 Å and 256.318 Å, but we treat them as only one line. This line is blended by Si X 256.4 Å.

As the EIS spectral lines are found, we design atomic models including these lines. We concentrate on the design of the iron atomic model, but we also make small modifications to the helium atomic model. The atomic data are mostly found from the HAO-DIAPER package (Judge and Meisner, 1994), but supplied with data from the CHIANTI atomic database and the NIST online database (Ralchenko et al., 2005).

For our numerical calculations we use the simulation code TTRANZ (Hansteen, 1991). This program solves the hydrodynamic plasma equations in one dimension, along with the rate equations which determine the radiat-

ive losses from the transition region and corona. The code simulates a plasma caught in a semi-circular magnetic loop with footpoints in the chromosphere, stretching through the transition region and up into the corona.

We do three simulation runs; a warm loop cooling, a cold loop heating, and a medium warm loop with forced waves. Before each run we let the system relax into a steady state, to isolate the effects we want to study. In the two first simulations we alter the heat input while in the last we force three minute waves on the system from the left footpoint. For each of the runs we analyze how the temperature, velocity, and density change in the different parts of the loop as a result of these events. We also examine how the EIS spectral emission lines react.

Intensity variations can be seen in all our lines, with the most extreme, Fe XV 284.2 Å, changing by several orders of magnitude in the two first experiments. Doppler velocities are also measured from our lines. The lines showing the largest velocities are He II 256.3 Å in the cooling loop experiment and Fe X 184.5 Å in the heating loop experiment. All our simulations cause sound waves to propagates in the corona. These signals can only be resolved with EIS in the wave experiment.

We are also interested in whether our lines are driven out of ionization equilibrium. We find that none of our iron lines go far out of equilibrium during any of our simulations, but that the helium line does. Therefore, care must be taken when the helium line is used for temperature and density diagnostic. The iron lines should be safe to use, at least as long as the event is not much more dramatic than in our simulations.

Changes in the EIS spectral lines' intensity and Doppler velocity can thus give us information about events in the solar atmosphere. The iron lines should be safe to use for temperature and density diagnostics, while care has to be taken with the helium line.

6.2 Further work

There are still more work that can be done to get a better understanding of the interpretation of the EIS data. First of all, we can do better examinations of which EIS spectral lines that are usable. We have only gone through the lines which have good enough resolution in quiet sun. The list for active regions and flares would contain more lines. Secondly, the design of the atomic models can be done in a more thorough way. We only included the energy levels that contain more than five per cent of the total population of the ion. To make a more qualified guess of which levels it is safe to remove, we should remove one level at a time, run a simulation and examine the effect on the lines' intensity due to the change. In addition, there have been published newer data, e.g. dielectronic rates coefficients by Gu (2003), and these should be examined to decide whether changes to our atomic models

should be made. At last, we do not know exactly how small intensity and velocity variations the EIS instrument is able to detect and how good our model is at representing the Sun. Thus, comparing our simulations with real data would give better understanding of the reliability of our results and conclusions. Last, but not least, further simulation experiments are needed to see how the lines respond to other types of events than discussed in the thesis.

Bibliography

Aggarwal, K. M. and Keenan, F. P. (2004). Electron impact excitation of Fe XIII. *Astronomy and Astrophysics*, 418:371–385.

Alfvén, H. (1947). Magneto hydrodynamic waves, and the heatinhg of the solar corona. *MNRAS*, 107:211–+.

Arnaud, M. and Raymond, J. (1992). Iron ionization and recombination rates and ionization equilibrium. *The Astrophysical Journal*, 398:394–406.

Arnaud, M. and Rothenflug, R. (1985). An updated evaluation of recombination and ionization rates. *Astronomy and Astrophysics Supplement Series*, 60:425–457.

Avrett, E. H., Vernazza, J. E., and Linsky, J. L. (1976). Excitation and ionization of helium in the solar atmosphere. *The Astrophysical Journal Letters*, 207:L199–L204.

Bentely, R. D. and Freeland, S. L. (1998). SOLARSOFT - an Analysis Environment for Solar Physics. In *ESA SP-417: Crossroads for European Solar and Heliospheric Physics. Recent Achievements and Future Mission Possibilities*, pages 225–+.

Biermann, L. (1946). . *Naturwissenschaften*, 33:118.

Biermann, L. (1948). Über die Ursache der chromosphärischen Turbulenz und des UV-Exzesses der Sonnenstrahlung. *Zeitschrift fur Astrophysik*, 25:161–+.

Burgess, A. (1965). A General Formula for the Estimation of Dielectronic Recombination Co-Efficients in Low-Density Plasmas. *The Astrophysical Journal*, 141:1588–1590.

Burgess, A. and Tully, J. A. (1992). On the Analysis of Collision Strengths and Rate Coefficients. *Astronomy and Astrophysics*, 254:436–453.

Carlsson, M. (1986). A computer program for solving multi-level non-lte radiative transfer problems in moving or static atmospheres. Later modifications: `http://www.astro.uio.no/~matsc/mul22`.

Culhane, J. L., Harra, L. K., James, A. M., Al-Janabi, K., Bradley, L. J., Chaudry, R. A., Rees, K., Tandy, J. A., Thomas, P., Whillock, M. C. R., Winter, B., Doschek, G. A., Korendyke, C. M., Brown, C. M., Myers, S., Mariska, J., Seely, J., Lang, J., Kent, B. J., Shaughnessy, B. M., Young, P. R., Simnett, G. M., Castelli, C. M., Mahmoud, S., Mapson-Menard, H., Probyn, B. J., Thomas, R. J., Davila, J., Dere, K., Windt, D., Shea, J., Hagood, R., Moye, R., Hara, H., Watanabe, T., Matsuzaki, K., Kosugi, T., Hansteen, V., and Wikstol, Ø. (2007). The EUV Imaging Spectrometer for Hinode. *Solar Physics*, pages 60–+.

Dere, K. P., Landi, E., Mason, H. E., Monsignori Fossi, B. C., and Young, P. R. (1997). CHIANTI - an atomic database for emission lines. *Astronomy and Astrophysics Supplemental*, 125:149–173.

Dorfi, E. A. and Drury, L. O. (1987). Simple adaptive grids for 1-D initial value problems. *Journal of Computational Physics*, 69:175–195.

Edlén, B. (1943). Die Deutung der Emissionslinien im Spektrum der Sonnenkorona. Mit 6 Abbildungen. *Zeitschrift fur Astrophysik*, 22:30–+.

Gu, M. F. (2003). Dielectronic Recombination Rate Coefficients for H-like through Ne-like Isosequences of Mg, Si, S, Ar, Ca, Fe, and Ni. *The Astrophysical Journal*, 590:1131–1140.

Gudiksen, B. V. and Nordlund, Å. (2005). An Ab Initio Approach to the Solar Coronal Heating Problem. *The Astrophysical Journal*, 618:1020–1030.

Hansteen, V. (1991). *Non-Equilibrium Effects in Solar Transition Region Physics*. PhD thesis, University of Oslo.

Ichimoto, K. and Solar-B Team (2005). The Solar-B Mission. *Journal of Korean Astronomical Society*, 38:307–310.

Ichimoto, K., Tsuneta, S., Suematsu, Y., Shimizu, T., Otsubo, M., Kato, Y., Noguchi, M., Nakagiri, M., Tamura, T., Katsukawa, Y., Kubo, M., Sakamoto, Y., Hara, H., Minesugi, K., Ohnishi, A., Saito, H., Kawaguchi, N., Matsushita, T., Nakaoji, T., Nagae, K., Sakamoto, J., Hasuyama, Y., Mikami, I., Miyawaki, K., Sakurai, Y., Kaido, N., Horiuchi, T., Shimada, S., Inoue, T., Mitsutake, M., Yoshida, N., Takahara, O., Takeyama, N., Suzuki, M., and Abe, S. (2004). The Solar Optical Telescope onboard the Solar-B. In Mather, J. C., editor, *Optical, Infrared, and Millimeter Space Telescopes. Edited by Mather, John C. Proceedings of the SPIE, Volume 5487, pp. 1142-1151 (2004).*, volume 5487 of *Presented at the Society of Photo-Optical Instrumentation Engineers (SPIE) Conference*, pages 1142–1151.

Janev, R. K., Langer, W. D., and Evans, K. (1987). *Elementary processes in Hydrogen-Helium plasmas - Cross sections and reaction rate coefficients*. Springer Series on Atoms and Plasmas, Berlin: Springer, 1987.

Joselyn, J. A., Munro, R. H., and Holzer, T. E. (1979). The validity of ionization equilibrium in highly ionized astrophysical plasmas. *The Astrophysical Journal Supplement Series*, 40:793–813.

Judge, P. G. and Meisner, R. W. (1994). The 'HAO spectral diagnostics package' (HAOS-Diaper). In Hunt, J. J., editor, *ESA SP-373: Solar Dynamic Phenomena and Solar Wind Consequences, the Third SOHO Workshop*, pages 67–+.

Kano, R., Hara, H., Shimojo, M., Tsuneta, S., Sakao, T., Matsuzaki, K., Kosugi, T., Golub, L., Deluca, E. E., Bookbinder, J. A., Cheimets, P., Owens, J. K., and Hill, L. D. (2004). SolarB X-Ray Telescope (XRT). In Sakurai, T. and Sekii, T., editors, *The Solar-B Mission and the Forefront of Solar Physics*, volume 325 of *Astronomical Society of the Pacific Conference Series*, pages 15–+.

Landi, E., Del Zanna, G., Young, P. R., Dere, K. P., Mason, H. E., and Landini, M. (2006). CHIANTI-An Atomic Database for Emission Lines. VII. New Data for X-Rays and Other Improvements. *ApJ Supplemental*, 162:261–280.

Mariska, J. T. (2005). *EIS Instrument Notes*.

Mason, H. E. and Fossi, B. C. M. (1994). Spectroscopic diagnostics in the VUV for solar and stellar plasmas. *Astronomy and Astrophysical review*, 6:123–179.

Mazzotta, P., Mazzitelli, G., Colafrancesco, S., and Vittorio, N. (1998). Ionization balance for optically thin plasmas: Rate coefficients for all atoms and ions of the elements H to NI. *The Astronomy and Astrophysics Supplement Series*, 133:403–409.

Mihalas, D. (1978). *Stellar Atmospheres, 2nd ed.* W. H. Freeman.

Osterbrock, D. E. (1961). The Heating of the Solar Chromosphere, Plages, and Corona by Magnetohydrodynamic Waves. *The Astrophysical Journal*, 134:347–+.

Parker, E. N. (1983). Magnetic neutral sheets in evolving fields. I - General theory. II - Formation of the solar corona. *The Astrophysical Journal*, 264:635–647.

Ralchenko, Y., Kramida, A., and Reader, J. (2005). Nist atomic spectra database. Online, http://physics.nist.gov/PhysRefData/ASD/index.html. Standard Reference Database #78.

Rutten, R. J. (2003). Radiative transfer in stellar atmospheres. Online, http://www.phys.uu.nl/ rutten/education/rjr-material/rtsa/afy.pdf.

Schwarzschild, M. (1948). On Noise Arising from the Solar Granulation. *The Astrophysical Journal*, 107:1–+.

Shull, J. M. and van Steenberg, M. (1982). The ionization equilibrium of astrophysically abundant elements. *The Astrophysical Journal Supplement Series*, 48:95–107.

Spitzer, L. (1962). *Physics of Fully Ionized Gases, 2nd ed.* John Wiley & Sons.

van Leer, B. (1974). Towards the ultimate conservative difference scheme, 2. monotonicity and conservation combined in a second-order scheme. *Journal of Computational Physics*, 14:361–376.

von Neumann, J. and Richtmyer, R. (1950). A method for the numerical calculation of hydrodynamic shocks. *Journal of Applied Physics*, 21:232–237.

Yokoyama, T., Akita, K., Morimoto, T., Inoue, K., and Newmark, J. (2001). Clear Evidence of Reconnection Inflow of a Solar Flare. *The Astrophysical Journal*, 546:L69–L72.